HUMAN DYNAMICS ESTIMATION DURING PHYSICAL HUMAN-ROBOT INTERACTION

Dipartimento di Elettronica, Informazione e Bioingegneria, Politecnico di Milano

Supervisor: Prof.ssa Elena De Momi
Co-Supervisor: Dott. Francesco Nori
Co-Supervisor: Dott.ssa Claudia Latella

Maria Lazzaroni, matricola 823608
Marta Lorenzini, matricola 823782

Academic Year 2015-2016

To our families

Abstract

Physical human-robot interaction has recently aroused growing interest among the scientific community: assistive technologies, collaborative industrial manipulators and rehabilitative robots are only a few examples of emerging applications. On the one hand, the researchers attempt to design the control of the robot in order to guarantee a safe interaction with the human. On the other hand, this control could be improved by adding human dynamics as a feedback to robot controllers. In this contest, estimation of human dynamic variables becomes mandatory and the importance of human sensing technologies goes without saying.

The aim of our work is to propose a computational framework for the estimation of whole-body human dynamics by means of sensors fusion. Since it is possible to replace classic boundary conditions of the Newton-Euler equations with redundant and noisy measurements coming from whole-body sensors, we compute an estimation of inverse dynamics by means of Maximum-A-Posteriori estimator, proposing a Bayesian solution of the recursive Newton-Euler algorithm. Indeed, this algorithm works in a probabilistic domain, thus it allows to assess results accuracy in terms of variance of the estimation and to associate a variance to each sensor (and to the human biomechanical model) according to their reliability, thus weighing differently that sensors role in the computation. The sensing systems included in our framework are: a full-body wearable suit provided with inertial sensors, two force plates and a robot equipped with force/torque sensors.

In order to test the proposed framework, an experimental investigation is conducted. Ten subjects are analysed, each of them performing two tasks alone and three tasks interacting with a robot. On the basis of the results, we firstly show that Maximum-A-Posteriori algorithm can deal with multiple sensors data and complex biomechanical model characterized by a high number of degrees of freedom. Once its estimation capability among different subjects is validated, we prove the robustness of Maximum-a-Posteriori algorithm with respect to modelling errors. These errors occur when an unsuitable model is employed in the computation,

therefore, by assigning an high variance (and so a low reliability) to the model itself, the algorithm is able to compensate for them. Finally, we demonstrate that, by adding progressively more sensors data to the estimation procedure, it is possible to significantly decrease variances associated to dynamic variables estimated. In order to assess the statistical significance of the results, a statistical hypothesis test is also performed.

We can state that the proposed framework allows to perform inverse dynamics in experiments analysing the physical human-robot interaction field. Its robustness with respect to modelling errors represents a unique feature in comparison with state-of-the-art methods for inverse dynamic computation discussed. We eventually demonstrate how the estimation accuracy can be improved by exploiting sensor fusion and measurements redundancy.

Sommario

L'interazione uomo-robot è un'area di ricerca multidisciplinare che sta riscuotendo un crescente interesse nella comunità scientifica. Le possibili applicazioni spaziano dalle tecnologie assistive e riabilitative ai manipolatori industriali automatizzati, giusto per citare alcuni esempi. Da una parte, l'obiettivo dei ricercatori è progettare un controllore del robot che permetta un'interazione sicura con l'uomo. Dall'altra, il controllo stesso del robot potrebbe essere migliorato fornendo come feedback al suo sistema di controllo la dinamica dell'uomo. In questo ambito, è fondamentale stimare le variabili dinamiche umane e, di conseguenza, è indiscutibile l'importanza della sensoristica applicata allo studio dell'uomo.

L'obiettivo del nostro progetto è proporre un sistema di calcolo per la stima della dinamica dell'intero corpo umano, sfruttando l'integrazione di più sensori. Dal momento che le classiche condizioni al contorno delle equazioni di Newton-Euler possono essere sostituite con le misure ridondanti e rumorose provenienti da sensori distribuiti su tutto il corpo, la dinamica inversa viene stimata tramite un algoritmo massimo a-posteriori, proponendo una soluzione Bayesiana per l'algoritmo ricorsivo di Netwon-Euler. Questo algoritmo lavora in un dominio probabilistico e quindi consente sia di valutare l'accuratezza dei risultati in termini di varianza associata alla stima, sia di attribuire ad ogni sensore (e al modello biomeccanico dell'uomo) una varianza in base alla sua affidabilità, pesando in questo modo il contributo dei diversi sensori nel calcolo. I sistemi di misura impiegati nella nostra analisi sono: una tuta indossabile dotata di sensori inerziali, due piattaforme di forza e un robot dotato di sensori di forza/coppia.

Allo scopo di analizzare il sistema proposto, abbiamo condotto un'analisi sperimentale su dieci soggetti. Ognuno di essi ha svolto due attività individualmente e tre attività interagendo con il robot. Sulle base dei risultati, abbiamo per prima cosa provato che l'algoritmo massimo a-posteriori è in grado di gestire i dati provenienti da più sensori durante esperimenti nell'ambito dell'interazione fisica uomo-robot. Una volta validata la stima tra diversi

soggetti, abbiamo dimostrato la robustezza dell'algoritmo massimo a-posteriori rispetto agli errori di modello. Tali errori si verificano in seguito all'impiego di modelli biomeccanici errati, quindi, assegnando un elevato valore di varianza (e di conseguenza una scarsa affidabilità) al modello stesso, l'algoritmo è in grado di compensarli. Infine, abbiamo provato che, aggiungendo progressivamente i dati di più sensori alla procedura di stima, è possibile ridurre in maniera significativa le varianze associate alle variabili dinamiche stimate. Al fine di provare la significatività statistica di questi risultati, è stato eseguito un test statistico di verifica di ipotesi.

Possiamo affermare che il sistema di calcolo proposto permette di calcolare la dinamica inversa in esperimenti che indagano l'interazione fisica uomo-robot. La sua robustezza rispetto agli errori di modello rappresenta una proprietà unica che non viene contemplata dai metodi classici per la dinamica inversa introdotti. Abbiamo dimostrato inoltre come sia possibile migliorare in modo significativo l'accuratezza della stima sfruttando l'integrazione di più sensori e la ridondanza delle misure.

Notation

Throughout the thesis we will adopt the following notation. Scalars are denoted with lowercase letters (e.g. m, τ), geometric vectors with bold lowercase letters (e.g. $\boldsymbol{a}$, $\boldsymbol{\omega}$), quaternions with lowercase letters (e.g. q) and matrices with bold capitals (e.g. $\boldsymbol{M}$, $\boldsymbol{R}$). Superscripts denote the frame in which a quantity is resolved (e.g. ^{G}q). Subscripts are used for annotations and indexing (e.g. F_{GRF}, $\boldsymbol{\omega}_i$).

A list of coordinate frames, of mathematical operators and of used abbreviations and acronyms can be found in the following tables.

Table 1: **COORDINATE FRAMES**

Notation	Meaning
G	Global reference frame.
i	i-th link reference frame.
j	j-th joint reference frame.
s	Sensor reference frame.

As concerns coordinate frames, we represent the $\boldsymbol{x} - \boldsymbol{y} - \boldsymbol{z}$ axes through Red, Green and Blue (RGB) convention, as can be seen in Figure 1.
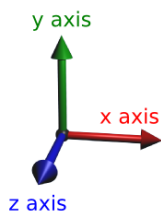
Figure 1: RGB convention for $\boldsymbol{x} - \boldsymbol{y} - \boldsymbol{z}$ axes

Table 2: **OPERATORS**

Notation	Meaning
$argmax$	Maximizing argument.
$^{-1}$	Inverse matrix.
^{T}	Transpose matrix.
$\times$	Spatial cross operator.
$\times^{*}$	Dual spatial cross operator.
$\otimes$	Quaternion multiplication.
d	Differential operator.
∂	Partial differential operator.
$diag$	Diagonal matrix.
$rank$	Rank of a matrix.
$\|\cdot\|$	Norm.
$\prod$	Multiplication.
$\sum$	Summation.
$\mathcal{N}$	Normal distribution.
$\boldsymbol{S}$	Skew-symmetric matrix.
$\lvert\cdot\rvert$	Matrix determinant

Table 3: **ABBREVIATIONS AND ACRONYMS**

Abbreviation	Meaning
w.r.t	With respect to.
2-D	Two dimensional.
3-D	Three dimensional.
CoM	Centre of mass.
DoF	Degree of freedom.
FEM	Finite element method.
F/T	Force/torque sensor.
GCS	Global coordinate system.
GRF	Ground reaction force.
GUI	Graphical user interface.
pHRI	Physical human-robot interaction.
ID	Inverse dynamics.
IK	Inverse kinematics.
IMU	Inertial measurement unit.
LCS	Local coordinate system.
MAP	Maximum-a-posteriori.
MEMS	Micro-machined electromechanical system.
RF	Reference frame.
RMSE	Root mean square error.
RNEA	Recursive Newton-Euler algorithm.
URDF	Unified robot description format.
YARP	Yet another robot platform

Contents

PART I

MOTIVATIONS AND PROBLEM STATEMENT

Chapter 1

Introduction

1. *A robot may not injure a human being or, through inaction, allow a human being to come to harm.*

2. *A robot must obey orders given it by human beings except where such orders would conflict with the First Law.*

3. *A robot must protect its own existence as long as such protection does not conflict with the First or Second Law.*

<div align="right">

Isaac Asimov

</div>

Human-robot interaction has recently aroused considerable interest among the academic community, in scientific lab environments, in technology companies and through the media. This field addresses the design, understanding, and evaluation of robotic systems, which involve humans and robots interacting through cooperation. This cooperation is one of the key technologies to broaden the application field of robots. The combination of human intelligence and robot power could be effective in several practical applications: industrial manipulators for factory automation, assistive technology and rehabilitative robots (Figure 1.1(a)) in clinical scenarios, investigation of disaster area and dangerous environments (Figure 1.1(b)), space exploration and remote and minimally-invasive surgery (Figure 1.1(c)), just to name a few examples. Researchers worldwide are analysing the various factors related to the introduction of robots in human environments and their attention is often focused on the cognitive interaction with them. There are certainly cognitive, social and ethical implications due to the human perception of the robot (and vice versa), but our discussion focuses on the distinctive aspects of physical Human-Robot Interaction (pHRI). In particular, safety and dependability are the successful evaluation criteria for mechanical design, actuation and control architectures of robots. Since it is impossible to model every action in an unstructured anthropic environment, robots should be provided with an autonomous behaviour but this can result in dangerous situations for humans
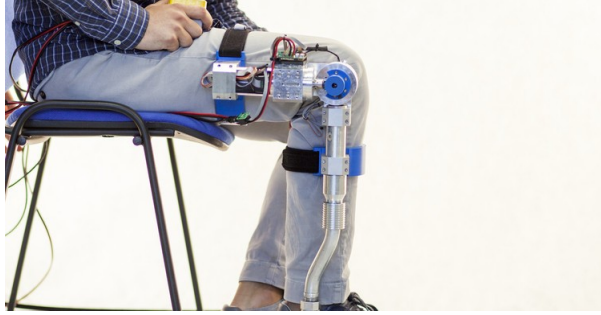
(a)
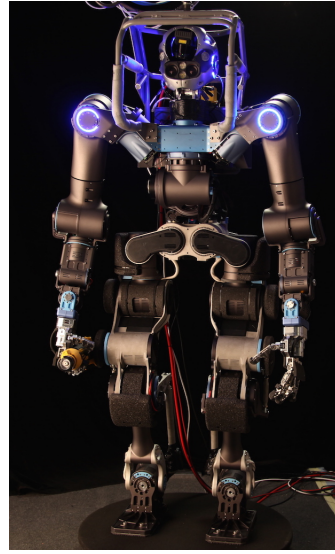
(b)
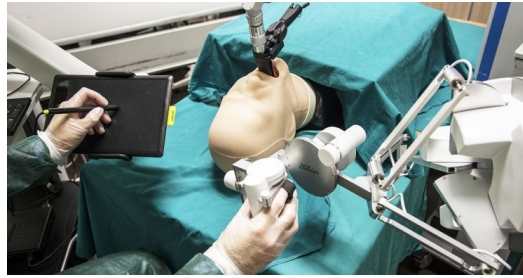
(c)

Figure 1.1: Examples of possible robot applications: (a) wearable assitive robot such as exoskeleton, (b) Walk-Man to be employed in dangerous environments and (c) robotics surgery

co-existing in the robot operational domain. By considering current robots available on the market, still not completely controllable, it is clear how natural or unexpected behaviour of people during interaction with robots can result in very severe injuries. Therefore, through a physical interaction with humans, robots could reduce fatigue and stress in assistance context, increase human capabilities in terms of force, speed and precision and improve in general the quality of life; on the other hand, the human can bring experience, global knowledge and understanding for a correct execution of tasks. By considering the huge potentiality of pHRI discussed so far, in order to spread the presence of robots in every day life, safety and dependability are the priority issues. As stated by Asimov's first law of robotics, a robot primarily may not injure a human being through its action or inaction. It is worth to notice, however, that safety standards for pHRI are still not well defined in the scientific community. Dealing with pHRI, a further step would be to replicate the physical interaction occurring during collaborative task among humans, in order to make the interaction with the robot more natural and comfortable for the human.

1.1 Motivation

In the contest of pHRI, on the one hand, the researches attempt to design the control of the robot in order to guarantee a safe interaction with the human. On the other hand, this control could be improved adding as a feedback to the robot controller dynamic variables (i.e. exchanged forces) that characterize human movements. In this way, the robot can adapt its movement to the human one, as in collaborative task between humans, where both actors adjust their strategy by observing each other actions. Thinking about a future possible scenario, we can imagine an old person with back pain that could be helped in his or her daily life by a robot that has information about his or her health condition and dynamics. To this end, estimation of human dynamic variables becomes mandatory and the importance of human sensing technologies goes without saying. Previous studies in the field of pHRI focus mainly on endowing robots with cooperation abilities that characterised the human; yet, none of them takes into account the retrieval of human motions and interaction forces. The purpose of our work is then to provide an estimation framework for computing human inverse dynamics (ID) that can be exploited in robot feedback controllers. The lack of accuracy that characterizes the traditional methods employed for ID computation, could be overcome by introducing in the analysis further information taken from additional measurement sources.

1.2 Contribution

The aim of our work is to propose an extension of a previous work [1] for the estimation of whole-body human dynamics. The introduced framework encompasses three different measurements sources. A traditional motion-capture system is replaced with a full-body wearable lycra suit equipped with three dimensions (3-D) accelerometers, gyroscopes and magnetometers, providing positions and orientations, velocities and accelerations of the human body over time. In order to retrieve external forces exchanged with the environment two force plates and a robot equipped with force/torques (F/T) sensors are exploited. It is worth to notice that the robot in this contest is not only a mere passive actor during the interaction, but it is involved as a sensor and thus as an active source of measurements. Since it is possible to replace classic boundary conditions of the Newton-Euler equations with measurements coming from sensors, we compute an estimation of ID by means of Maximum-A-Posteriori (MAP) estimator, proposing a Bayesian solution of the Recursive Newton-Euler Algorithm (RNEA) with sensors redundant measurements. This algorithm, indeed, works in a probabilistic domain, thus it allows to assess results accuracy in terms of variance of the estimation and to associate a variance to each sensor according to their reliability, weighing differently their role in the computation. Finally, a distinctive feature of MAP algorithm is the possibility of adding progressively each of sensors data to the computation and verify that sensor fusion approach allows to increase considerably results accuracy.

1.3   Thesis Outline

This thesis is structured as follows. Part I focuses on the purpose and the motivation of our work and the state of the art of the application fields. Following this introduction (Chapter 1), in Chapter 2, firstly we provide an overview on pHRI current stage and then we present ID methods and tools available in literature.

Part II addresses the issue of dynamic variables estimation for whole-body human motion. In Chapter 3 we start discussing how to solve Inverse Kinematics (IK) in order to obtain the joint angles, mandatory to perform ID computation. Then, one of the main available commercial software for ID analysis (OpenSim) is introduced. MAP algorithm is successively described in detail along with its benefits with respect to (w.r.t) the traditional methods. In addition, the sensors contemplated in our framework are depicted with all their specifications, along with the biomechanical model we provide as input for the ID analysis.

Part III presents all the elements that compose the experimental analysis. The experimental protocol, the set-up and the test conducted along with their results are discussed in Chapter 4. Finally, Chapter 5 illustrates conclusions and possible future developments of our work. Appendix A, Appendix B and Appendix C complete the thesis providing further information regarding RNEA, anthropometry and estimation worst case variance for human analysis.

Chapter 2

State of the art

Physical human-robot interaction (pHRI) is a field of growing interest among the scientific community: assistive technologies, collaborative industrial manipulators and rehabilitative robots are only a few examples of emerging applications. On the one hand, the researchers attempt to design the control of the robot in order to guarantee a safe interaction with the human. On the other hand, this control could be improved by adding as a feedback to robot controllers the dynamic variables that characterise the human. In this way, the robot could adapt its movement to the human movement as in collaborative tasks between humans, where both actors adjust their strategy by observing each other actions. In this contest, estimating human dynamic variables becomes mandatory. Our work attempts to provide a method to estimate these quantities during an interaction with a robot by exploiting measurements coming from several sources, i.e. two force plates, a full-body wearable suit provided with Inertial Measurements Units (IMUs) and the robot itself.

Among the several methods employed to compute ID we choose the RNEA which has the main advantage of being a real-time computationally efficient technique. Implementation of RNEA is presented in Appendix A.

In the following sections we present the state of the art about the two topics of interest cited above: a brief overview regarding attempts done in the direction of pHRI experiments and then a description of the ID problem and how its computation could be improved, following to a review of relevant studies found in literature. Finally, we introduce some available commercial software that can be used to perform ID analysis.

2.1 Physical Human-Robot Interaction

One of the main challenges for the robotics community dealing with pHRI is to replicate the physical interaction occurring during collaborative tasks among humans. To solve this problem, many approaches have been adopted.

A method for estimating human partner motions based on the minimum jerk model in real-time

is used in [2] in order to design a robot control. This choice is justified by the fact that humans naturally try to minimize jerk during movements. Here the attempt was that of incorporating human characteristics in the control strategy of the robot, by using the human hand estimated position to determine the position of the robot.

In [3] a preliminary investigation upon cooperative tasks with predefined trajectories is conducted: each subject performs a task in standalone mode and then in a cooperative way; obtained results reveal that the minimum jerk model fitting is not good to characterise the movement. The main limitations of this method lie in: i) the pre-determination of the task; ii) the fact that the reliability decreases considerably if the human partner decides to apply not-scheduled trajectory changes during the task or in presence of perturbations; and iii) in cooperative tasks that involve the control of an object, its final position must be known.

Several solutions have been proposed in order to overcome these limitations. In [4] to get over the traditional approach in which the planning and the guiding of the cooperative task is based entirely on the human, while the robot is a mere follower, they propose two types of controllers: a reactive controller and a proactive controller. The reactive controller dictates the follower-like behaviour of the robot by generating a reactive command based upon the current state of the environment. A proactive controller instead, dictates the leader-like behaviour thanks to the prediction of the human position in the next time step, that decides the robot proactive action. The confidence of the prediction allows to dynamically and automatically varying the behaviour of the robot during the task.

Another route for pHRI is the imitation learning approach [5]: the movement of two human actors are recorded with a motion-capture system and subsequently used to learn a compact model of the observed interaction. This model is represented with an interaction primitive (IP), a dynamical system encoding a recorded trajectory in an adaptive way. A learned IP is used by a robot to engage in a similar interaction with a human partner: human partner behaviour is predicted given a partial observed trajectory then, robot movement is guided through this estimation.

The above approaches focus mainly on endowing robots with the human cooperation ability in collaborative tasks. Yet, it would be useful to estimate human dynamics and employing human whole-body motions and interaction forces as an input for the control of the robot, in order to make the interaction more functional and improve control accuracy.

2.2 Human Inverse Dynamics estimation methods

Kinetics is the study of the forces and moments that cause motion of a body. Despite the fact that movement is characterised by smooth, regular and repeating acts, the underlying control mechanism represented by the nervous, muscular and skeletal systems is very complex. Such coordinated movements result from the activation of many muscles and it is the tension in muscles acting across joints, associated to the interaction of the body with the environment, that directly causes the kinematic pattern we observe and recognise as locomotion [6]. The study of the kinetics therefore, allows researchers

to explore basic mechanisms of human movement. There is a relevant interest in synthesising detailed description of the elements of the neuro-musculoskeletal system with measurements of movement. The aim is to develop an integrated understanding of movement of healthy subjects and to establish a scientific basis for correcting abnormal movement. A possible way to understand why and how aberrant movements occur, could be studying the cause of movement and the cause of movement may be identified with joints torques, as they are the resultant effect of the forces exerted by the muscles crossing a joint. While kinematic variables can be easily found with a good degree of accuracy, the estimation from other known variables of dynamic quantities, such as muscles and joints forces and moments that can not be readily or, indeed, ethically measured with in-vivo transducers, is a major challenge.

In biomechanics there are two main approaches to perform a dynamic analysis:

◇ **forward dynamics** is the problem of finding the joints accelerations given as input a set of initial conditions on model, state and forces;

◇ **inverse dynamics** is the problem of finding the joints torques required to produce a given acceleration taking as input a set of initial conditions on model, state and forces (e.g. using a motion-capture system and a force plate).

It is worth to remember that kinetic analysis of human movement is based on two fundamental assumptions: (1) anatomical segments are rigid bodies, (2) these rigid bodies are connected in a hierarchical chain to form a link model representation of the subject being studied. Segments should be consider as rigid bodies composed of a fixed Local Coordinate System (LCS), fixed geometric dimensions and fixed anthropometric properties: mass, location of the Centre Of Mass (CoM) and moments of inertia. To form hierarchical model of human body these segments have to be linked by joints. These joints either allow complete rotational and translational motion between them (three rotations and three translations are allowed at each joint) or specify constraints at the joints to limit one or more of the rotational or translation Degrees of Freedom (DoF) [7].

Before investigating the details of ID, we should highlight the indeterminacy of the solution to the ID problem: if we want to compute the contributions of all muscles acting on a segment, undoubtedly there are many more unknowns then independent equations and the system is said to be indeterminate. There are three main strategies that may be employed to overcome this state of indeterminacy. In the first strategy, the number of unknowns can be reduced yielding a tractable solution but this could lead to a too much approximative result. The second strategy consists in a mathematical optimisation theory [8] that treats the unknown forces as design variables. The aim is to minimize a cost function, such as a segmental energy of the joint power, subject to certain constraints, which are simply the equations of motion. The main drawback is that the cost function can not be known a-priori and there is not a procedure of validation of the resulting predictions. The last strategy consists in replacing all external forces with a single equivalent force that represents the sum of all the effective forces acting on the body and a single equivalent couple that represents the sum of all effective moments acting on

the body.

With the ID method we compute the joints reaction forces and net moments for any segments representing all bones, muscles and external forces, starting from the Newton-Euler equations of motion:

$$\sum \boldsymbol{f} = \frac{\mathrm{d}}{\mathrm{d}t}(m\boldsymbol{v}) = m\boldsymbol{a} \tag{2.1}$$

$$\sum \boldsymbol{\tau} = \frac{\mathrm{d}}{\mathrm{d}t}(\boldsymbol{I}\boldsymbol{\omega}) \tag{2.2}$$

Equation (2.1) is Newton's equation that states that the sum of all forces acting on a rigid body is equal to the rate of change of momentum of the body. Equation (2.2) is Euler's equation that states that the sum of all moments acting on a rigid body is equal to the rate of change of the angular momentum of the body.

It is possible to solve these equations for a multi-body model starting with a fixed base segment from motion-capture data, by following these steps:

1. define the segment LCS;

2. estimate the pose (position and orientation) of the model from recorded motion-capture data;

3. scale the segments anthropometry to the subject and identify the segments inertial properties;

4. compute kinematics (e.g. angular velocities and accelerations) from the pose estimated;

5. record and represent external forces acting on the body;

6. compute the joints reaction forces, net joints moments and joints powers.

Below, a brief description of the *steps 1-5* is presented. Then, we will focus in a more detailed way on the *step 6*.

A mathematically convenient consequence of the assumption of rigidity is that, in the context of kinematics, each segment is defined completely by an LCS fixed in that segment (*step 1*); as the segment moves, the LCS moves correspondingly. The LCS is right-handed and orthogonal; its position and orientation w.r.t. the global coordinate system (GCS) defines the position and orientation of the body or segment in the GCS (e.g. the capture volume in which we represent the 3-D space of the motion-capture system).

The pose of an unconstrained rigid segment (*step 2*) requires six independent variables (commonly referred to as DoFs): three to specify the location of the origin and three to specify the orientation. There is a relationship between the number of markers and the number of DoFs: one marker attached to a segment is sufficient to define 3 DoFs, by adding another marker the DoFs became five and a third marker adds the last DoF. Thus, in order to fully describe the pose of the segment (6 DoFs), we have to locate at least three non-collinear markers on the segment. Tracking of a segment refers to the process of estimating the pose of the segment from motion data. There are several algorithms for estimating the pose of rigid bodies and they all undergo the assumption that the markers move

rigidly with the body segments which they are attached to; this means that markers coordinates in a segment LCS do not change during movement. Markers noise and especially soft tissue artefacts could result in poor estimation of the pose but judicious markers placement or the choice of an appropriate estimation algorithm partially solve the problem.

In order to perform ID, inertial properties of the recruited subjects along with segments dimensions are required (*step 3*). In particular, the segment inertial properties that have to be identified are: segment mass, segment CoM and segment momentum of inertia. To provide all of them, different approaches have been proposed in literature: direct measurements ([9], [10]), regression equations derived from cadaver dissections ([11], [12], [13]), regression equations derived from skeletons ([14]) and geometrical representations of the segments ([15], [16], [17]). All of these approaches are estimates, thus the choice should be based on the population being studied and on the level of accuracy that the researchers require for a given experimental hypothesis. In the event of multiple subject being investigated, the manual measuring of the parameters of interest on each subject is not feasible. Thanks to anthropometric data found in literature, the estimation of these inertial and geometric parameters specific for each subject could be implemented in an automatic way, starting from his mass and his height. Information about anthropometric data can be found in Appendix B.

Then, we have to compute kinematics (*step 4*) because the solution for ID requires as inputs the position of the centre of gravity, linear velocity, linear acceleration, angular velocity and angular acceleration of each segment. To this end, linear kinematics defined in the GCS for the position, velocity and acceleration of the CoM of the segment is sufficient.

At this point, the biomechanical model is composed of segments defined by an LCS, provided with inertial proprieties and the kinematics which has been computed from the pose of segments as estimated from the 3-D motion-capture data. Since subject movement goes along with interaction of the body with the environment, it is necessary to measure or model all external forces acting on the analysed subject (*step 5)* to calculate accurate joints torques and forces. The most significant and often the only one available is the ground reaction force (GRF), that has to be defined in the GCS. Once we have calculated segment inertial properties, kinematics and external forces, we have all the inputs required to determine the joints reaction forces and the joints net moments (*step 6*). For segment s we can express (2.1) as the sum of all forces $\boldsymbol{f}_s$, acting on segment s:

$$\sum \boldsymbol{f}_s = m_s \boldsymbol{a}_s \qquad (2.3)$$

If there is more than one unknown force, it is not possible to compute the individual force without additional information and for this reason we have to set up equations with only one unknown. A general expression of the reaction at the $j - th$ joint for any linkage of m segments distal to the joint can be expressed as:

$$\boldsymbol{f}_j = \left(\sum_{s=1}^{m} m_s(\boldsymbol{a}_s - \boldsymbol{g}) \right) - \boldsymbol{f}_{grf} \qquad (2.4)$$

where we sum over all (m) segments distal to the proximal joint including the segment for which the

joint is associated. Reminding that the momentum of force $\boldsymbol{\tau}$ produced by a single force $\boldsymbol{f}$ acting on a segment can be computed as:

$$\boldsymbol{\tau} = \boldsymbol{r} \times \boldsymbol{f} \tag{2.5}$$

where $\boldsymbol{r}$ is the vector from the point at which the momentum is computed (typically the origin of the segment or the CoM of the segment) and one point along the force vector $\boldsymbol{f}$, we can now compute the net joint momentum acting on a segment. In order to simplify the computation, considering that the momentum of inertia $\boldsymbol{I}$ is constant in the segment LCS and not in the GCS during movement, we express the inertial contribution to the net momentum ($^{\text{LCS}}\boldsymbol{\tau}_s^I$) in the segment LCS:

$$^{\text{LCS}}\boldsymbol{\tau}_s^I = \frac{\mathrm{d}}{\mathrm{d}t}(\ ^{\text{LCS}}I_s\ ^{\text{LCS}}\boldsymbol{\omega}_s) = \ ^{\text{LCS}}I_s\ ^{\text{LCS}}\boldsymbol{\alpha}_s + \ ^{\text{LCS}}\boldsymbol{\omega}_s \times (\ ^{\text{LCS}}I_s\ ^{\text{LCS}}\boldsymbol{\omega}_s) \tag{2.6}$$

and then we transform it back to the GCS ($\boldsymbol{\tau}_s^I$):

$$\boldsymbol{\tau}_s^I = \ ^{\text{LCS}}\boldsymbol{R}_s\ ^{\text{LCS}}\boldsymbol{\tau}_s^I \tag{2.7}$$

We can express the sum of the moments acting about the CoM of the segment s as equal to the inertial momentum in the GCS:

$$\sum \boldsymbol{\tau_s} = \boldsymbol{\tau_s^I} \tag{2.8}$$

Then, the general equation to compute the net joint moments by summing the expression over all (m) segments distal to the joint can be written as:

$$\boldsymbol{\tau}_j = \left[\sum_{s=1}^{m} \boldsymbol{\tau}_s^I + \boldsymbol{r}_{j,s} \times m_s\ (\ ^{\text{LCS}}\boldsymbol{\alpha}_s - \boldsymbol{g}) \right] - \boldsymbol{\tau}_{grf} - \left[\boldsymbol{r}_{j.grf} \times \boldsymbol{f}_{grf} \right] \tag{2.9}$$

where $\boldsymbol{r}_{j.grf}$ is the vector from the joint to the GRF and $\boldsymbol{r}_{j,s}$ is the vector from the joint to the CoM of segment s.

2.2.1 Inverse dynamics optimization strategy

In order to improve ID computations several solutions have been proposed in literature; some of the methods implemented are presented below.

In ID computation, the accuracy of the solution strongly depends on the accuracy of the input data. In particular, estimated joints moments are highly sensitive to uncertainties in acceleration data. In order to overcome this limitation, measuring of external forces and moments (ground reaction component recordings, i.e, with force plates) reduces the influence of the acceleration estimates and joints moments estimations tend to be more accurate. Alternatively, classic mechanical computation can be improved with an optimization approach to provide optimal acceleration distributions. Accelerations are usually calculated from noise-polluted position data by using numerical double differentiation, which amplifies measurements noise. Low-pass filtering of raw position data improves the accuracy of the double differentiation calculations by reducing high frequency random measurements noise.

Nevertheless, data smoothing can not eliminate systematic errors, as the inaccurate positions of body markers.

In [18] the aim is to exploit the knowledge of all available imperfect position and force measurements to extract optimum acceleration estimations. A least-squares optimization approach, that exploits the over-determinacy arising from the introduction of the force plate, is employed in order to provide optimal acceleration values most consistent with dynamic and kinematic measurements. Joints moments can then be calculated from these optimal kinematic values via ID. Thanks to this method, it is possible to accurately predict ground reactions and provide optimal joint moments estimations that largely differ from classic calculations. Furthermore, the formulation is based on the over-determinacy of the system, thus the estimation can be performed even if some of the force measurements are missing.

The main limitations associated with measuring kinematics with video system and GRFs with a force plate, deal with: the accuracy of the acquisition systems, the dimension of the field of view and the double differentiation of kinematic data (which requires severe low pass filtering). In order to overcome these drawbacks a new method for ID analysis, based on 3-D accelerometers, is developed in [19]. The procedure, based on the assumption that the body segments are rigid, consists in computing resultant loads of segment from loads acting on a number of test masses inside the accelerometers. The use of four tri-axial accelerometers allows to compute kinematic variables (linear acceleration and gravity, angular velocity and angular acceleration) without performing integration or differentiation. The method can only be applied during the single support phase of gait or other movements while for walking and running it systematically underestimates the forces and the moments by about 20%, but it has been demonstrated that its results are similar to the loading patterns obtained with a conventional analysis [19]. The accelerometers method has the advantages of not requiring a gait laboratory environment and it can be used for studies with a completely body-mounted recording system. Moreover, since integration or differentiation are not required, the method provides the possibility of real-time analysis. Concerning the implementation of the analysis, in order to estimate the kinematic variables, we use the signal produced by the uniaxial accelerometer attached to a rigid body segment at a known position r and with orientation u, written as:

$$s = u \left(R^{-1}(a - g) + \dot{\omega} \times r + \omega \times (\omega \times r) \right) \tag{2.10}$$

where R is the rotation matrix of the body segment w.r.t. the ground, a is the acceleration of the origin of the segment coordinate system (chosen as the CoM of the body w.r.t. the ground), g is the gravitational field and ω is the angular velocity of the body, expressed in the body-fixed coordinate system. The Equation (2.10) can be rewritten as:

$$s = u \left(s_0 + \dot{\omega} \times r + \omega \times (\omega \times r) \right) \tag{2.11}$$

since gravitational force and inertial forces due to linear acceleration can not be separated. Signals from four tri-axial accelerometers attached to the same rigid body are recorded and so we obtain twelve

of these algebraic equations in the nine unknown kinematic variables (s_0, ω, $\dot{\omega}$). The Levenberg-Marquardt method for non-linear least-square problems is used to solve the kinematics and this configuration provides sufficient redundancy to eliminate singularities in the system of the equation. Then f and M have to be computed, by using the equations of motion of rigid body in three dimensions that, for translation and rotation respectively, are:

$$f + mg = ma \tag{2.12}$$

$$M' = I\dot{\omega} + \omega \times (I\omega) \tag{2.13}$$

where f is the sum of all forces acting on the segment, except for gravity, expressed in the ground-based coordinate system; M' is the sum of all moments on the segment, expressed in the body-fixed coordinate system, m is the segment mass and I is the inertia matrix. Transforming the Equation (2.12) into the segment coordinate system:

$$f' = R^{-1}f = mR^{-1}(a - g) = ms_0 \tag{2.14}$$

the Equations (2.14) and (2.13) produce the six load components f', M' acting at the CoM of the rigid body.

Classic estimation of joints torques in biomechanics consists in the bottom-up ID method, where motion-capture and GRFs measurements are used to solve Newton-Euler equations from the ground to the top, one after another. The major drawback of this technique is that measurement errors are propagated progressively during the process, leading to uncertainties on the estimation of joints torques. The joint torque estimation is made highly noise-sensitive by the need of computing velocity from the segment position and thus real-time estimations are difficult to implement. [20] attempts to overcome these lacks by means of a nonlinear unknown-input observer that allows the real-time estimation of both the joints torques and the angular velocities from angular position measurements with good accuracy. The form of a Takagi-Sugeno (T-S) model is used to design the nonlinear state space dynamical descriptor and the convergence of the estimation errors (in positions, velocities and torques) is established using a quadratic Lyapunov function through Linear Matrix Inequality (LMI) conditions. The results of this approach are successfully compared with the classic ID method.

It is important to remind that in ID computation the main sources of error are:

⋄ inaccuracy in momentum coordinate data,

⋄ estimation of body segment parameters,

⋄ errors related to force plate measurements,

⋄ identification of joint centre [21], [22], [23], [24].

Inaccuracy in momentum coordinate data affects the calculation of the motion of body segments in the form of i) error in markers location due to inherent motion-capture system noise, and ii)relative motion between skin-mounted markers and the underlying bones [25], [26], [27].

ID computation uses traditionally two approaches. The first has as input only kinematic and anthropometric data to calculate joints torques: this is the top-down approach that starts at the distal segment and proceeds downward such that dynamic equilibrium conditions are satisfied for each successive segment. However, it is quite sensitive to the propagation of inaccuracies, including those affecting acceleration data. The second method improves torque estimation for the lower extremity and reduces acceleration effects by adding kinetic data, typically GRFs. This bottom-up approach starts at the distal segment of one or both lower extremities and proceeds upward; by incorporating GRFs measurements, boundary conditions are defined; these conditions result in an over-determined system, since there are more equilibrium equations than system unknowns. This redundancy has been used to reduce error effects through optimization methods, adjusting specific input parameters in the top-down calculations until optimal values, in order to minimize the differences between the known ground reaction measurements and those predicted through the top-down calculations, are found. These optimization methods have been used to:

⋄ determine an optimal set of body segment parameters,

⋄ reduce the effect of noise in measured data,

⋄ calculate optimal segment accelerations in order to improve joint torque calculation.

However, their cost functions do not contain information on the joints torques and therefore it is possible to minimize them but also to increase error in the joints torques. To improve this optimization in [28] a constrained nonlinear optimization problem is formulated with a cost function that minimizes the difference between the measured GRFs and the GRFs calculated via a top-down ID approach. The objective function is the least-square of the difference between these two quantities:

$$z = \sum_{i=1}^{n} \left[\ (f_i^x(v) - \bar{f}_i^x)^2 + (f_i^z(v) - \bar{f}_i^z)^2 + (\tau_i^y(v) - \bar{\tau}_i^y)^2 \ \right] \qquad (2.15)$$

where z is the objective function, v is a vector of optimization variables (i.e. segment angles), i is the time index, n is the total number of time intervals, f^x, f^z, τ^y are the GRFs and torque calculated using a top-down approach as a function of the optimization variables v and $\bar{f}^x$, $\bar{f}^z$, $\bar{\tau}^y$ are the known ground reactions.

The equations of motion used to calculate the joints torques, GRFs and moments are subjected to kinematic constraints that relate the segment angles to the position of each segment CoM. The minimization is made under the equality and inequality constraints on the motion parameters: the equality ones are used to calculate angular velocity and acceleration for each segment, the inequality ones are based on the literature and previous knowledge of the system to give a range in which the solution could be found; angular position are limited to upper and lower bounds. Another inequality constraint is based on the kinematic configuration stating that error in the location of each joint centre has to fall within a specified range.

The final outputs of the minimization are the optimized angular profiles and optimization-based joints torques; these results tend to have larger errors at the beginning and at the end of the motion, since no boundary condition constraints are specified. The optimization approach outperforms traditional ID approaches by estimating more accurate torques.

2.2.2 Inverse dynamics tools

Since there is a growing need for software tools that can accurately simulate the complex dynamics of modern robots, several softwares have been developed. We provide below an introduction of two examples of available commercial software (i.e. AnyBody and MuJoCo). Since OpenSim ID tool is employed in our analysis, it will be presented in detail in the next chapter.

In [29] AnyBody Modeling System, a software capable of analyzing the musculoskeletal system of humans as rigid body systems, is reviewed. Among the main features of the system the ID analysis computes the muscles activation patterns, based on a specified task and the forces and moments to perform it. ID puts many restrictions on the model but it is computationally more efficient than forward dynamic and thus can be used with more complex models comprising more muscles, i.e. a finer level of details of the mechanical model of the body.

An important issue with simulation software lies in the contact dynamics. Engines such as SD/FAST [30] and OpenSim either ignore contacts, or use spring-dampers, resulting in too huge approximations or in stiff dynamics. This limits their applications to robotics where contact dynamics are key. For this reason, a new wave of simulators which combine efficient recursive algorithm in joint space and modern velocity-stepping methods for contact dynamics has been developed. One of them is MuJoCo, presented in [31], whose acronym stands for MUlti-JOint dynamics with COntact. It is worth nothing that ID with MuJoCo can always be computed, even in the presence of contacts and equality constraints.

In summary, in the field of dynamic simulation it is difficult to select the best tool for a given project or to predict how much effort will be needed and what the ultimate performance will be. In [32] a comparison of several different simulation software has been presented and it has been found that each engine performs best on the type of system it is designed and optimised for.

PART II

HUMAN INVERSE DYNAMICS ESTIMATION

Chapter 3

Inverse dynamics estimation by exploiting sensors fusion

The importance of knowing dynamic information in human motion, such as forces and torques, is a crucial point in several research areas as ergonomics for industrial scenarios, rehabilitation monitoring or for developing prosthetic devices and exoskeleton systems. Although motion-capture is a powerful tool used in a large range of applications towards human movement analysis, its main limitation is the lack of dynamic information as it typically employs only kinematic estimates. For these reasons, human force capture estimation is not a new challenge for the scientific community but the topic has been seldom explored in-situ due to the computational difficulties of the analysis. In order to compensate for these computational deadlocks, it is here proposed a probabilistic algorithm to estimate dynamic quantities by harnessing redundant measurements information coming from different sensors.

In the next sections we firstly discuss how to solve inverse kinematics (IK) in order to obtain the joints angles, mandatory to perform ID computation. Then, our solution for the estimation problem is presented and the description of all the sensors employed for the sensor fusion is provided. Along with these sensors data, a fundamental input for the ID computation is the biomechanical model of the subject performing the experimental analysis. An overview of the available methods for human modelling and a full description of our model is presented.

3.1 Inverse Kinematics

In [1] the IK problem has been solved with a geometric approach: starting from the marker coordinate data the links have been reconstructed and the angles between them have been estimated. In order to achieve better results in term of accuracy, we decided to employ OpenSim, a commercial and robust software that automatically computes kinematic variables in term of joint angles with the relative tool.

OpenSim is an open source software for modelling humans, robots and the environment in 3-D, and simulating their interaction and movement. It allows to build models of a broad range of musculoskeletal structures and many other mechanisms. Models can include any combination of rigid bodies, simple and complex joints, constraints, springs, dampers, contacts, controllers, muscles, and other actuators. The graphical user interface (GUI) allows to load and visualize models, simulate their movements and edit any of their properties [33]. OpenSim has fast and robust tools for performing IK, ID and generating forward simulations of movement, once marker data, joint kinematics, and external forces have been imported [34].

3.1.1 OpenSim Inverse Kinematics tool

The IK tool steps through each time frame of experimental data and reconstructs the model movement that 'best matches' experimental markers and coordinate data, in order to compute the joint angles and/or translations. This 'best matching' is the pose that minimizes a sum of weighed squared errors of markers and/or coordinates. Obtaining accurate results from the IK tool is essential for using later the ID tool [33].

The primary inputs to IK are the following files:

⋄ a subject-specific OpenSim model (`.osim`) that must include inertial parameters, information about how links and joints are connected and their Reference Frames (RFs), along with an associated marker set containing adjusted virtual markers (the model and the relative marker set are showed in Figure 3.14). It is a text file in which the units of measurement are specified and includes the `<BodySet>` whose objects are the bodies and the joints that compose the model, the `<ConstraintSet>`, the `<ForceSet>` and the `<MarkerSet>` subsection;

⋄ experimental marker trajectories (`.trc`) of a trial obtained from a motion-capture system, along with the time range of interest. It is a text file composed by a header containing information about the temporal settings and the units of measurement of the raw data and by a body containing the marker coordinates for each time frame;

⋄ an optional file (`.mot`) that includes experimental generalised coordinate values (joint angles) of a trial obtained from alternative motion-capture devices or other specialised algorithms. The end-user can optionally specify relative coordinate weighs in the `Tasks` file, if joint angles are known a-priori.

It is also possible to create and load a setup file (`.xml`) containing all the settings information for the IK tool: the marker trajectories, the time range for the analysis, the output file where the results are stored and marker weighs. Marker weighs determine how 'well' the virtual markers track experimental markers (a larger weigh for a given marker will mean less error; the error is the distance between the virtual and experimental representations of a marker, for that marker). The other possibility is to set the session settings manually.
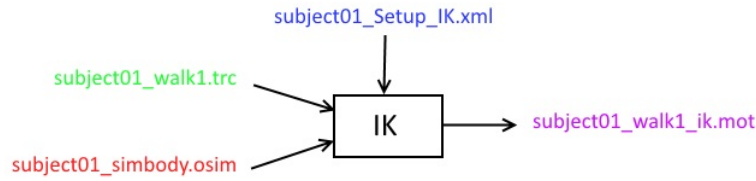
Figure 3.1: Input and output of the IK tool. Experimental data are shown in green, OpenSim files (`.osim`) in red, settings files in blue and the files generated by the workflow are shown in purple.

The IK tool then generates a motion file (`.mot`) containing the generalised coordinate trajectories (joint angles and/or translations). It is worth noting that, when collecting experimental data to analyse motion and perform IK, the development and documentation of procedure protocols and standards (for marker sets, camera locations, and force plate coordinate frames) allow the user to obtain accurate and reliable results and repeatable data. To make the pre-processing and the importing of data into OpenSim is good practise to employ them. Total Root Mean Square Error (RMSE) and maximum marker errors are displayed in the 'Messages' window. It is possible to use these values to guide changes in weighs or, if necessary, to redo marker placement. Maximum marker error should be generally less than 2-4 cm, and RMSE under 2 cm is achievable. These guidelines will vary depending on the nature of the model and the motion being examined.

The input and the output for the IK tool are shown in Figure 3.1.

Mathematically, IK computation is expressed as a weighed least-squares problem, whose solution aims to minimize both marker and coordinate errors. The marker error is the distance between an experimental marker and the corresponding marker on the model when it is positioned using the generalized coordinates computed by the IK solver. Each marker has a weigh associated with it, specifying how strongly that marker error term should be minimized. A coordinate error is the difference between an experimental coordinate value and the coordinate value computed by IK.
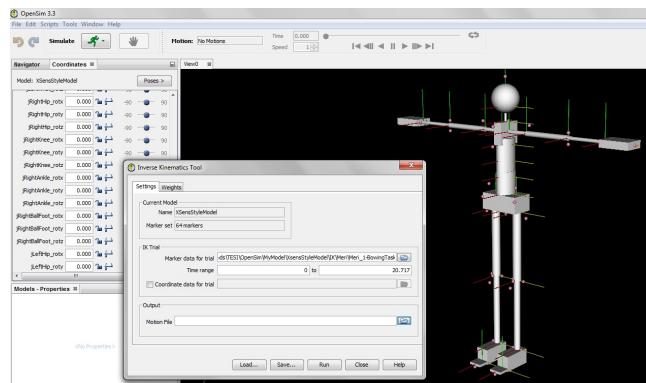

Figure 3.2: OpenSim model with the relative marker set whose trajectories are employed in IK analysis.

Experimental coordinate values can be joint angles themselves obtained directly from a motion-

capture system, or may be computed from experimental data by various specialized algorithms or by other measurement techniques that involve other measurement devices. A fixed desired value for a coordinate can be also specified. Overall, the inclusion of experimental coordinate values is optional since the IK tool can solve for the motion trajectories using marker matching alone. A distinction should be made between prescribed and unprescribed coordinates. A prescribed coordinate (also referred to as a locked coordinate) is a generalized coordinate whose trajectory is known and which will not be computed using IK, therefore their known values will be used. This can be useful when some generalized coordinate value is evaluated as reliable and therefore it is preferable the IK solver does not change it. An unprescribed coordinate is a coordinate which is not prescribed, and whose value is computed from IK. By using these definitions, only unprescribed coordinates can vary and thus only these will appear in the least-squares equation solved by IK. Each unprescribed coordinate being compared to an experimental coordinate must have a weigh associated with it, specifying how strongly that coordinate error should be minimized.

The weighed least-squares equation solved by IK is:

$$\min_{\boldsymbol{q}} \left[\sum_{i \ \epsilon \ markers} w_i \ \|\hat{\boldsymbol{x}}_i - \boldsymbol{x}_i(\boldsymbol{q})\|^2 + \sum_{j \ \epsilon \ uc} \omega_j (\hat{\boldsymbol{q}}_j - \boldsymbol{q}_j)^2 \right] \tag{3.1}$$

$$\boldsymbol{q}_j = \hat{\boldsymbol{q}}_j \quad \text{for all pc j} \tag{3.2}$$

where $\boldsymbol{q}$ is the vector of generalized coordinates being solved for, $\hat{\boldsymbol{x}}_i$ is the experimental position of marker i, $\boldsymbol{x}_i(\boldsymbol{q})$ is the position of the corresponding marker on the model (which depends on the coordinate values), $\hat{\boldsymbol{q}}_j$ is the experimental value for coordinate j; uc indicates unprescribed coordinates while pc indicates prescribed coordinates. Prescribed coordinates are set to their experimental values. The marker weighs w_i and coordinate weighs ω_j are specified in the `<IKMarkerTask>` and `<IKCoordinateTask>` tags in the setup file, respectively. This least-squares problem is solved by means of a general quadratic programming solver, with a convergence criterion of 0.0001 and a limit of 1000 iterations. The least-squares solution is affected by the choice of length and angle units. The units used by IK are the model units, which are meter $[m]$ for lengths and radians $[rad]$ for angles.

3.2 Classic Inverse Dynamics

The field of motion analysis is driven by observation and experiments, but there are two fundamental drawbacks in using them alone for movement dynamics understanding. Firstly, important variables generated by muscles are not directly measurable in experiments. Secondly, in complex dynamic systems cause-effect relationships are difficult to determine from experimental data. Considering that the knowledge of internal forces in multi-articulated human movements is of considerable importance in many biomechanical and neuro-physiological investigations, kinematic variables have to be integrated

with the information coming from ID analysis. The results of this computation can be obtained performing dynamic simulations of movement that integrate biomechanical models describing the anatomy and the physiology of the neuro-musculoskeletal system and the mechanics of multi-joints movement. To this end, several software has been developed. We will focus in detail on OpenSim and successively we will briefly present other alternative software.

3.2.1 OpenSim Inverse Dynamics tool

A classic ID tool determines the generalized forces (e.g. net forces and torques) at each joint responsible for a given movement. Given the kinematics (e.g. the state) describing the motion of a model and perhaps a portion of the kinetics (e.g. external loads) applied to the model, the ID tool uses these data to perform an ID analysis. Classic mechanics mathematically expresses the mass-dependent relationship between force and acceleration, $\mathbf{f} = m\mathbf{a}$, with equations of motion. The ID tool solves these equations, in the ID sense, to yield the net forces and torques at each joint which produce the movement [33]. In order to compute the ID three inputs are required :

⬦ a subject-specific OpenSim model (`.osim`) that must include inertial parameters, information about how links and joints are connected and their RFs. It is a text file in which the units of measurement are specified and includes the <`BodySet`> whose objects are the bodies and the joints that constitute the model, the <`ConstrainSet`>, the <`ForceSet`> and the <`MarkerSet`> subsection;

⬦ a motion file (`.mot`) containing the time histories of generalized coordinates that describe the movement of the model. It is a text file constituted by a header containing information about the dimensions and the units of measurement of the raw data and by a body containing the joint angles for each time frame;

⬦ external load data (`.xml`), (i.e. GRFs, moments, and center of pressure location). It is a text file including the <`ExternalLoads`> subsection whose objects are the information about the external force data and information about the low pass filtering performed on them. It is worth to notice that it is necessary to measure and apply or model all external forces acting on a subject during the motion to calculate accurate joints torques and forces.

It is possible to create and load also a setup file (`.xml`) in order to specify parameters relating to the input kinematics of the current model, the time range for the analysis and the folder where the results are stored. The other possibility is to set them manually. A filtering of the coordinate data can be introduced by setting the cut frequency, since noise is amplified by differentiation; without filtering, the calculated forces and torques will be very noisy.

The ID tool then generates a single output file (`.sto`) in a folder specified in the setup file. This storage file contains the time histories of the net joints torques and forces acting along the coordinate axis that produce the accelerations estimated (via double differentiation) from the measured
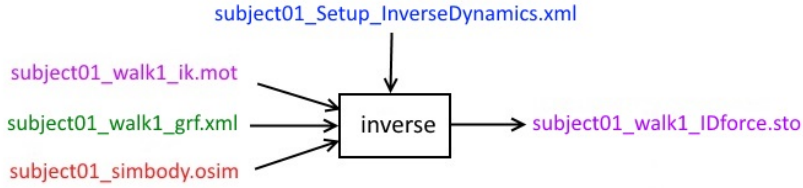
Figure 3.3: Input and output of the Inverse Dynamics tool. Experimental data are shown in green; OpenSim files (`.osim`) are shown in red; settings files are shown in blue; files generated by the workflow are shown in purple.

experimental motion and the external forces applied; it is a text file constituted by a header containing information about the dimensions and the units of measurement of the raw data and by a body containing the data. The input and the output for the ID tool are shown in Figure 3.3.

It is useful to remind in this context how ID works; the classic equations of motion may be written in the following form considering Lagrange formulation [33]:

$$H(q)\ddot{q} + C(q,\dot{q}) + G(q) = \tau \tag{3.3}$$

- $\diamond$ $q, \dot{q}, \ddot{q} \in \mathbb{R}^N$ are the vectors of generalized joints positions, velocities, and accelerations, respectively;

- $\diamond$ $H(q) \in \mathbb{R}^{N \times N}$ is the system generalised inertial matrix;

- $\diamond$ $C(q,\dot{q}) \in \mathbb{R}^N$ are the vectors of Coriolis and centrifugal forces;

- $\diamond$ $G(q) \in \mathbb{R}^N$ is the vector of gravitational forces;

- $\diamond$ $\tau \in \mathbb{R}^N$ is the vector of generalized forces.

where N is the number of DoFs. The motion of the model is completely defined by the generalized positions, velocities and accelerations. Consequently, all of the terms on the left-hand side of the equations of motion are known. The remaining term on the right-hand side of the equations of motion is unknown. The ID tool uses the known motion of the model to solve the equations of motion for the unknown generalized forces. Overall, all the tools which implement ID analysis require a forward step of IK. In this step, the markers trajectories, acquired thanks to a motion-capture system, are used to build the joint positions related to the biomechanical model of the subject that has to be implemented previously. Then, during the ID step, the joints torques associated to the studied motion are obtained from the joint positions. There is another possible further step consisting in an estimation of the muscles forces based on an optimization algorithm, starting from joints torques.

Some examples of OpenSim possible applications can be found in literature. In [34] is introduced SimTrack, an accurate tool capable of generating muscle-actuated simulation of subject-specific motion quickly, that creates a dynamic simulation through four steps, taking as input i) a dynamic model of the musculoskeletal system, ii) an experimentally-measured kinematics, iii) reaction forces and iv)

moments. In step 1, a dynamic musculoskeletal model is scaled in order to match the anthropometric measurements of an individual subject, obtained as the distance between pairs of markers acquired by a motion-capture system. The masses, instead, are scaled proportionally to the total measured mass. Step 2 consists in a least-squares problem that minimizes the differences between the measured and the model virtual markers locations in order to solve IK and determine joint angles and relative translations. For each frame in the experimental kinematics, the weighed square error that has to be minimized is:

$$\varepsilon = \sum_{i=1}^{M} w_i (\boldsymbol{x}_i^{subject} - \boldsymbol{x}_i^{model})^2 + \sum_{j=1}^{N} \omega_j (\boldsymbol{\theta}_j^{subject} - \boldsymbol{\theta}_j^{model})^2 \tag{3.4}$$

where M is the number of markers, N is the number of joints, $\boldsymbol{x}_i^{subject}$ and $\boldsymbol{x}_i^{model}$ are the 3-D positions of the i-th marker or joint centre for the subject and the model, $\boldsymbol{\theta}_j^{subject}$ and $\boldsymbol{\theta}_j^{model}$ are the values of the j-th joint angles for the subject and the model and w_i and ω_j are factors that allow markers and joint angles to be weighed differently. Step 3 allows to make the model generalized coordinates more dynamically consistent with the measured GRFs and moments thanks to a Residual Reduction Algorithm [35]. Then, in step 4, Computed Muscle Control, a method which employs static optimization criterion to distribute forces across synergistic muscles and proportional-derivative control to generate a forward dynamic simulation that tracks the kinematics, produces a set of muscles excitations in order to create a coordinate muscle-driven simulation of the subject movement.

In [36] the authors demonstrate how torque computation with ID tool can be useful in order to validate the meaning of the muscle momentum arm, a quantity of interest to biomechanical researchers and clinicians since it represents a measure of the effectiveness of a muscle and it contributes to a particular motion over a range of configurations. This relation between torques and muscle momentum arm is fundamental in mapping between biomechanical systems and multi-body models. Given the requirement that a momentum arm depends only on the joint-associated kinematic variable $\boldsymbol{\theta}$, the muscle momentum arm quantity is defined as:

$$r_\theta \triangleq \frac{\tau_\theta}{s} \tag{3.5}$$

where τ_θ is a scalar representing the 'effective torque' acting about θ, due to the scalar tension force $s > 0$ generated by muscles activation. Starting with this definition, there are several methods differing in precision, implementation and conceptual difficulties in order to compute muscle momentum arm:

⋄ perturbation method,

⋄ path velocity method,

⋄ partial velocity method,

⋄ generalized force method.

Once momentum arm has been computed, in order to show that the result is consistent with the definition and thus it provides a biologically-relevant quantity, τ_θ is calculated and compared with $r_\theta s$.

3.3 Maximum-A-Posteriori algorithm for dynamics estimation

The estimation procedure we use for computing human dynamic variables is originally proposed in the domain of humanoid robot control. Starting from the Newton-Euler algorithm, the classic boundary condition in the recursive algorithm (i.e. linear-angular velocities and acceleration at the base link and forces-torques at the end-effector) are replaced with redundant (and noisy) measurements coming from whole-body distributed sensors that, in this way, play an active role in the computation. The proposed algorithm computes an estimation of the dynamic variables, assumed as stochastic variables with Gaussian distributions, providing as a Maximum-A-Posteriori (MAP) their mean and covariance conditioned on all the available measurements. The estimation of the dynamic variables is performed within a Bayesian Framework, in which it is possible to weigh differently the constraints according to the available sensors accuracy. The framework encompasses different data sources: *i*) a full-body wearable sensor suit provided with 17 inertial measurements units; *ii*) two force platforms; and *iii*) a full-body humanoid robot. Since the real forces, torques, velocities and accelerations acting on the system are not noise-free measurements, by exploiting sensor fusion and redundancy it is possible to significantly improve the estimation accuracy.
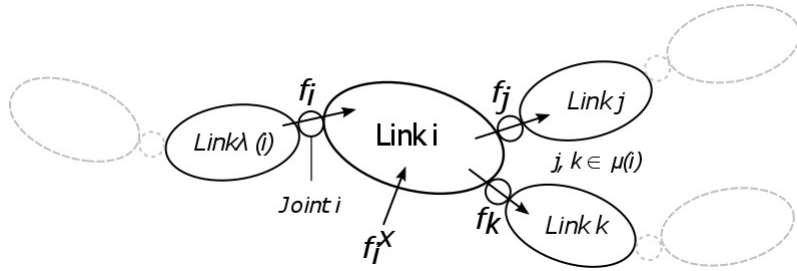
Figure 3.4: Articulated multi-body as an oriented kinematic tree.

3.3.1 Background

The notation adopted follows the one used in [37]: all variables are spatial vectors (six dimensional vectors including angular quantities in the first three components and the rest as linear quantities). Within this notation, an articulated rigid body is a system modeled as an oriented kinematic tree (Figure 3.4) with N_B moving links numbering from 1 to N_B (0 is the fixed base). Each link in the model is associated with a unique node in the tree. Node numbers can always be selected in a topological order so that each node i has a higher number than its unique parent $\lambda(i)$ and a smaller number than all the nodes in the set of its children $\mu(i)$. Links i and its parent $\lambda(i)$ are coupled with joint i according to Denavit-Hartenberg convention for joint numbering [38]. Joint i motion constraints are modelled with $\boldsymbol{S}_i \in \mathbb{R}^{6 \times n_i}$, being n_i the number of DoFs of the joint i and $n = n_1 + ... + n_{N_B}$ the total number of DoFs of the system excluding the fixed base. For each rigid link i, the system is modeled also by supplying the spatial inertia tensor $\boldsymbol{I}_i$:

$$\boldsymbol{I}_i = \begin{bmatrix} \boldsymbol{I}_{C,i} + m_i \boldsymbol{c}_i \times \boldsymbol{c}_i^T & m_i \boldsymbol{c}_i \times \\ m_i \boldsymbol{c}_i \times^T & m_i \boldsymbol{I}_{3\times3} \end{bmatrix} \tag{3.6}$$

where $\boldsymbol{I}_{C,i}$ is the spatial inertia tensor w.r.t. the body CoM, m_i is the total mass, $\boldsymbol{c}_i$ is the relative displacement between the CoM and the origin of the link RF. The motion-vector transform from the RF of the rigid link i to the RF of the rigid link j $^j\boldsymbol{X}_i$ and its analogous transformation for a force vector $^j\boldsymbol{X}_i^*$:

$$^j\boldsymbol{X}_i = \begin{bmatrix} ^j\boldsymbol{R}_i & \boldsymbol{0}_{3\times3} \\ -\,^j\boldsymbol{R}_i(^i\boldsymbol{r}\times) & ^j\boldsymbol{R}_i \end{bmatrix} \tag{3.7}$$

$$^j\boldsymbol{X}_i^* = \begin{bmatrix} ^j\boldsymbol{R}_i & -\,^j\boldsymbol{R}_i(^i\boldsymbol{r}\times) \\ \boldsymbol{0}_{3\times3} & ^j\boldsymbol{R}_i \end{bmatrix} \tag{3.8}$$

A homogeneous transformation matrix from A to B is also described as follows:

$$^j\boldsymbol{T}_i = \begin{bmatrix} ^j\boldsymbol{R}_i & -^j\boldsymbol{R}_i(^i\boldsymbol{r}) \\ \boldsymbol{0} & 1 \end{bmatrix} \tag{3.9}$$

For a spatial vector $\boldsymbol{x}$ the cross spatial cross operator $\times$ and its dual $\times^*$ are defined as follows:

$$\boldsymbol{v} \times = \begin{bmatrix} \boldsymbol{\omega} \\ \dot{\boldsymbol{p}} \end{bmatrix} \times = \begin{bmatrix} \boldsymbol{\omega} & \boldsymbol{0} \\ \dot{\boldsymbol{p}}\times & \boldsymbol{\omega}\times \end{bmatrix} \tag{3.10}$$

$$\boldsymbol{v}\times^* = \begin{bmatrix} \boldsymbol{\omega} \\ \dot{\boldsymbol{p}} \end{bmatrix} \times^* = \begin{bmatrix} \boldsymbol{\omega} & \dot{\boldsymbol{p}}\times \\ \boldsymbol{0} & \boldsymbol{\omega}\times \end{bmatrix} \tag{3.11}$$

Given two vectors $\boldsymbol{x}, \boldsymbol{y} \in \mathbb{R}^3$, we denote with $\boldsymbol{S}(\boldsymbol{x}) \in \mathbb{R}^{3\times3}$ the skew-symmetric matrix

$$\boldsymbol{S}(\boldsymbol{x}) = \begin{bmatrix} 0 & -x_3 & x_2 \\ x_3 & 0 & -x_1 \\ -x_2 & x_1 & 0 \end{bmatrix} \tag{3.12}$$

such that $\boldsymbol{S}(\boldsymbol{x})\boldsymbol{y} = \boldsymbol{x} \times \boldsymbol{y}$, where $\times$ denotes the cross product operator in $\mathbb{R}^3$. We denoted with $^A\dot{\boldsymbol{x}}$ the temporal first order derivative and with $^A\ddot{\boldsymbol{x}}$ the temporal second order derivative of a generic vector x in A coordinates. For each link i and joint i, the considered kinematic variables are:

⋄ $\boldsymbol{v}_i$: the link spatial velocity;

⋄ q_i: the joint i position;

$\diamond$ $\dot{q}_i$: the joint i velocity;

$\diamond$ $\boldsymbol{v}_{Ji}$: the spatial velocity across joint i.

The dynamics variables are:

$\diamond$ $\boldsymbol{a}_i$: the link spatial accelerations;

$\diamond$ $\ddot{q}_i$: the joint i acceleration;

$\diamond$ $\boldsymbol{\tau}_i$: the joint i torque;

$\diamond$ $\boldsymbol{f}_i$: the spatial force transmitted to body i from $\lambda(i)$;

$\diamond$ $\boldsymbol{f}_i^B$: the net spatial force on body i;

$\diamond$ $\boldsymbol{f}_i^x$: external forces acting on body i.

All variables are expressed in body i coordinates, except for $\boldsymbol{f}_i^x$ which is convenient to express in absolute (i.e. body 0) coordinates.

Within the stochastic contest introduced to obtain the Bayesian solution of the RNEA, we adopt the following notation. Given a stochastic variable $\boldsymbol{x}$, we denote with $p(\boldsymbol{x})$ its probability density and with $p(\boldsymbol{x}|\boldsymbol{y})$ the probability density of $\boldsymbol{x}$ conditioned on the stochastic vector $\boldsymbol{y}$. Since $\boldsymbol{y}$ is associated to a deterministic function $f(\boldsymbol{x})$, with $E_{\boldsymbol{x}}[f(\boldsymbol{x})]$ we denote the expected value of $f(\boldsymbol{x})$ w.r.t. the probability distribution $p(\boldsymbol{x})$ and with $\mu_{\boldsymbol{x}}, \Sigma_{\boldsymbol{x}}$, the mean and covariance of $\boldsymbol{x}$. The probability density function of a multivariate Gaussian distribution $\boldsymbol{x} \in \mathbb{R}^n$ is $p(\boldsymbol{x}) \sim \mathcal{N}(\boldsymbol{\mu_x}, \boldsymbol{\Sigma_x})$:

$$p(\boldsymbol{x}) = (2\pi)^{\frac{n}{2}} \ |\boldsymbol{\Sigma_x}|^{-\frac{1}{2}} \ exp\left\{ -\frac{1}{2}(\boldsymbol{x} - \boldsymbol{\mu_x})^T \ \Sigma_{\boldsymbol{x}}^{-1} \ (\boldsymbol{x} - \boldsymbol{\mu}_x) \right\} \tag{3.13}$$

where $|\boldsymbol{\Sigma_x}|$ denotes the determinant of the matrix $\boldsymbol{\Sigma_x} \in \mathbb{R}^{n \times n}$. It is worth to notice that when in a multivariate normal distribution the covariance $\boldsymbol{\Sigma}$ is not a full-rank matrix, then the distribution is degenerate and does not have a density. In order to avoid the problem, it can be useful to restrict the problem on a subset of $\boldsymbol{\Sigma}$ such that the covariance matrix for this subset is positive definite.

3.3.2 Problem statement and formulation

The dynamic estimation algorithm has been originally proposed in the domain of humanoid robot control [39] and then adapted in [1] as a framework for the probabilistic estimation of whole-body human dynamics with redundant measurements. This section presents the estimation problem in details; starting from the RNEA for ID computation, the resulting equations are arranged in matrix form. Then, the estimation problem is analysed in the event that the boundary conditions for the RNEA are replaced with a set of redundant measurements and a Bayesian solution of the estimation problem is proposed.

Recursive Newton-Euler Algorithm

The ID problem is formulated in [37] as the problem of finding the forces required to produce a given acceleration and it can be summarized in this way:

$$\boldsymbol{\tau} = f\left(model, \boldsymbol{q}, \dot{\boldsymbol{q}}, \ddot{\boldsymbol{q}}\right) \tag{3.14}$$

where f indicate the ID function. Among the different ID approach used in literature [20], we choose a "top-down" approach, assuming that all quantities depending on $\boldsymbol{q}$ and $\dot{\boldsymbol{q}}$ have been precomputed, including the transformation matrices ${}^j\boldsymbol{X}_i$, ${}^j\boldsymbol{X}_i^*$. A classic efficient numerical solution of ID problem is given by the RNEA, consisting of two subparts. The first part is in charge of efficiently computing the rigid body velocities with the following recursive equation:

$$\boldsymbol{v}_{Ji} = \boldsymbol{S}_i \dot{\boldsymbol{q}}_i \tag{3.15a}$$

$$\boldsymbol{v}_i = {}^j\boldsymbol{X}_{\lambda(i)} \boldsymbol{v}_{\lambda(i)} + \boldsymbol{v}_{Ji} \tag{3.15b}$$

The second part of the RNEA computes the rigid body accelerations, forces and torques, expressed in body i coordinates:

$$\boldsymbol{a}_i = {}^j\boldsymbol{X}_{\lambda(i)} \boldsymbol{a}_{\lambda(i)} + \boldsymbol{S}_i \ddot{\boldsymbol{q}}_i + \boldsymbol{v}_i \times \boldsymbol{v}_{Ji} \tag{3.16a}$$

$$\boldsymbol{f}_i^B = I_i \boldsymbol{a}_i + \boldsymbol{v}_i \times^* I_i \boldsymbol{v}_i \tag{3.16b}$$

$$\boldsymbol{f}_i = \boldsymbol{f}_i^B - {}^i\boldsymbol{X}_0^* \boldsymbol{f}_i^X + \sum_{j \epsilon \mu(i)} {}^i\boldsymbol{X}_j^* \boldsymbol{f}_j \tag{3.16c}$$

$$\boldsymbol{\tau}_i = \boldsymbol{S}_i^T \boldsymbol{f}_i \tag{3.16d}$$

Equations (3.15a), (3.15b) and (3.16a) are propagated from $i = 0$ to (N_B-1) with initial conditions $\boldsymbol{v_0} = 0$ and $\boldsymbol{a_0} = -\boldsymbol{a_g}$, which corresponds to the gravitational spatial acceleration vector expressed in the body frame 0 (null in its first three components and equal to the gravitational acceleration in the last three). Equations (3.16b)-(3.16d) are propagated from $i = (N_B - 1)$ to 0.

RNEA matrix formulation and the measurements equation

In this subsection, we rearrange the RNEA in a matrix form. Equation (3.16) can be seen as a set of equations which the dynamic variables have to satisfy. Let us first define a spatial vector $\boldsymbol{d}$ of dynamic variables as follows:

$$\boldsymbol{d}_i = \left[\begin{array}{cccccc} \boldsymbol{a}_i^T & \boldsymbol{f}_i^{B^T} & \boldsymbol{f}_i^T & \boldsymbol{\tau}_i^T & \boldsymbol{f}_i^{xT} & \ddot{\boldsymbol{q}}_i^T \end{array} \right] \tag{3.17}$$

$$\boldsymbol{d} = \left[\begin{array}{cccc} \boldsymbol{d}_1^T & \boldsymbol{d}_2^T & \ldots & \boldsymbol{d}_{N_B}^T \end{array} \right] \tag{3.18}$$

whose dimensions are $d_i = 24 + 2n_i$ and $d = 24N_B + 2n$ respectively. Given (3.17) and (3.18), Equations (3.16) can be compactly written in the following matrix equation:

$$D(q, \dot{q})d + b_D(q, \dot{q}) = 0 \tag{3.19}$$

where D is a block matrix $\epsilon \ \mathbb{R}^{(12N_B+n)\times(18N_B+2n)}$ and b_D is a vector $\epsilon \ \mathbb{R}^{(12N_B+n)}$ and we explicitly indicate the fact that both D and b_D can be expressed as a function of q and $\dot{q}$. D matrix and b_D vector can be build as:

$$D = \begin{bmatrix} D_{1,1} & \dots & D_{1,N_B} \\ \vdots & \ddots & \vdots \\ D_{N_B,1} & \dots & D_{N_B,N_B} \end{bmatrix} \quad b = \begin{bmatrix} b_1 \\ \vdots \\ b_{N_B} \end{bmatrix} \tag{3.20}$$

In particular:

$$D_{i,i} = \begin{bmatrix} -1 & 0 & 0 & 0 & S_i \\ I_i & -1 & 0 & -{}^iX_0^* & 0 \\ 0 & S_i^T & -1 & 0 & 0 \end{bmatrix} \tag{3.21}$$

$$\forall j \ \epsilon \ \mu(i) \ D_{i,j} = \begin{bmatrix} 0 & 0 & 0 & 0 & 0 \\ 0 & -{}^iX_j^* & 0 & 0 & 0 \\ 0 & 0 & 0 & 0 & 0 \end{bmatrix} \tag{3.22}$$

$$\forall j \ \epsilon \ \lambda(i) \ D_{j,i} = \begin{bmatrix} {}^iX_{\lambda(j)} & 0 & 0 & 0 & 0 \\ 0 & 0 & 0 & 0 & 0 \\ 0 & 0 & 0 & 0 & 0 \end{bmatrix} \tag{3.23}$$

$$\text{if } \lambda(i) = 0 \ b_i = \begin{bmatrix} {}^iX_0 a_0 + v_i \times S_i \dot{q}_i \\ v_i \times^* I_i v_i \\ 0 \end{bmatrix} \tag{3.24}$$

$$\text{if } \lambda(i) \neq 0 \ \ b_i = \begin{bmatrix} v_i \times S_i \dot{q}_i \\ v_i \times^* I_i v_i \\ 0 \end{bmatrix} \tag{3.25}$$

Remarkably, Equation (3.19) represents the set of linear constraints in d and, in a sense, ID computation consists of computing d given f_i^x and $\ddot{q}_i$.

Over constrained Netwon-Euler equations

Moving away from the classic approach, the boundary conditions to obtain a solution of the Equation (3.19) are replaced with measurements coming from sensors. The multiple noisy and redundant

measurements $\boldsymbol{y_m} \in \mathbb{R}^y$ are linked to $\boldsymbol{d}$ by the equation:

$$Y(\boldsymbol{q}, \dot{\boldsymbol{q}})\boldsymbol{d} + \boldsymbol{b_Y}(\boldsymbol{q}, \dot{\boldsymbol{q}}) = \boldsymbol{y_m} \tag{3.26}$$

The $\boldsymbol{Y}$ matrix depends on the number of sensors $N_S = \sum_i N_{Si}$ used for each link i, and its structure is:

$$\boldsymbol{Y} = \begin{bmatrix} \boldsymbol{Y_1} & ... & \boldsymbol{Y_{N_B}} \end{bmatrix}^T \tag{3.27}$$

$$\boldsymbol{Y_i} = \begin{bmatrix} \boldsymbol{Y_{i,1}^T} & ... & \boldsymbol{Y_{i,N_{S_i}}^T} \end{bmatrix}^T \tag{3.28}$$

where $\mathbb{R}^{N_S \times d}$ and $\mathbb{R}^{N_{S_i} \times d_i}$.

The structure of the bias vector $\boldsymbol{b_Y}$ is also defined with the same methodology:

$$\boldsymbol{b_Y} = \begin{bmatrix} \boldsymbol{b_{Y_1}} & ... & \boldsymbol{b_{Y_{N_B}}} \end{bmatrix}^T \tag{3.29}$$

$$\boldsymbol{b_{Y_i}} = \begin{bmatrix} \boldsymbol{b_{Y_{i,1}}^T} & ... & \boldsymbol{b_{Y_{i,N_{S_i}}}^T} \end{bmatrix}^T \tag{3.30}$$

whose dimensions are N_S and N_{S_i} respectively.

Combining properly (3.19) and (3.26), we obtain:

$$\begin{bmatrix} \boldsymbol{D}(\boldsymbol{q}, \dot{\boldsymbol{q}}) \\ \boldsymbol{Y}(\boldsymbol{q}, \dot{\boldsymbol{q}}) \end{bmatrix} \boldsymbol{d} + \begin{bmatrix} \boldsymbol{b_D}(\boldsymbol{q}, \dot{\boldsymbol{q}}) \\ \boldsymbol{b_Y}(\boldsymbol{q}, \dot{\boldsymbol{q}}) \end{bmatrix} = \begin{bmatrix} \boldsymbol{0} \\ \boldsymbol{y_m} \end{bmatrix} \tag{3.31}$$

$$\text{rank} \begin{pmatrix} \boldsymbol{D}(\boldsymbol{q}, \dot{\boldsymbol{q}}) \\ \boldsymbol{Y}(\boldsymbol{q}, \dot{\boldsymbol{q}}) \end{pmatrix} = d \tag{3.32}$$

where the assumption of the rank guarantees that the available measurements $\boldsymbol{y_m}$ give enough constrains on $\boldsymbol{d}$. In this system $\boldsymbol{d}$ is over constrained and so an exact solution of (3.31) does not exist.

There are several approaches to solve this system; our solution, proposed in the next subsection, is to estimate $\boldsymbol{d}$ in a Bayesian framework in which it is possible to weigh differently the constraints according to the available sensors accuracy.

Bayesian solution of the Newton-Euler equations

The first assumption for adopting MAP estimation approach is to consider $\boldsymbol{d}$ and $\boldsymbol{y}$ as stochastic variables with Gaussian distributions. Let $\boldsymbol{d}$ and $\boldsymbol{y}$ be two random vectors. Their joint probability can be defined by using the factorisation $p(\boldsymbol{d}, \boldsymbol{y}) = p(\boldsymbol{d})p(\boldsymbol{y}|\boldsymbol{d})$ being $p(\cdot)$ the probability density and $p(\cdot|\cdot)$ its conditioned version. Given $p(\boldsymbol{d}, \boldsymbol{y})$, it is possible to compute an estimation of $\boldsymbol{d}$ given $\boldsymbol{y}$ by exploit the MAP estimator as follows:

$$d_{MAP} = \arg\max_{\boldsymbol{d}} p(\boldsymbol{d}|\boldsymbol{y}) \ \alpha \ p(\boldsymbol{d}, \boldsymbol{y_m}) \tag{3.33}$$

where we applied Bayes rule, i.e. $p(\boldsymbol{d}|\boldsymbol{y}) = p(\boldsymbol{d}, \boldsymbol{y})/p(\boldsymbol{y})$, and where we omitted the term $p(\boldsymbol{y})$ since it does not depend on $\boldsymbol{d}$ and does not contribute to the optimization. With Gaussian distributions the maximum a-posteriori solution coincides with the conditioned mean $E[\boldsymbol{d}|\boldsymbol{y} = \boldsymbol{y}_m]$ and the minimum variance estimator. Let us first give an expression for $p(\boldsymbol{Y}|\boldsymbol{d})$:

$$p(\boldsymbol{Y}|\boldsymbol{d}) \sim \mathcal{N}(\boldsymbol{\mu_y}, \boldsymbol{\Sigma_y}) \quad \boldsymbol{\mu_y} = \boldsymbol{Y}(\boldsymbol{q}, \dot{\boldsymbol{q}})\boldsymbol{d} + \boldsymbol{b_Y} \tag{3.34}$$

which implicitly makes the assumption that the measurements from Equation (3.26) are affected by a Gaussian noise with zero mean and covariance $\boldsymbol{\Sigma_y}$. Its probability distribution is:

$$p(\boldsymbol{Y}|\boldsymbol{d}) \ \alpha \ exp\left\{-\tfrac{1}{2}(y - \boldsymbol{\mu}_y)^T \boldsymbol{\Sigma}_y^{-1}(y - \boldsymbol{\mu}_y)\right\} \tag{3.35}$$

The second assumption is to define a probability density for $\boldsymbol{d}$ with the following distribution $p(\boldsymbol{d}) \sim \mathcal{N}(\boldsymbol{\mu}_D, \boldsymbol{\Sigma_D})$:

$$p(\boldsymbol{d}) \ \alpha \ exp\left\{-\tfrac{1}{2}\boldsymbol{e}(\boldsymbol{d})^T \boldsymbol{\Sigma}_D^{-1}\boldsymbol{e}(\boldsymbol{d})\right\} \tag{3.36}$$

taking into account constraints in Equation (3.19) with $\boldsymbol{e}(\boldsymbol{d}) = \boldsymbol{D}(\boldsymbol{q}, \dot{\boldsymbol{q}})\boldsymbol{d} + \boldsymbol{b}_D$. The role of $\boldsymbol{\Sigma_D}$ is to establish how much the dynamical model (3.19) should be considered exact but this choice leads to a degenerate normal distribution and a term of regularization has to be adopted. For example, if we have a Gaussian prior knowledge on $\boldsymbol{d}$ in the form of $p(\boldsymbol{d}) \sim \mathcal{N}(\boldsymbol{\mu}_d, \boldsymbol{\Sigma_d})$ distribution, we can reformulate Equation (3.36) as $p(\boldsymbol{d}) \sim \mathcal{N}(\bar{\boldsymbol{\mu}}_D, \bar{\boldsymbol{\Sigma}}_D)$:

$$p(\boldsymbol{d}) \ \alpha \ exp\left\{-\tfrac{1}{2}\left[\ \boldsymbol{e}(\boldsymbol{d})^T \boldsymbol{\Sigma}_D^{-1} \ \boldsymbol{e}(\boldsymbol{d}) + (d - \boldsymbol{\mu}_d)^T \boldsymbol{\Sigma}_d^{-1} \ (d - \boldsymbol{\mu}_d) \ \right]\right\} \tag{3.37}$$

with:

$$\bar{\boldsymbol{\Sigma}}_D = \left(\boldsymbol{D}^T \boldsymbol{\Sigma}_D^{-1} \boldsymbol{D} + \boldsymbol{\Sigma}_d^{-1}\right)^{-1} \tag{3.38a}$$

$$\bar{\boldsymbol{\mu}}_D = \bar{\boldsymbol{\Sigma}}_D \left(\boldsymbol{\Sigma}_d^{-1} \boldsymbol{\mu}_D - \boldsymbol{D}^T \boldsymbol{\Sigma}_D^{-1} \boldsymbol{b}_D\right)^{-1} \tag{3.38b}$$

Given Equations (3.35) and (3.37), we can build the joint probability as $p(\boldsymbol{d}|\boldsymbol{Y}) \sim \mathcal{N}(\boldsymbol{\mu}_{d|y}, \boldsymbol{\Sigma}_{d|y})$ being

$$\boldsymbol{\Sigma}_{d|y} = \left(\bar{\boldsymbol{\Sigma}}_D^{-1} + \boldsymbol{Y}^T \boldsymbol{\Sigma}_y^{-1} \boldsymbol{Y}\right)^{-1} \tag{3.39a}$$

$$\boldsymbol{\mu}_{d|y} = \boldsymbol{\Sigma}_{d|y}\left[\boldsymbol{Y}^T \boldsymbol{\Sigma}_y^{-1}(\boldsymbol{Y} - \boldsymbol{b}_Y) + \bar{\boldsymbol{\Sigma}}_D^{-1} \bar{\boldsymbol{\mu}}_D\right] \tag{3.39b}$$

where Equation (3.39b) is exactly the estimation $\boldsymbol{d}_{MAP}$.

The benefits of MAP algorithm

The benefits of multi-sensor data fusion for solving the dynamic estimation problem can be observed by characterizing the effects of data fusion on the covariance of associated estimator. The general idea is that the more sensors we use in the estimation, the better the estimation itself will be. Since we are interested in the analytic solution of MAP, the estimator must have the following covariance (combining Equations (3.40) and (3.38a)):

$$\boldsymbol{\Sigma}_{d|y} = \left(\boldsymbol{D}^T \boldsymbol{\Sigma}_D^{-1} \boldsymbol{D} + \boldsymbol{\Sigma}_d^{-1} + \boldsymbol{Y}^T \boldsymbol{\Sigma}_y^{-1} \boldsymbol{Y} \right)^{-1} \tag{3.40}$$

Assuming multiple measurements $\boldsymbol{Y}_1 = \boldsymbol{Y}_1\,\boldsymbol{d} + \boldsymbol{b}_{Y_1}, ..., \boldsymbol{Y}_m = \boldsymbol{Y}_m\,\boldsymbol{d} + \boldsymbol{b}_{Y_m}$ statistically independent, this implies a diagonal structure to the matrix $\boldsymbol{\Sigma}_y^{-1}$. Thus, we have:

$$\boldsymbol{Y}^T \boldsymbol{\Sigma}_y^{-1} \boldsymbol{Y} = [\boldsymbol{Y}_1 \ldots \boldsymbol{Y}_m] \begin{bmatrix} \boldsymbol{\Sigma}_{y_1}^{-1} & \ldots & 0 \\ \vdots & \ddots & \vdots \\ 0 & \ldots & \boldsymbol{\Sigma}_{y_m}^{-1} \end{bmatrix} \begin{bmatrix} \boldsymbol{Y}_1 \\ \vdots \\ \boldsymbol{Y}_m \end{bmatrix} \tag{3.41}$$

$$\Rightarrow \boldsymbol{Y}^T \boldsymbol{\Sigma}_y^{-1} \boldsymbol{Y} = \boldsymbol{Y}^T \boldsymbol{\Sigma}_{y_1}^{-1} \boldsymbol{Y} + \ldots + \boldsymbol{Y}^T \boldsymbol{\Sigma}_{y_1}^{-1} \boldsymbol{Y} \tag{3.42}$$

With an abuse of notation, let us denote with $\boldsymbol{d}|\boldsymbol{Y}_i$ the estimator which exploits all measurements up to $i - th$, *i.e.* $y_1, ..., y_i$. The addition of one measurement induces changes in the associated covariance matrix according to the following recursive equation:

$$\boldsymbol{\Sigma}_{d|y_i}^{-1} = \boldsymbol{\Sigma}_{d|y_i-1}^{-1} + \boldsymbol{Y}_i^T \boldsymbol{\Sigma}_{y_i}^{-1} \boldsymbol{Y}_i \tag{3.43}$$

where, for $i = 1$, the initial condition is $\boldsymbol{\Sigma}_{d|y_0}^{-1} = \boldsymbol{D}^T \boldsymbol{\Sigma}_D^{-1} \boldsymbol{D} + \boldsymbol{\Sigma}_d^{-1}$. Considering the Weyl inequality for the largest eigenvalue λ_1 of Equation (3.44):

$$\frac{\lambda_N(\boldsymbol{\Sigma}_{d|y_i-1})}{1 + \lambda_N(\boldsymbol{\Sigma}_{d|y_i-1})\lambda_1(\boldsymbol{Y}_i^T\boldsymbol{\Sigma}_{y_i}^{-1}\boldsymbol{Y}_i)} \leq \lambda_N(\boldsymbol{\Sigma}_{d|y_i}) \leq \frac{1}{L_1} \tag{3.44}$$

$$L_1 = \max_{i+j=N+1} \left[\frac{1}{\lambda_{N-i+1}(\boldsymbol{\Sigma}_{d|y_i-1})} + \lambda_j(\boldsymbol{Y}_i^T\boldsymbol{\Sigma}_{y_i}^{-1}\boldsymbol{Y}_i) \right] \tag{3.45}$$

The maximum benefit is obtained by lowering the upper bound on $\lambda_1(\boldsymbol{\Sigma}_{d|y_i})$. Trivially, this can be obtained by choosing high values for all the eigenvalues of $\boldsymbol{Y}_i^T \boldsymbol{\Sigma}_{y_i}^{-1} \boldsymbol{Y}_i'$. Obviously, this is not always possible and benefits can be obtained by maximizing L_1.

In summary, inputs and outputs of all method employed (i.e. OpenSim IK tool, OpenSim ID tool and MAP algorithm) are synthesized in Table 3.1.

Table 3.1: Inputs required and outputs generated by OpenSim IK tool, OpenSim ID tool and MAP algorithm.

Method	Inputs	Outputs
OpenSim IK	marker trajectories biomechanical model	joint trajectories
OpenSim ID	joint trajectories biomechanical model external load data	joints torques and forces
MAP algorithm	joint trajectories biomechanical model external load data joint velocities and accelerations[1] other sensors measurements	dynamic variables (3.17)

3.4 Sensors

As mentioned before, the algorithm we propose for the estimation of ID consists in replacing the classic boundary conditions in the Newton-Euler equations with the measurements coming from available sensors. In addition to the limited computational complexity, the key feature of this strategy is that sensors fusion and redundancy exploitation allow to significantly improve the estimation accuracy. The proposed framework encompasses three sources of measurements:

- ◇ a full-body wearable lycra suit provided by Xsens technology equipped with 17 inertial measurements units that include accelerometers, gyroscopes and magnetometers;

- ◇ two standard force plates AMTI OR6 mounted on the ground;

- ◇ iCub, a full-body humanoid robot provided with whole-body distributed F/T sensors, accelerometers, gyroscopes and tactile sensors.

3.4.1 Xsens

The XSens MVN motion-capture system can be used in a wide range of scenarios, within the range of the wireless link. Subjects are not forced to a specific measurement volume and their movements

---

[1]Computed as joints angles first and second derivatives.

can be measured in a familiar environment while performing their tasks - as in daily life. There is no need to install or place any fixed infrastructure, so the total set-up time (including calibration) takes less than 10 minutes. There is no limitation by occlusion with neither objects surrounding nor other persons interacting with the subject. The system consists of 17 miniature inertial and magnetic measurement units called MTx (see Figure 3.6) that integrates 3-D gyroscopes measuring angular velocities, 3-D linear accelerometers measuring accelerations including gravitational acceleration and 3-D magnetometers measuring the earth magnetic field. Specification about MTx sensors are displayed in Table 3.2. All these sensor modules are connected to the Xbus Masters, that synchronizes all sensor sampling, provides sensors with power and handles the wireless communication with the PC or laptop. For quick and convenient placement, the sensors and cables are integrated in a lycra suit (see Figure 3.5) and the Xbus Masters are mounted on the back [40].
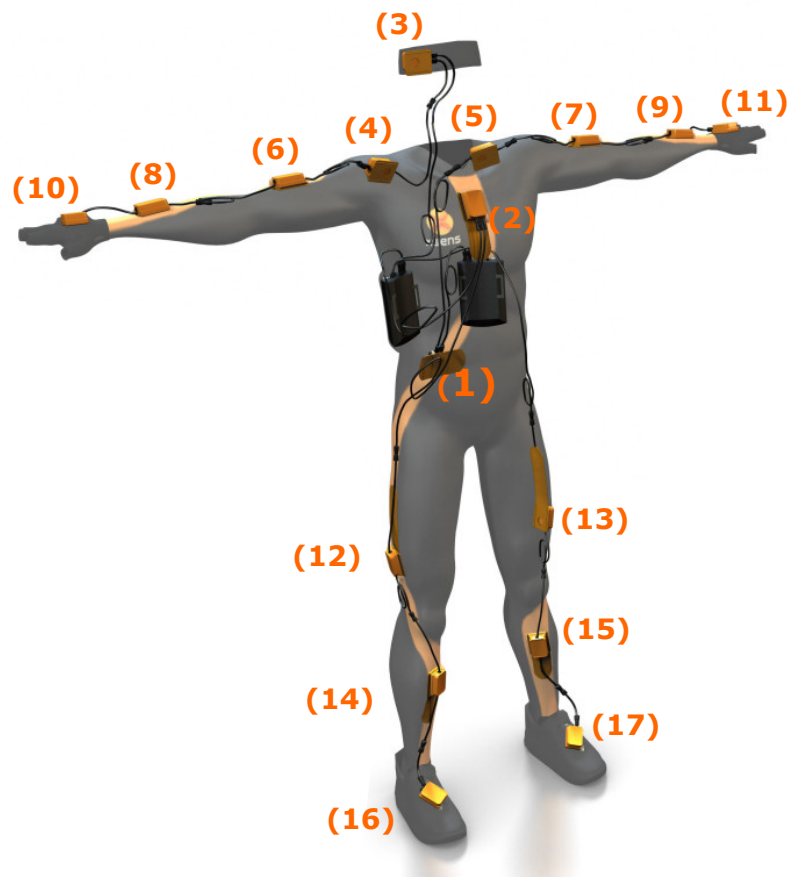
Figure 3.5: Wearable lycra suit provided by Xsens embedding 17 IMUs with their relative labels.

The system runs in real-time with a maximum update rate for all kinematics of 240 Hz. In order to estimate body segment orientation and position changes, gyroscope and accelerometer signals are integrated and continuously updated by using a biomechanical model of the human body. Its development is a functionality provided by Xsens system software; the model is employed within the analysis

but it is not investigable by the user. Information about the biomechanical model can be found in [41]. It consists of 23 segments (pelvis, L5, L3, T12, T8, neck, head, and right and left shoulder, upper arms, fore arms, hands, upper legs, lower legs, feet and toes) linked together by 22 joints with 3 DoFs, in which the sensor modules are attached as shown in Table 3.6. Joint origins are defined in the centre of the functional axes with the directions of the $x - y - z$ axes being related to functional movements (see Figure 3.7).

	Link	IMUs
Trunk	Pelvis	(1)
	L5	
	L3	
	T12	
	T8	(2)
Head	Neck	
	Head	(3)
Arm	Shoulder	(4)-(5)
	UpperArm	(6)-(7)
	ForeArm	(8)-(9)
	Hand	(10)-(11)
Leg	UpperLeg	(12)-(13)
	LowerLeg	(14)-(15)
	Foot	(16)-(17)
	Toe	

Figure 3.6: On the left, an Xsens IMU is shown. Table on the right depicts the set of links for human model with the relative parent joints and associated sensors.

34
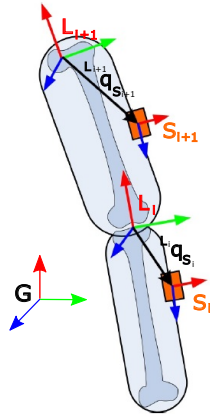
Figure 3.7: Orientation and position of the sensor w.r.t link RF. S_i is the sensor RF, L_i is the link RF, $^{L_i}q_{S_i}$ is the quaternion that express the transformation between the sensor and the link.

When attaching sensors to a body, the initial pose between the sensors and body segments is unknown. Moreover, by assessing distances between body segments by numerical integration of acceleration is difficult because of the unknown initial position. In order to overcome these problems and express segment kinematics in the global frame, a calibration procedure has to be performed to determine the orientation of the sensor w.r.t. the segment (Figure 3.7) and the relative distances between joints. During this procedure, the subject stands in a-priori known position, called N-pose, whose configuration is showed in Figure 3.8.

Figure 3.8: Xsens model of a subject performing N-pose.

The quaternion $^{L}q_{S}$, from which it is possible to obtain the rotation matrix between the sensor and body segment, is determined by matching the orientation of the sensor in the global frame $^{G}q_{S}$

35

Table 3.2: Xsens IMUs specifications [41].

Specification	Numerical Value
Sampling rate[2]	1800 Hz
Operating Voltage	4.5-30 V
Power consumption	350 mW
Operating temperature range	-40 to + 85 °C
Gyroscopes bias stability	20 deg/h
Timing accuracy	10 $10^{-6}s$
Static accuracy (roll/pitch)	<0.5 deg
Static accuracy (heading)	<1 deg
Dynamic accuracy	2 deg RMSE
Angular resolution	0.05 deg

with the known orientation of each segment $^G q_L$ in this pose as follows:

$$^G q_L = {}^G q_S \otimes {}^L q_S^* \tag{3.46}$$

where $\otimes$ denotes a quaternion multiplication and $*$ denotes the complex conjugate of the quaternion. Estimates of joints position are obtained by measuring several body dimensions.

After the calibration procedure, each sensor orientation and position can be estimated respectively by integrating the gyroscope data and double integrating the accelerometer data in time. Rate gyroscopes primary measure angular velocity $\boldsymbol{\omega}$. If this angular velocity is integrated over time, it provides the change in orientation w.r.t. an initially known one:

$$^G \dot{q}_{S,t} = \frac{1}{2} {}^G q_{S,t} \otimes \boldsymbol{\Omega}_t \tag{3.47}$$

where $^G \dot{q}_{S,t}$ is the quaternion describing the rotation from sensor S to global frame G at time t and $\boldsymbol{\Omega}_t = (0, \omega_x, \omega_y, \omega_z)^T$ is the quaternion representation of the angular velocity $\boldsymbol{\omega_t}$. Linear accelerometers measure the vector of acceleration $\boldsymbol{a}$ and gravitational acceleration $\boldsymbol{g}$ in sensor coordinates. If the orientation of the sensor $^G q_{S,t}$ is known, the quantities measured by the sensor can be expressed in the global reference system G:

$$^G \boldsymbol{a}_t - {}^G \boldsymbol{g}_t = {}^G q_{S,t} \otimes ({}^S \boldsymbol{a}_t - {}^S \boldsymbol{g}_t) \otimes {}^G q *_{S,t} \tag{3.48}$$

After removing the gravity component, the acceleration $\boldsymbol{a}_t$ can be integrated once to velocity $\boldsymbol{v}_t$ and twice to position $\boldsymbol{p}_t$.

To provide 6 full DoFs tracking of the subject, the information coming from the sensors are translated to body segments using the biomechanical model of the subject and the sensor orientation and position w.r.t. the segment, found in the calibration step.

---

[2]Maximum IMUs update rate depends on amount of IMUs used.

Because of sensor noise due to skin and soft tissue artefacts, the uncertainty of the joint position and rotation grows after building the kinematic structure for the subject model. By exploiting the knowledge that two segments are on average connected but with a statistical uncertainty, these artefacts are corrected by using the joint measurement updates.

The Xsens sensor system provides the 3-D position, velocity, acceleration, orientation, angular velocity and angular acceleration of all the 23 body segment w.r.t. a global (earth-fixed) reference coordinate system G. The Euler angles ZXY (flexion/extension, abduction/adduction, internal/external rotation) are extracted for all the 22 joints. For the shoulder, also the XZY sequence is available. The positions and the trajectories of some points of interest, the anatomical landmarks, are provided in the links RFs. These points are not measured directly as in traditional optical motion-capture systems, but computed by using the measured segment kinematics in combination with the anatomical model. The global RF G and the RFs L of some links (takes as examples) are shown in Figure 3.9.
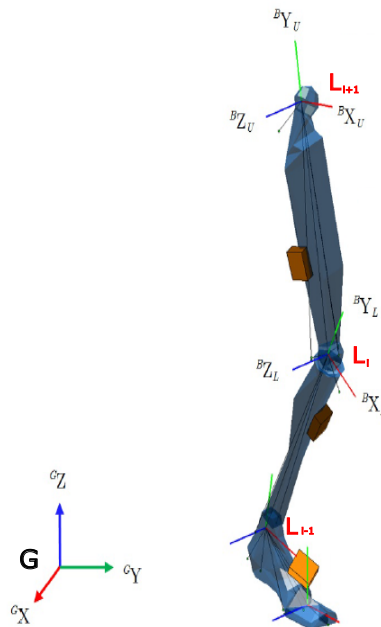
Figure 3.9:   The global RF G and the RFs L of the links that compose the leg (take as an example) are shown.

The CoM is estimated on the segment positions and orientations together with a body mass distribution model.

The software provided with the system, MVN Studio is an easy-to-use GUI and allows the visualization of the subject movements in real-time and from previous recordings. The data can be stored in the native format MVN which contains all raw sensor data, and MVNX, the MVN Open xml format which contains all kinematic data and can be used for post-processing.

3.4.2 Force plates

While performing the requested tasks the human subject stands with his feet on two standard AMTI Biomechanics model OR6-7 force plates mounted on the ground, one foot per platform. These platforms are specifically designed for an accurate measurement of GRFs. They measure the three orthogonal force components along the $x - y - z$ axes, and the moments about the three axes, producing a six dimensional measurements vector at a frequency of 1 kHz. The OR6-7 platforms weigh 1000 *pounds* and present the specifications listed in Table 3.3.

Table 3.3: AMTI OR6-7 force plates specifications (data-sheet).

Specification	Numerical Value
Maximum Excitation Voltage	10 V
Crosstalk	< 2 %
Operating Temperature Range	-17 to 52 °C
Fx, Fy, Fz Hysteresis	± 0.2 % Full scale output
Fx, Fy, Fz Nonlinearity	± 0.2 % Full scale output
Fx, Fy Capacity	2225 N
Fz Capacity	4450 N
Mx My Capacity	1100 Nm
Mz Capacity	600 Nm
Fx, Fy Natural Frequency	300 Hz
Fz Natural Frequency	480 Hz
Fx, Fy Sensitivity	0.67 $\mu V/(VN)$
Fz Sensitivity	0.17 $\mu V/(VN)$
Mx, My Sensitivity	1.59 $\mu V/(VNm)$
Mz Sensitivity	3.38 $\mu V/(VNm)$

They use strain gages mounted on four precision strain elements in a patented design to measure forces and moments. As with most conventional strain gage transducers, bridge excitation and signal amplification are required. To this purpose, AMTI strain gage amplifiers, high gain devices which provide excitation and amplification for multiple channels, are employed. Thanks to high sensitivity, low crosstalk, repeatability and long term stability, these platforms can be used for research and clinical studies. For automated data collection and reduction, the AMTI software NetForce is employed. Orthogonal and 3-D projections of the force plates along with the RF are depicted respectively in Figure 3.10(a) and Figure 3.10(b).

(a)   (b)
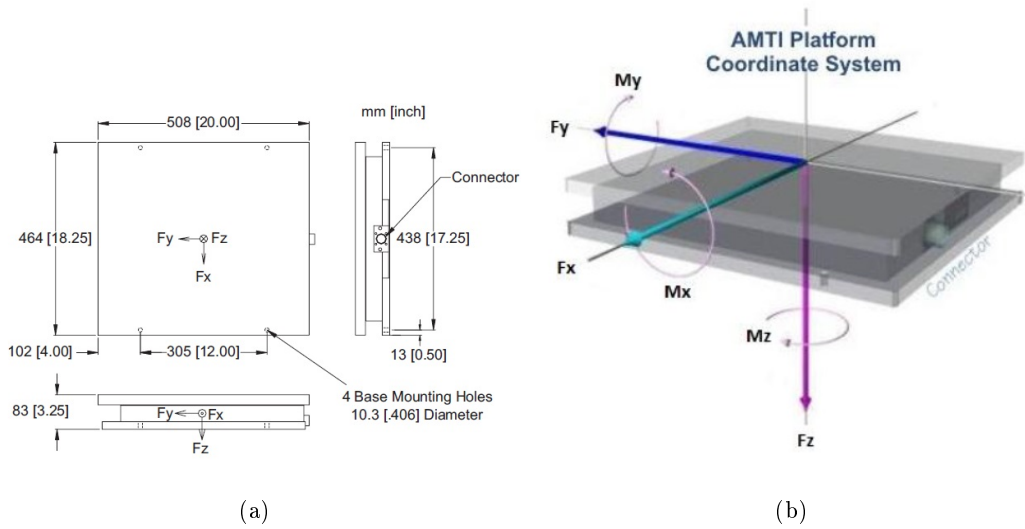
Figure 3.10: (a) shows the orthogonal projections of the platforms including the geometric dimensioning. (b) depicts a 3-D projection again with the RF

3.4.3   iCub

The employed robotic platform for pHRI experiments is the humanoid iCub, a state-of-the-art open source robotic platform for research in cognitive robotics, extensively described in [42]. The iCub humanoid robot is 104 cm tall, weighing 33 kg and possesses in total 53 DoFs, most of these located in the hands. The more important are the 23 distributed in the following way:

- ◇ 6 DoFs for each legs;

- ◇ 3 DoFs for the torso;

- ◇ 4 DoFs for the upper arm, 3 of which in the shoulder and one in the elbow.

The torso and shoulder joints are mechanically coupled and driven by tendon mechanisms. All the 23 joints are powered by brushless electric motors equipped with harmonic drive gears. A peculiarity of iCub is the huge array of sensors available: F/T sensors, accelerometers, gyroscopes, a distributed tactile skin, two cameras and microphones. The sensors considered in our application are the F/T sensors. iCub possesses 6 six-axes F/T sensors whose location is depicted in Figure 3.11(a). In particular, two of them are mounted at the shoulder, the other four respectively at the hip and at the ankle.

iCub also encompasses distributed tactile sensors, the artificial skin, which provides information about both the location and the intensity of the contact forces. As can be noticed, the skin is distributed on the torso, arms, the palm and fingertips of the hands and legs. For the fact that iCub is not provided with joints torque sensors, the F/T sensors and the skin are used to provide an estimation of both the internal torques and external forces [43]. Finally, a commercial inertial
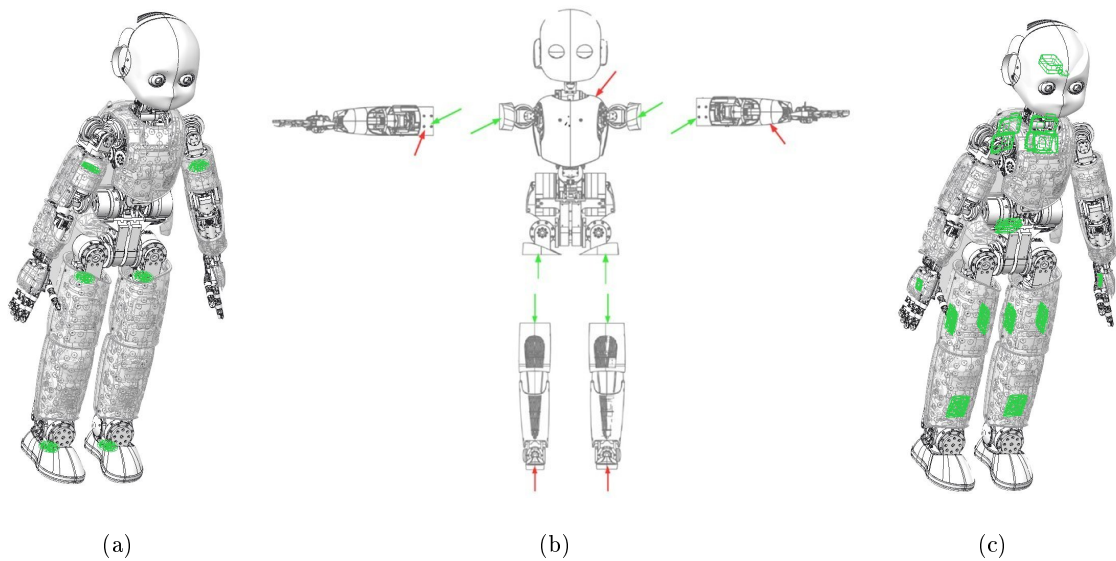
Figure 3.11:   (a) Shows the F/T sensors location while (b) depicts the internal (green arrows) and external (red arrows) wrenches that can be measured. Finally (c) represents the Inertial Measurements Units (IMUs) locations.

sensor providing acceleration and angular velocity information is mounted on the head along with whole-body distributed gyroscopes and accelerometers, as can be seen in Figure 3.11(c). Data coming directly from the artificial skin and inertial sensors are not considered in our application.

Since an infrastructure of computers is necessary in order to control the robot, the software Yet Another Robot Platform (YARP) [44] is employed. YARP is a middle-ware software whose main purpose is to allow seamless communication between "applications", which can reside on different computers. Furthermore, it provides interfaces to interact with physical devices independently from the actual implementation, thus facilitating code reuse and modularity. iCub functionalities are based on YARP and the acquisitions from the different sensors and motor controllers are provided through YARP interfaces. On top of the YARP middle-ware, an additional software layer called Whole-Body Interface is available [44]. The objective of this set of protocols is to simplify the writing of Whole-body controllers. It wraps dynamic computations such as the estimation of the mass matrix or ID, together with the possibility to interface with the robot, acquiring the state and commanding the actuators. For our application the Whole-Body Interface is used in order to acquire the data about the state of the robot and the data acquired by the F/T sensors during the pHRI experiments.

Table 3.4: List of the data extracted from the sensing systems employed for the analysis (i.e. Xsens system, force plates and iCub) with the RF which they ar expressed in.

Sensing system	Data extracted	RF
Xsens system	links 3-D positions and orientations	G (see Figure 3.9)
	links 3-D linear and angular velocities	G
	links 3-D linear and angular accelerations	G
	joints euler angles ZXY	-
	time data associated to each frame	-
	anatomical landmarks positions	L (see Figure 3.9)
	anatomical landmarks trajectories	L
Force plate	measured wrenches	forceplate RFs
iCub	revolute joints angles	-
	measured wrenches (by F/T sensors)	relative links RFs

In summary, the data coming from the three measurements sources (i.e. Xsens system, force plates and iCub) and the RF they are expressed in, are synthesized in Table 3.4.

3.5   Biomechanical Model

In the contest of movement analysis, models of the agents involved in the selected task are required. While the robot model is supplied by the iCub open source robotic platform, a 48 DoFs model, is developed for the human. This model is an extension of the 3 DoFs model employed in [1] (starting point of our study) and it allows to analysed more complex movements since all the biological DoFs are contemplated. In the next section, after providing an overview of human body modelling issues, we describe in detail the links, the joints and the kinematic tree which compose our model.

In the past decade computational models have become very popular in the field of biomechanics due to exponentially increasing computational power. The information provided by measurement systems is very important for investigating the mechanics of movements, but it is not sufficient to gain insight into the mechanical behaviour of the inner human body. The only possible way to answer the questions related to the human body, is to set up mechanical models of the human body or at least of human body parts. It is worth to notice that measurement systems still plays an important role: the

information provided by the measurements is either input for a model (e.g. reaction forces acting on the foot) or used to validate the model (e.g. comparing the simulation results with EMG data) [45].

Employing biomechanical models, the basic understanding of the analysed system can be simplified. Modelling can be thought of as a process of enrichment and enhancement: one should begin with a model that is distinct from reality and progressively move toward a more elaborate model that reflects the complexity of the actual situation. Through a process of system components analysis, the model is expanded and a greater understanding of component interaction is gained. To achieve these objectives, a model has to posses several features: *i*) it should be robust, *ii*) it should display the essence of the system under a variety of circumstances, *iii*) it should represent reality and it should have clinical relevance or workplace applications [46].

Biomechanical models can roughly be subdivided into two groups: multi-body models and numerical models using finite elements method (FEM) or computational fluid dynamics. Both types of models have their own advantages and disadvantages: numerical models enable the computation of the whole body deformation, whereas multi-body models only provide forces at a limited number of body points. Yet, the price to pay for taking into account this deformation is a much higher demand in terms of computational power for the FEM [45].

In our work, we focus on multy-body models which are systems composed by solid bodies, or links, connected to each other by joints that restrict their relative motion. There are two different methods which employ multi-body systems as inputs: *i*) *forward approach* or the analysis of how mechanical systems move under the influence of forces and *ii*) *inverse approach* where the aim is to find what forces are necessary to make the mechanical system move in a specific manner.

The biomechanical model in this contest is employed in the field of the analysis of human movements: a more complex model w.r.t. the one used in [1] is introduced in order to improve the accuracy of the estimation of the dynamics variables, starting from the measurements of kinematics quantities.

3.5.1 Inertial parameters estimation

In order to design a biomechanical model, body segment inertial parameters (model mass, centroid and moments of inertia) are required. We remind that moments of inertia are expressed through the inertia tensor. The inertia tensor can be defined in the system $x - y - z$ whose axes correspond to the principal axes of inertia of the body considered; in this case, it is equal to:

$$
\boldsymbol{I} = \begin{bmatrix} I(xx) & 0 & 0 \\ 0 & I(yy) & 0 \\ 0 & 0 & I(zz) \end{bmatrix}
\tag{3.49}
$$

where $I(xx)$, $I(yy)$ and $I(zz)$ are the principal moments of inertia. These ones are the only computed for the body segments that compose our model.

Two methods commonly used for estimating inertial quantities are regression equations and geometric approximation [47].

The former technique is based on regression equations derived from cadaveric measurements, computed tomography, plain radiography, or magnetic resonance imaging data from a finite set of specimens. The regression equation technique is more popular due to it being simpler to implement and use. For example, [48] contains tables of data for average male and female segment parameters which can be scaled appropriately according to an individual height, mass and segment lengths. This approach can be considered to extrapolate from an average and it is known to produce inaccurate results over a disparate population of body types ([49], [50]), therefore it is usually avoided.

The geometric approximation technique uses in-field measurements of an individual mapped onto a 3-D geometric model to derive mass and related properties from certain shape and density assumptions. In [15] the earliest geometric model of a humanoid was proposed, consisting of fifteen homogeneous solid shapes including ellipsoids, truncated cones, and elliptic cylinders. Twenty-five anthropometric measurements were required to calculate the properties of the model. The authors of [51] noted the inadequacy of using homogeneous and regular segments in model employed in [15] since segments can be subject to significant shape and density fluctuations along their length. Their work then proposed 2 *cm* elliptical slices of the human body measured using photometric means. The accuracy of estimating segment masses was significantly improved over the method used in [15]. In [52] a remarkably detailed seventeen segment 3-D geometrical model of the human body was developed with the same motivation, but due to its complexity, this model has rarely been used by other researchers in the field. Previous work [15] is simple but inaccurate, while the work [17] using the general "stadium solid" shape, forms a middle ground between ease of modelling and accuracy. This technique is limited by the number of measurements that can be practically taken on an individual and the complexity of the geometry used to model their body shape.

A comparison described in [53] between the regression equation technique and geometric modelling (although not including [52]) showed that the more complex geometric models produce more accurate results, especially when non-uniform densities are used; although the model employed in [52] has its flaws it is the most complete geometric model yet developed.

3.5.2   Human biomechanical model

To design the biomechanical model of the human body the following assumptions have been made:

⬦ the human body is represented by a set of rigid bodies of simple geometric shape (boxes, cylinders and spheres) and uniform density;

⬦ the joints have one, 2 or 3 DoFs, depending on the anatomical characteristic of the relative biological joint.

The first assumption offers the possibility to determine analytically the inertial proprieties of all the

segments of the human body. For these simple objects (symmetric mass distributions, constant density and axes of rotation taken to be through the centre of mass), one can determine the momentum of inertia w.r.t. the symmetry axis through the centre of mass in an exact closed-form expression by using the consistent equation, as in the geometric approximation technique described above.

The second assumption states that the model joints have to be defined on the base of the number of DoFs and the range of motion in degree of the relative biological joints. This information can be found in previous works taken from the literature. The model developed by Xsens system is based on studies found in literature [54], [17], [55] and it is composed of 23 links. We investigate human modelling state-of-the-art too, and we decide to build a model for humans with the same number of links. This choice is justified by the fact that measurement coming from Xsens sensors, fitted for Xsens biomechanical model, have to be associated to our model. Then, as can be seen in Figure 3.12, our model is made up of 23 simple geometric solids, each one representing a segment of the body, linked together by 22 revolute joints. This model has 48 DoFs due to constraints imposed on joints movement which are below described in detail.
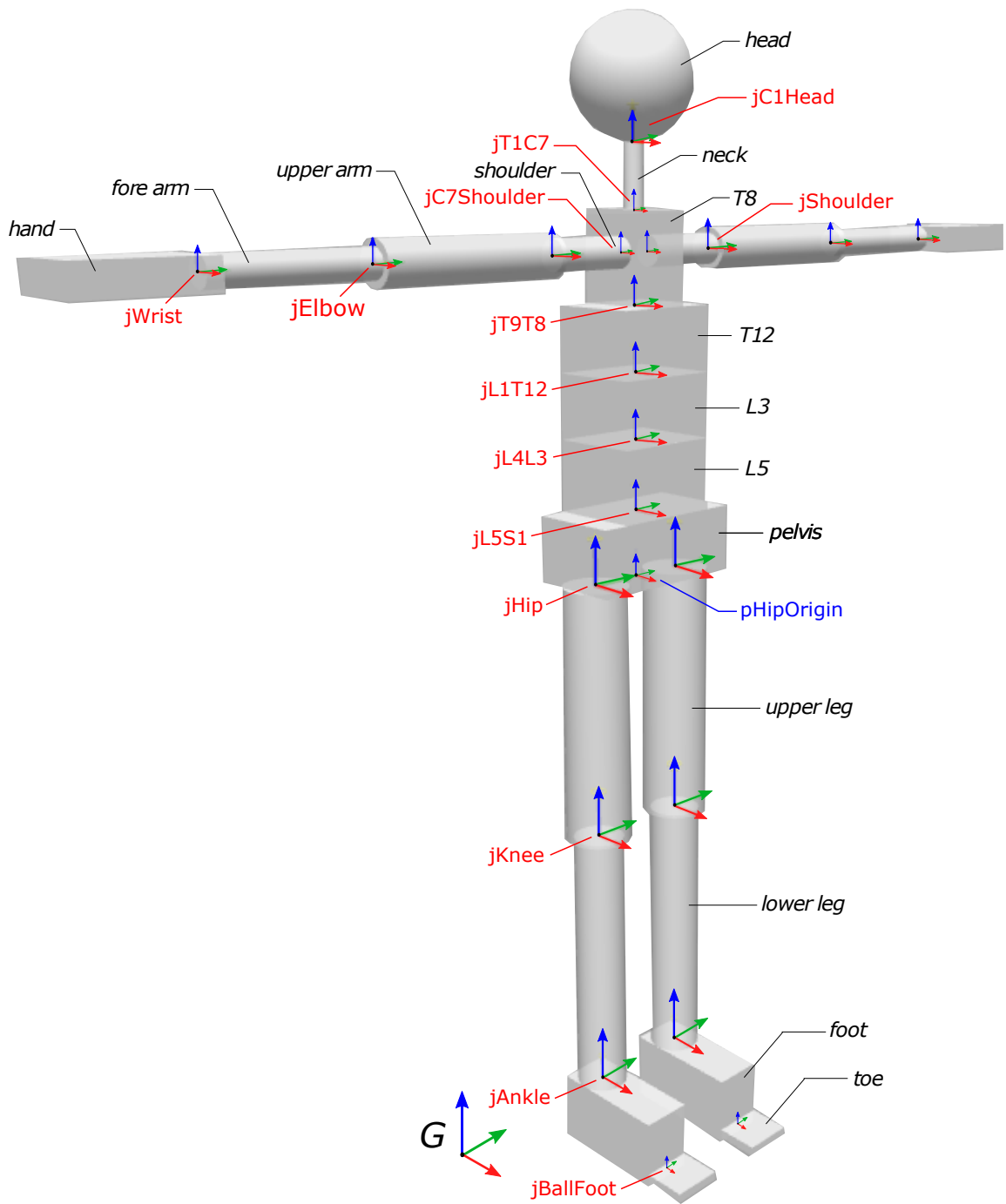
Figure 3.12: Biomechanical model with all segments labels (in black) and all joints labels (in red). The origin of the floating base is the point pHipOrigin (in blue).

Links

As mentioned before, the numbering and labeling of the human model links we are using, is inspired by Xsens system model. The list of links that compose our model is displayed in Table 3.5. The torso is divided in 5 sub-parts: Pelvis, L5, L3, T12 and T8. The labels of these links are related to the vertebra in which each link origin (corresponding with the joint that connects the link to its parent) is located.

For each link, dimensions, geometry, inertial parameters and the origin have to be specified. Each link dimensions are computed using the data extracted from Xsens system. As regards geometry, the links are modeled as cylinders, boxes or spheres. Inertial parameters are computed by exploiting the anthropometric table B.3, starting from the mass m_{tot} of the subject performing an experiment. As concerns moments of inertia, we remind that only the principal moments of inertia are computed, as the inertia tensor is defined as in Equation (3.49). Each link origin is located in the RF of the joint that connects that link with its parent.

For the cylindrical solids (upper and lower legs, upper and lower arms, shoulders, neck and elements of the torso) the radii r_x and r_y, the length h and mass m have to be defined. The lengths h and the radii r_x and r_y, as previously said, are extracted from Xsens data. The mass of each segments, except for the torso, is computed thanks to the anthropometric data and their values are listed in Table 3.5. After computing the total volume of the torso, the volume fraction is calculated for each element and then it is used to derive the relative mass starting from the total mass of the torso, that could be find in the anthropometric tables (torso mass equal to 0.497 m_{tot} and elements masses equal to 0.102 m_{tot}). At this point, the momentum of inertia around the $\boldsymbol{x} - \boldsymbol{y} - \boldsymbol{z}$ axes and through the CoM for all these cylindrical links can be calculated by using following equations:

$$I(xx) = m \ \frac{r_x \ r_y}{2} \tag{3.50}$$

$$I(yy) = m \ \frac{3r_y^2 + h^2}{12} \tag{3.51}$$

$$I(zz) = m \ \frac{3r_x^2 + h^2}{12} \tag{3.52}$$

Feet, toes, hands, T8 and Pelvis are designed by using boxes, of which mass m and dimensions, width (α), height (β) and depth (γ), have to be found. The dimensions are derived from anatomical points of interest, whose coordinates are extracted from the Xsens data and, when it is not feasible, with assumptions. The relative masses that again can be found on the basis of anthropometric tables, as shown in Table 3.5. The momentum of inertia of the boxes can be computed by:

$$I(xx) = m \ \frac{(\alpha^2 + \beta^2)}{12} \tag{3.53}$$

$$I(yy) = m \ \frac{(\beta^2 + \gamma^2)}{12} \tag{3.54}$$

$$I(zz) = m \ \frac{(\gamma^2 + \alpha^2)}{12} \tag{3.55}$$

Finally, the head is represented by a sphere with radius r and mass m. Once the radius is defined

Table 3.5:   List of links and the relative parent joints for human model. For each link the partial mass w.r.t. to the total mass of the subject is defined.

Link	Partial mass	Parent Joint
Pelvis	$0.08\ m_{tot}$	(floating base)
L5	$0.102\ m_{tot}$	jL5S1
L3	$0.102\ m_{tot}$	jL4L3
T12	$0.102\ m_{tot}$	jL1T12
T8	$0.04\ m_{tot}$	jT9T8
Neck	$0.012\ m_{tot}$	jT1C7
Head	$0.036\ m_{tot}$	jC1Head
Right shoulder	$0.031\ m_{tot}$	jRightC7shoulder
Right upper arm	$0.030\ m_{tot}$	jRightShoulder
Right fore arm	$0.020\ m_{tot}$	jRightElbow
Right hand	$0.006\ m_{tot}$	jRightWrist
Left shoulder	$0.031\ m_{tot}$	jLeftC7Shoulder
Left upper arm	$0.030\ m_{tot}$	jLeftShoulder
Left fore arm	$0.020\ m_{tot}$	jLeftElbow
Left hand	$0.006\ m_{tot}$	jLeftWrist
Right upper leg	$0.125\ m_{tot}$	jRightHip
Right lower leg	$0.0365\ m_{tot}$	jRightKnee
Right foot	$0.013\ m_{tot}$	jRightAnkle
Right toe	$0.0015\ m_{tot}$	jRightBallFoot
Left upper leg	$0.125\ m_{tot}$	jLeftHip
Left lower leg	$0.0365\ m_{tot}$	jLeftKnee
Left foot	$0.013\ m_{tot}$	jLeftAnkle
Left toe	$0.0015\ m_{tot}$	jLeftBallFoot

equal to half of the head height (0.130 h_{tot}) and the mass to the value displayed in Table 3.5, the momentum of inertia can be computed as:

$$I(xx) = I(yy) = I(zz) = \frac{2m}{5}(r^2) \tag{3.56}$$

Joints

The links are coupled with 22 joints, whose labels are inspired by the ones of Xsens system and that are listed in Table 3.5. Since each link is connected to its parent by a joint, this specific joint can be considered as the parent joint of that link. The joints need information about: the motion type, the origin defined in terms of the parent RF, the parent and the child links, the friction and the damping coefficients and the joint limit (effort, maximum velocity and range of motion).

For the motion type and the range of motion information, the joints of our model are represented with 1, 2 or 3 DoFs, depending on the anatomy of the relative biological joint. A biological joint, also called an articulation, is defined as the point at which two or more bones articulate. The structure and tissue make up of a joint define its properties including the mobility, strength and stability, and consequently joints could be classified both structurally and functionally. Structural classification takes into account the type of present tissues and so it is possible to distinguish fibrous, cartilaginous and sinovial joints. Functional classification describes the degree of movement available between the bones, related to the functional requirements for that joint. It differentiates synarthrosis or immobile joint, amphiarthrosis or slightly movable joint and diarthrosis, which is a freely movable joint [56]. The joints we are interested in modelling are the diarthrosis because they provide the majority of the body movements. These joints are divided into three categories, based on the number of axes of motion provided by each of them. In anatomy axes are described as the movements in reference to the three anatomical planes: transverse, frontal, and sagittal. Thus, diarthroses are classified as uniaxial (for movement in one plane), biaxial (for movement in two planes), or multi-axial joints (for movement in all three anatomical planes).

The movements that can be carried out by a joint are: flexion and extension, abduction and adduction, lateral bending, elevation and depression, pronation and supination, medial and lateral rotation, dorsiflexion and plantarflexion, opposition and reposition [57]. Flexion and extension are movements that occur in the sagittal plane. They refer to decreasing and increasing, respectively, the angle between two body parts. Abduction and adduction are used to describe movements away from or towards the mid line of the body. Lateral bending, referred to vertebrae, is the movement around the anterior-posterior axis in the frontal plane. Elevation refers to movement in a superior direction while depression refers to movement in an inferior direction. Pronation refers to the inward roll while supination is the opposite motion. Medial and lateral rotations describe movement of the limbs around their long axes. Dorsiflexion and plantarflexion are terms used to describe movements at the ankle. They refer to the two surfaces of the foot the dorsum (superior surface) and the plantar surface (the sole). Opposition brings the thumb and little finger together while reposition is the movement that

moves the thumb and the little finger away from each other.

In order to measure the joints movements we have to define the neutral orero position. Most of these positions coincide with the anatomical standing pose of the subject [58]. Moreover, for all the DoFs of the joints included in the model, we have to define their range of motion, the measurement of movement in one plane around a specific joint or body part. Based on previous studies in the literature, we define the human model joints DoFs and average ranges of motion, as shown in Table 3.6. The definition of these properties can be arbitrary or based on studies taken from literature.

As a consequence of these constraints, a 48 DoFs model is defined. This model allows to analysed complex physiological movements since all the biological DoFs are considered. The joint origins are located in the origins of the biological joint RF. This RF is defined with $x - y - z$ axes directions coincident with functional axes' ones, as to permit functional movements. The origins of these RFs are defined arbitrarily in the following way:

⬦ *jL5S1*: at the top of the pelvis, in the middle of the base of the box;

⬦ *jL4L3*: at the top of L5, in the middle of the circular base of the cylinder;

⬦ *jL1T12*: at the top of L3, in the middle of the circular base of the cylinder;

⬦ *jT9T8*: at the top of T12, in the middle of the circular base of the cylinder;

⬦ *jT1C7*: at the top of T8, in the middle of the base of the box;

⬦ *jC1Head*: at the top of the neck, in the middle of the circular base of the cylinder;

⬦ *jC7Shoulder*: on the lateral border of T8, at the middle of T8 height and depth;

⬦ *jShoulder*: on the lateral border of the shoulder link, in the middle of the circular base of the cylinder;

⬦ *jElbow*: at the bottom of the upper arm, in the middle of the circular base of the cylinder;

⬦ *jWrist*: at the bottom of the fore arm, in the middle of the circular base of the cylinder;

⬦ *jHip*: at the bottom of the pelvis, translated along the y axes both on the right and on the left for each side (derived from the Xsens system data);

⬦ *jKnee*: at the bottom of the upper leg, in the middle of the circular base of the cylinder;

⬦ *jAnkle*: at the bottom of the lower leg, in the middle of the circular base of the cylinder;

⬦ *jBallFoot*: at the extremity of the foot length, in the middle of the base of the box.

In Figure 3.12 the parent and the child link of each joint and the order they are connected with, can be visualized.

The friction and the damping coefficients are employed especially for simulation. The physical damping and the physical static friction values of the joint are respectively 0.1 Nms/rad and 0.0 Nm. For each joint some limits have to be defined:

Table 3.6: List of joints with the relative DoFs, allowed movements and ranges of motions. The definition of these properties can be arbitrary or based on studies taken from literature.

Joints	DoFs	Allowed movements	Range of motion	Definition
jBallFoot	1	*flexion and extension*	90°- 0°- 10°	Arbitrarily
jAnkle	3	*dorsiflexion and plantarflexion*	50°- 0°- 30°	From literature[58]
		abduction and adduction	45°- 0°- 35°	
		supination and pronation	50°- 0°- 25°	
jKnee	2	*flexion and extension*	135°- 0°- 0°	From literature[58]
		medial and lateral rotation	30°- 0°- 40°	
		(with 90° knee flexion)		
jHip	3	*flexion and extension*	120°- 0°- 15°	From literature[58]
		abduction and adduction	45°- 0°- 30°	
		medial and lateral rotation	45°- 0°- 45°	
jL5S1	2	*flexion and extension*	75°- 0°- 30°	From literature[59]
		lateral bending	35°- 0°- 35°	
jL4L3	2	*flexion and extension*	75°- 0°- 30°	From literature[59]
		lateral bending	35°- 0°- 35°	
jL1T12	2	*flexion and extension*	75°- 0°- 30°	From literature[59]
		lateral bending	35°- 0°- 35°	
jT9T8	3	*flexion and extension*	40°- 0°- 15°	From literature[60]
		lateral bending	20°- 0°- 20°	
		medial and lateral rotation	35°- 0°- 35°	
jT1C7	3	*flexion and extension*	90°- 0°- 55°	From literature[60]
		lateral bending	35°- 0°- 35°	
		medial and lateral rotation	70°- 0°- 70°	
jC1Head	2	*flexion and extension*	10°- 0°- 25°	From literature[60]
		lateral bending	35°- 0°- 35°	
jC7Shoulder	1	*elevation and depression*	45°- 0°- 5°	Arbitrarily
jShoulder	3	*flexion and extension*	180°- 0°- 45°	From literature[61]
		abduction and adduction	180°- 0°- 45°	
		medial and lateral rotation	90°- 0°- 90°	
jElbow	2	*flexion and extension*	145°- 0°- 0°	From literature[61]
		supination and pronation	90°- 0°- 85°	
jWrist	2	*flexion and extension*	60°- 0°- 50°	From literature[58]
		abduction and adduction	30°- 0°- 20°	

◇ the lower joint limit: the lower bound of the range of motion of the joint, in rad;

◇ the upper joint limit: the upper bound of the range of motion of the joint, in rad;

◇ the maximum effort: a threshold for the effort that can be applied on the joint, in Nm;

◇ the maximum velocity: the bounds on the magnitude of the joint velocity, in rad/s.

The quantities defined above are assigned to the joint limits while the value of the last two fields are respectively set to 30 Nm and 1.0 rad/s for all joints.

Kinematic tree

Once the links and the joints are defined, we have to create a description of the kinematic structure that describes the hierarchical architecture of the model.

We set the pelvis as the floating base, so that the following element of the torso (L5), the right and the left leg are its child links. The elements of the torso are connected in a chain until the last elements of the torso (T8), which is connected with the two shoulders and the neck. The arms are composed of the upper arm, the fore arm and the hand and are attached to the shoulders on both the right and the left side. The two legs are composed of the upper leg, the lower leg, the foot and the toes and are attached at the bottom of the pelvis. The head is attached at the top of the neck.

We suppose the position and orientation, and other kinematic data of each link to be expressed w.r.t. an earth-fixed reference coordinate system, defined as a right handed Cartesian coordinate system with:

◇ **Global RF:**

◇ X positive when pointing to the local magnetic North;

◇ Y according to right handed coordinates (West);

◇ Z positive when pointing up.

◇ **Local coordinate frame:** (considering links in anatomical pose):

◇ *Origin*: center of rotation (proximal);

◇ X forward;

◇ Y pointing right;

◇ Z up, from joint to joint.

This means that each links' RF is coupled with the joint that connect it to its parent and it moves as the consistent link.

All this information has to be included in two different files, used as a prototype for the analysis: a URDF (Unified Robot Description Format) file, that can be imported in Matlab and an osim file. The URDF is a XML specification in which the links and the joints that represent the model, along

with the related properties and limits, are listed. It is used as an input for the MAP algorithm to solve the dynamic estimation.

In order to verify the model represented through the URDF, we can get insight into it thanks to Gazebo, a simulation software which offers the possibility to accurately and efficiently display and simulate populations of robot, virtual environment and any other type of model. It is possible to see how our model appears in Gazebo: in Figure 3.13 the global RF and the link RF are displayed.

The osim file is a text file defined in a similar way to the URDF one; it is needed in order to perform the IK and the ID computation with the software OpenSim.
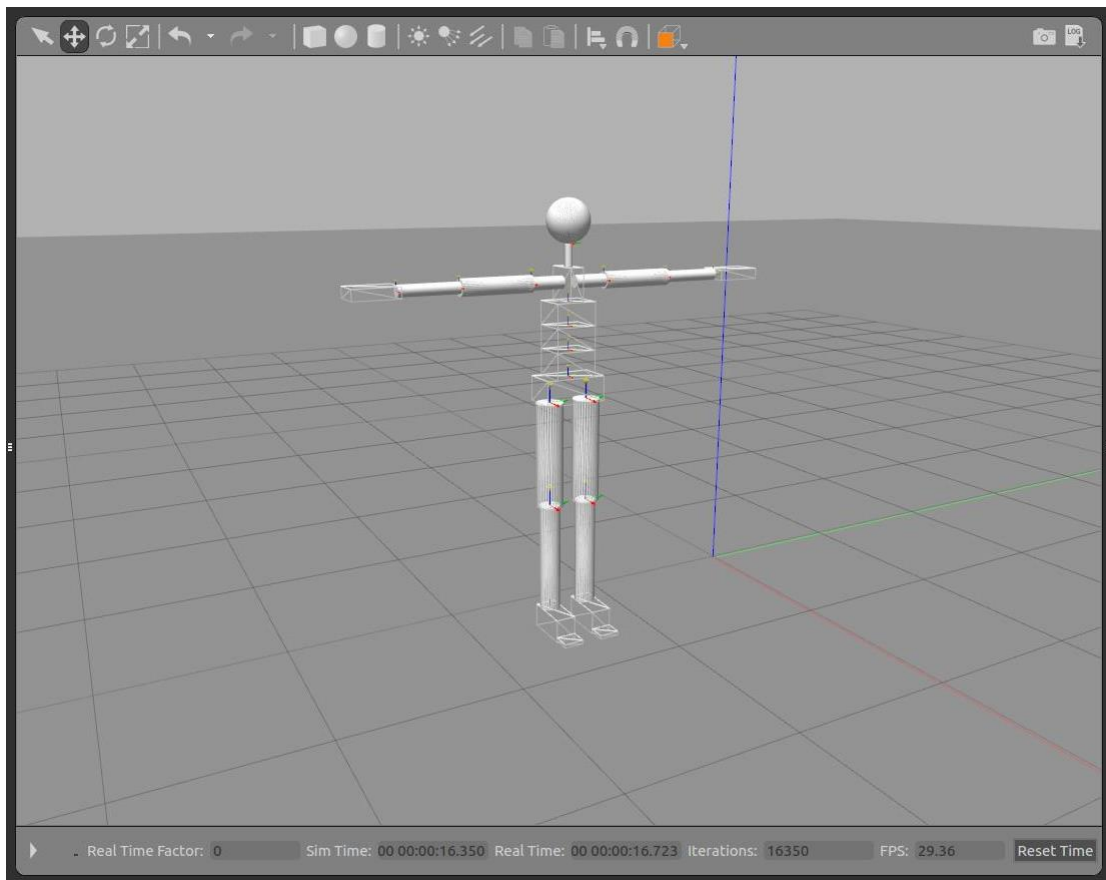
Figure 3.13: Biomechanical model of human as it appears in Gazebo simulator environment.

Markers

In order to perform the IK computation with OpenSim IK tool, we need as input the osim model and data about the trajectories of some points of interest, associated to the model itself. Then joint angles can be computed. To this end, we use the trajectories of the 64 anatomical landmarks (provided by Xsens system), that have to be associated to the correspondent markers in the osim model. Indeed, the osim model is defined with a marker set in accordance with the Xsens anatomical landmark set.

The position of each marker in the combined link RF can be extracted among Xsens data and

then defined in the osim model in the same link RF. The anatomical landmarks defined in the Xsens model and the relative markers which we associate to the osim model are displyed in Figure 3.14. For simplicity, the name of anatomical landmarks and osim markers are the same.

Figure 3.14: In (a) the positions of anatomical landmarks associated to Xsens model are shown. In (b) the positions of markers defined in OpenSim model, in accordance with Xsens anatomical landmarks, are shown. The trajectories of these markers are employed in IK computation.

Sensors

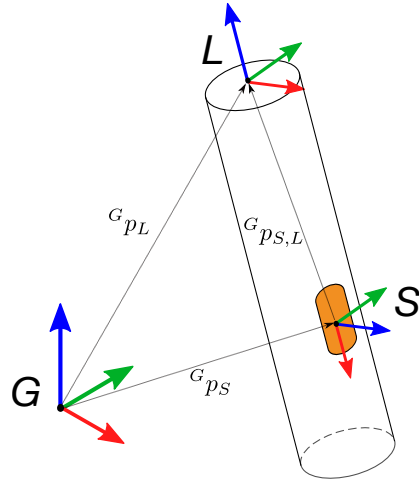In order to perform ID computation with MAP algorithm, the information about the Xsens IMUs has to be included in the URDF model. For using the data coming from the suit, the link at which each sensor is attached and its position in the link have to be specified. The position of the sensor w.r.t. the attached link, that is not provided by Xsens system, is obtained by exploiting the linear acceleration $\boldsymbol{a}$ and the angular velocity $\boldsymbol{\omega}$ measured by sensors in the following way:

$$
\begin{aligned}
{}^{S}\boldsymbol{a}_{S} &= {}^{S}\boldsymbol{R}_{G}\ ({}^{G}\boldsymbol{a}_{S} - {}^{G}\boldsymbol{a}_{g}) \\
&= {}^{S}\boldsymbol{R}_{G}\ [{}^{G}\boldsymbol{a}_{L} + {}^{G}\dot{\boldsymbol{\omega}}_{L} \times {}^{G}\boldsymbol{R}_{L}{}^{L}\boldsymbol{p}_{S,L} + {}^{G}\boldsymbol{\omega}_{L} \times ({}^{G}\boldsymbol{\omega}_{L} \times {}^{G}\boldsymbol{R}_{L}{}^{L}\boldsymbol{p}_{S,L}) - {}^{G}\boldsymbol{a}_{g}]
\end{aligned}
\tag{3.57}
$$

where S is the frame of the sensor and L is the frame related to the link on which it is attached, as showed in Figure 3.15 .

Figure 3.15: Sensor attached to a generic link.

This equation yields to the position of sensor on the link:

$$^L\boldsymbol{p}_{S,L} = \boldsymbol{A}^{-1}(^G\boldsymbol{a}_{L,S} + {}^G\boldsymbol{a}_g) \tag{3.58}$$

where

$$\boldsymbol{A}^{-1} = \left[\boldsymbol{\mathcal{S}}(^G\dot{\boldsymbol{\omega}}_L) + \boldsymbol{\mathcal{S}}^2(^G\boldsymbol{\omega}_L) \right] {}^G\boldsymbol{R}_L \tag{3.59}$$

PART III

EXPERIMENTAL ANALYSIS AND RESULTS

Chapter 4

Experimental Analysis

In order to test the proposed framework an experimental investigation is conducted. We delineate a protocol consisting in five different tasks (two performed only by the human, three involving pHRI) which have to be repeated five times. Ten healthy and adult subjects are recruited. The positions of the human wearing the suit, iCub and force plates are set and kept fixed during all the experiments. In order to handle the communication between all the devices included in the experimental set-up, the appropriate connections and synchronization procedures are implemented and the post-processing of raw data is outlined. Four different type of analysis with relative objectives, analysed quantities and evaluation metrics are defined in detail.

In this chapter we firstly describe the experimental protocol and the set-up. Then, we present the dataset obtained and the relative post-processing phase which we have configured. Subsequently, provided the detailed characterization of the four analysis conducted, we expose their outcomes. A section that discuss the obtained results, concludes the chapter.

4.1 Experiments

Experiments for testing the proposed framework for ID estimation were conducted on ten adult and healthy subjects. Subjects were provided a written informative consent before starting the experiment. The height and the mass (included the Xsens system mass) of each subject recruited and the relative mean μ and standard deviation σ of all heights and all masses are showed in Table 4.1. No requirement as regards nationality was needed, so subjects have been chosen between Italian and foreigners, without specification. Data were collected at Istituto Italiano di Tecnologia (IIT), Genoa, Italy.

Table 4.1: List of each subject height and mass and relative mean μ and standard deviation σ

| Subject	Height [cm]	Mass [kg]
1	165	60.8088
2	166	67.2970
3	161	54.4269
4	172	64.0725
5	171	58.7148
6	169	65.3451
7	170	68.2332
8	165	52.7832
9	169	65.3586
10	158	54.3953
μ	166.6	61.1435
σ	4.5018	5.7608

4.1.1 Protocol

The subjects are asked to wear the suit and stand on the two force plates positioning one foot for each platform in a known position, with the assumption of rigid contact with the ground. iCub is located in front of the subject, facing him at a known distance. The position of one iCub foot is fixed and iCub maintains the same configuration during all the experiments. This layout of human and robot feet positioning, whose schema and photo are showed in Figure 4.1, is located on the ground in a known position w.r.t. the force plates on which the experiments are performed.

The information about the relative position between the human, iCub and the force plates is necessary in order to provide:

⋄ the transformation matrix $^{hand}\boldsymbol{X}_{iCubFT}$ between the human hand and the F/T sensor position on iCub arms;

⋄ the transformation matrix $^{foot}\boldsymbol{X}_{fp}$ between each human foot and the relative force platforms.

These matrices, displayed in Figure 4.2, are adopted in order to express data coming from each sensor in the RF of the human subject link in contact with that specific sensor.
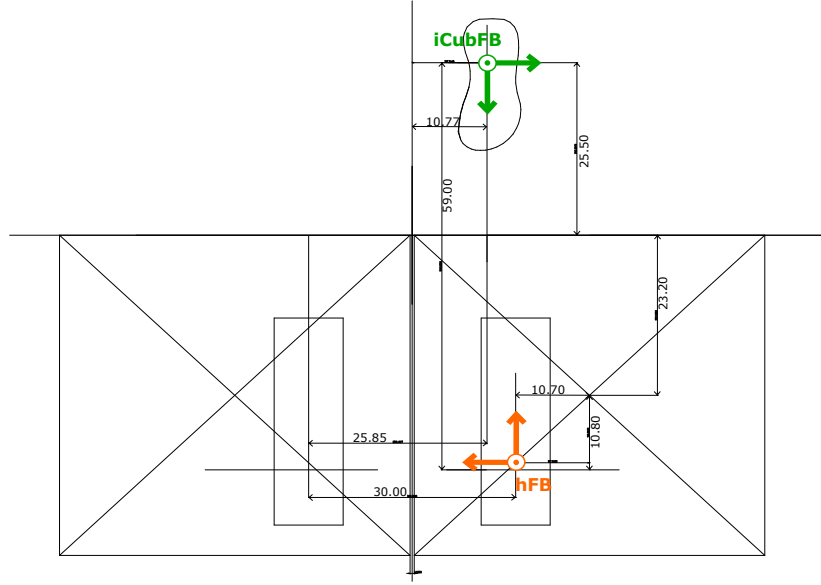
(a)
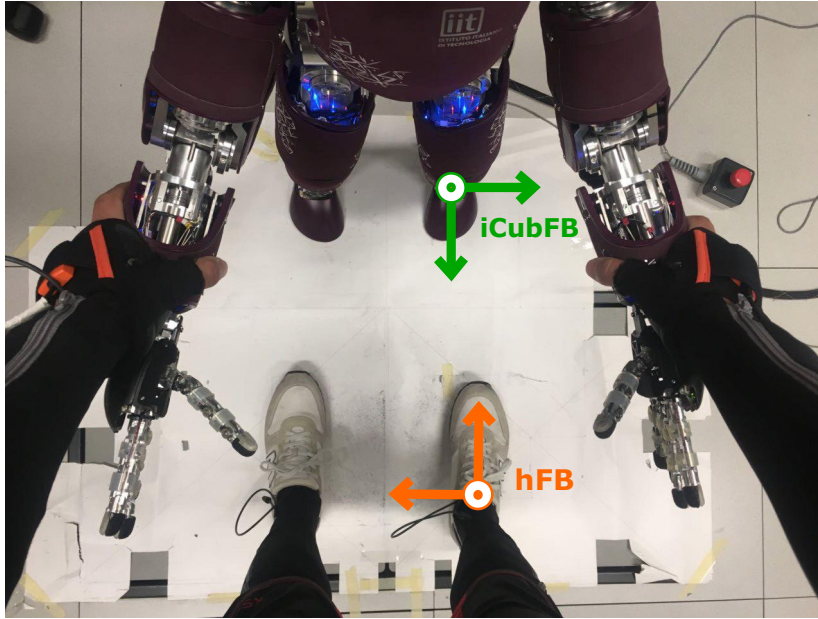
(b)

Figure 4.1: Geometric layout for human and robot fixed feet positioning: schema (a) and photo (b). The RFs of human fixed-base (hFB) and of iCub fixed-base (iCubFB) are represented.

Going into detail, in order to obtain ${}^{hand}\boldsymbol{X}_{iCubFT}$ and ${}^{foot}\boldsymbol{X}_{fp}$, the multiplication of transformation matrices is required:

$$
{}^{hand}\boldsymbol{X}_{iCubFT} = {}^{hand}\boldsymbol{X}_{hFB} \; {}^{hFB}\boldsymbol{X}_{iCubFB} \; {}^{iCubFB}\boldsymbol{X}_{iCubFT} \tag{4.1}
$$

$$
{}^{foot}\boldsymbol{X}_{fp} = {}^{foot}\boldsymbol{X}_{hFB} \; {}^{hFB}\boldsymbol{X}_{\bar{fp}} \; {}^{\bar{fp}}\boldsymbol{X}_{fp} \tag{4.2}
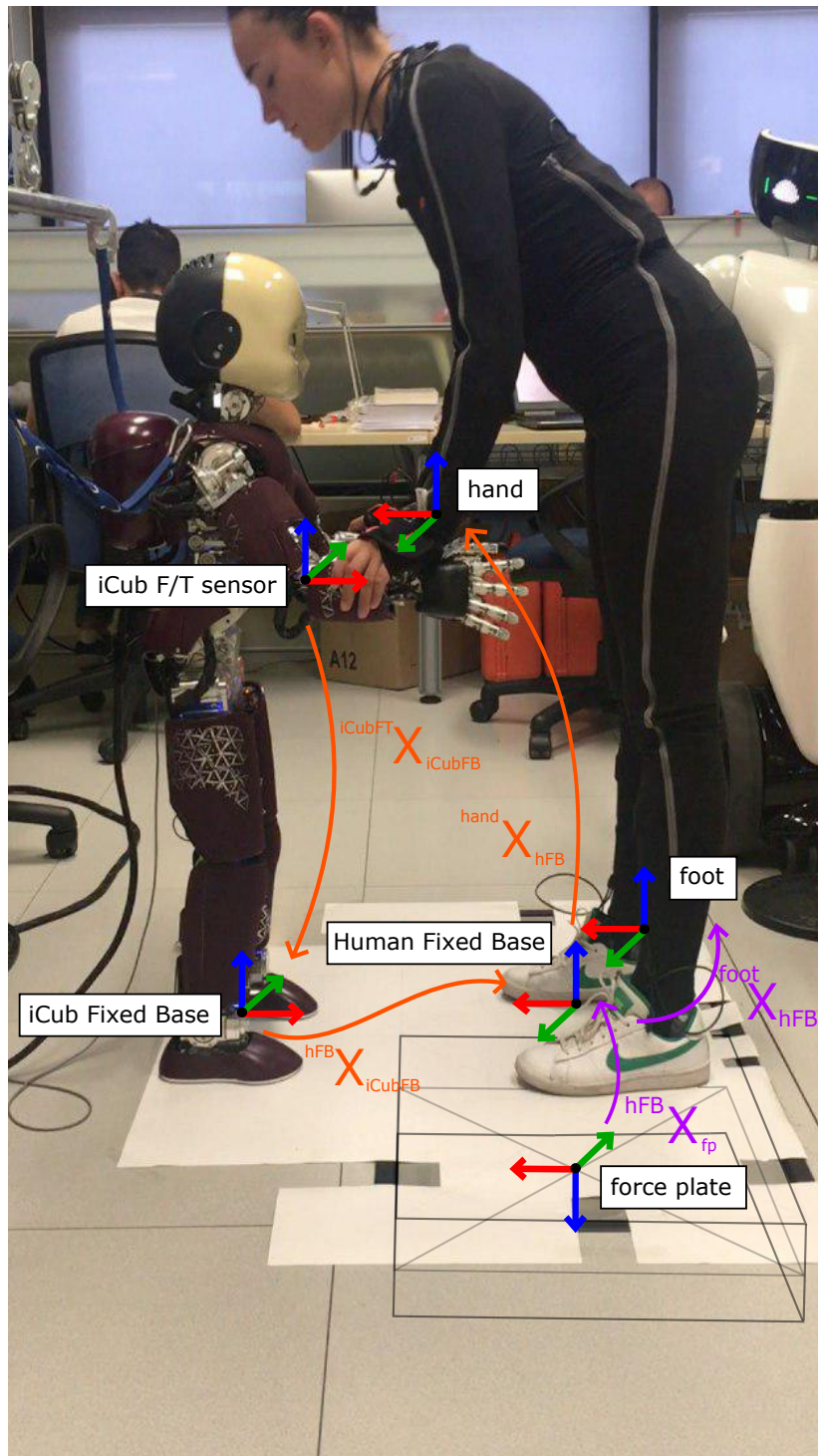$$

Figure 4.2: Human, force plates and iCub RFs with the relative transformation matrices. These transformation matrices are needed in order to express sensor measurements in the human links RFs, which they are in contact with.

where, with hFB we refer at the human fixed base, with $iCubFB$ we refer at iCub fixed base and with $\bar{fp}$ we mean the theoretical RF of the force plates (located in the centroid of the platform) that have to be calibrated with $^{\bar{fp}}\boldsymbol{X}_{fp}$ (force plates data-sheets). This configuration and, as a consequence, the transformation matrices are kept constant during all the experiments.

The subject is asked to perform four different tasks for five times, involving or not a physical interaction with iCub. These tasks are described below, as they have been explained to the subjects before performing the experiment:

1. **bowing task without pHRI (BH)**: the subject is asked to bow without bending the knees keeping both arms straight and in line with the vertical axis of the torso with palms turned inwards and back in a neutral position;

2. **bowing task with pHRI (BR)**: the subject is asked to bow without bending the knees while grasping and pushing down both iCub arms (as shown in Figure 4.3) with back in neutral position;

3. **squat without pHRI (SH)**: the subject is asked to lower the hips as if to sit while bending the knees keeping both arms straight and in line with the vertical axis of the torso with palms turned inwards and back in a neutral position;

4. **squat with pHRI (SR)**: the subject is asked to lower the hips as if to sit while bending the knees, grasping and pushing down both iCub arms (as shown in Figure 4.4) with back in neutral position;

During all these trials, subjects are asked not to move their feet from the template on the ground because of the rigid contact assumption. All the movements have to be performed keeping the heels in contact with the ground, even if this imposition may lead to unnatural behaviour. As regard the back position, subjects in all the trials must try not to bend the spinal cord throughout the movement. In pHRI trials (BR and SR), subjects are asked to grasp iCub arms with their thumbs turned inwards, as showed in Figures 4.3 and 4.4. No particular specification as regard the force to be exerted on iCub arms has been given to subjects.

This list of the described tasks composes a block and all subjects have to perform five repetitions of this block. In each block the order of execution of the different tasks is randomized, in order to make each trial independent from the trial of the previous block.

In addition to this protocol employed for torque estimation analysis, in order to perform a robustness test for MAP algorithm, a different experiment is conducted.

5 **bowing task with pHRI with an additional weigh (BRW)**: the same subject with and without an additional weigh of a known value, located approximately on the CoM of the torso, is asked to perform five repetition of the bowing task with pHRI. The subject have to follow the same procedure adopted for the previous experiment.
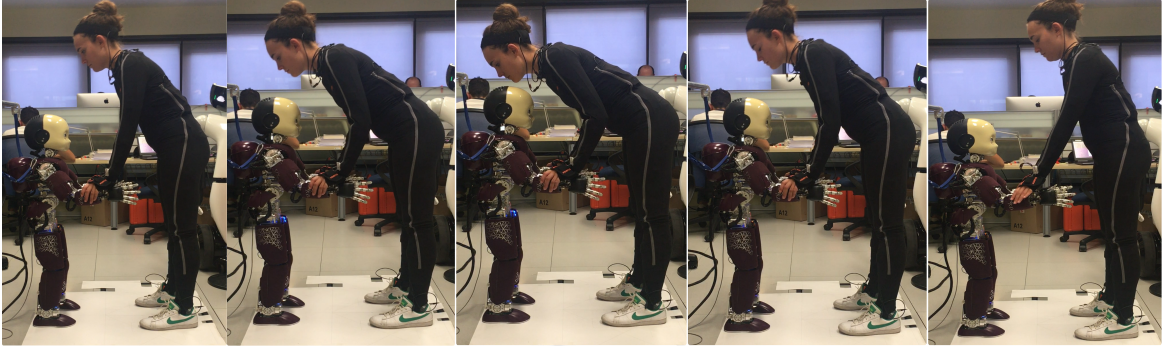
Figure 4.3: Subject performing a bowing task with pHRI (BR). These frame are extracted from a video with sampling rate of 1.5 Hz.
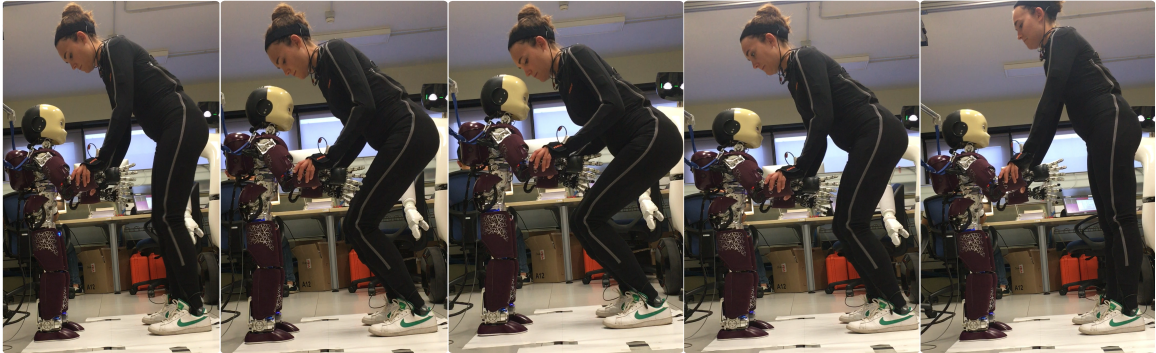

Figure 4.4: Subject performing a squat with pHRI (SR). These frame are extracted from a video with sampling rate of 1.5 Hz.

4.1.2 Experimental set-up

The framework outlined to conduct the experiments include different devices for which a communication have to be implemented. The connection between the Xsens suit and the PC where the MVN software is installed on is performed through an Access Point. The data from the suit are sent via wireless to the Access Point, that is connected to the PC with an Ethernet cable. The force plates are controlled by the same PC through an hardware synchronization system: the Awinda station. The Awinda Station is a device provided by Xsens created specifically for biomechanics applications in order to provide a synchronization with third party devices. It is connected to the PC through an USB cable and to the force plates through two BNC connectors. Finally, a second PC controls iCub. In order to match the clock of the two PCs, the first PC system time is synchronized to the NTP [1] server of the second one. The described configuration set-up is shown in Figure 4.5. Data collected from the three measurement sources are listed below:

⋄ angular velocities $\boldsymbol{\omega}_i$ and linear accelerations $\boldsymbol{a}_i$ of each link ($i = 1, \ldots, 23$) are collected from Xsens system;

---

[1] Network Time Protocol (NTP) is a networking protocol for clock synchronization between computer systems over packet-switched, variable-latency data networks.

61

◇ anatomical landmarks (i.e. virtual markers) trajectories $\boldsymbol{p}_{marker}$ are collected from Xsens system (and then give as input to OpenSim IK tool);

◇ time data associated to each frame expressed in unix time stamp[2] format are collected from Xsens system;

◇ external wrenches (forces and momentum) $\boldsymbol{f}_{GRFs}^{x}$ exchanged between human feet and the ground are collected from the two force plates;

◇ external wrenches (forces and momentum) $\boldsymbol{f}_{iCub}^{x}$ exchanged between human hands and robot arms are collected from the robot itself;

◇ time data associated to each frame expressed in unix time stamp format are collected from the robot.

Xsens generates a (`.mvnx`) file (Xsens Open XML format) containing 3-D position ($\boldsymbol{x} - \boldsymbol{y} - \boldsymbol{z}$ coordinates), linear and angular acceleration and velocity of all 23 segments, 3-D joint angles of all 22 joints, 3-D orientation, acceleration, angular velocity and magnetic field data of all 17 IMUs. The force plates generate a file (`.txt`) containing data about wrenches measured by both platforms for each time frame. Finally, iCub generates seven files (`.txt`): five containing information about the iCub state (two arms, two legs and torso pose w.r.t. the pose detected during the robot calibration - iCub home position) and two containing wrenches measured by the F/T sensors located on the iCub arms, along with time data for each frame. After being collected in the same folder, these data are ready to be processed.

---

[2]Unix time is a system for describing istants in time, defined as the number of seconds that have elapsed since 00:00:00 Coordinated Universal Time (UTC), Thursday 1 January 1970
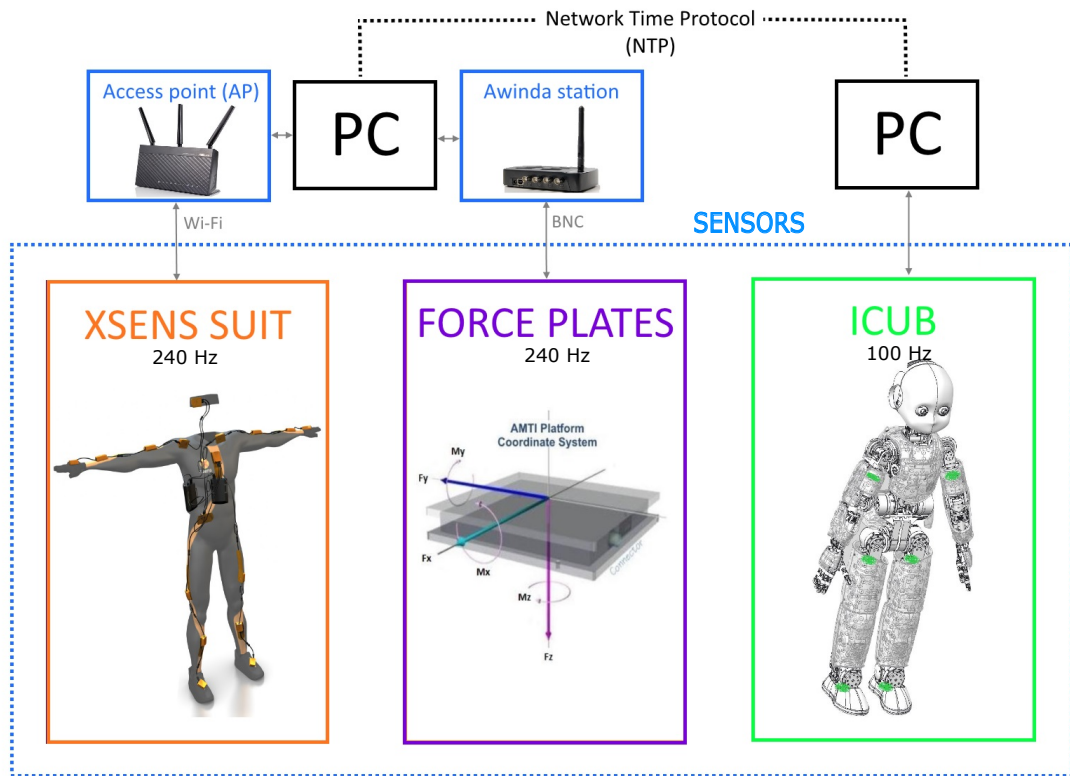
Figure 4.5: Scheme of the experimental set-up. The Xsens suit and the force plates are controlled by the same PC and acquired data at 240 Hz. A second PC controls iCub, that collect sample at 100 Hz. The synchronization between the two PCs is provided through NTP server.

The three sensing system have different acquisition sampling rate: i) the Xsens system collects data at 240 Hz, ii) the force plates present a maximum sampling rate of 1000 Hz but they can be configured to acquire data at a different frequency and iii) iCub data are collected at 100 Hz. In order to perform all the computation for the MAP estimation, all the data coming from these sources must be sampled at the same frequency. To this aim, Awinda station is employed. The Awinda hardware clock is very accurate. As an indication of the clock accuracy, the error has a maximum of 1 μs every second [41]. Thanks to the Awinda Station it is possible to synchronize the force plates and the XSens system: once the acquisition is started (thanks to a manual trigger of the operator), every time the Xsens system collects a sample, it sends a rectangular pulse that, through the station, reaches the platform. Each platform receives the pulse and in turn it collects the relative sample with the data about wrenches in that specific time frame. Within this configuration, the force platforms are forced to acquired data at a sampling rate of 240 Hz.

As regards the synchronization with iCub instead, we exploit the unix time stamps series associated to data originating from both the suit and iCub. A unix time stamp is associated to each temporal frame. Firstly, the initial and final instant of the two dataset must have a temporal correspondence and so unix time stamps must match. For that purpose, an eventual cutting of the data must be

performed. Secondly, since robot data are collected at a frequency of 100 Hz (lower than the suit one), time data of the suit are employed to fill robot data thanks to a linear interpolation function.

Both data coming from force plates and iCub express the wrenches applied on them in their RFs (origin and orientation), which are represented in Figure 4.2. For human dynamic variables estimation, we need to get these wrenches but: they have to be multiplied by -1 (as the wrench applied on the human is exactly the opposite of the one exerted on the force plates or on the robot, due to their RFs definition) and they have to be expressed in the frame of the human link in contact with the sensor (RFs represented in Figure 4.2). On account of this, with regard to the force plates, the transformation matrix between RFs of the platforms and RFs of human feet $^{foot}\boldsymbol{X}_{fp}$ (defined in Equation (4.2)) is computed and then applied to the relative wrenches. Similarly, as regards iCub, the transformation matrix between RFs of robot arms (where F/T sensors are localized) and RFs of human hands $^{hand}\boldsymbol{X}_{iCub}$ (defined in Equation (4.1)) is computed.
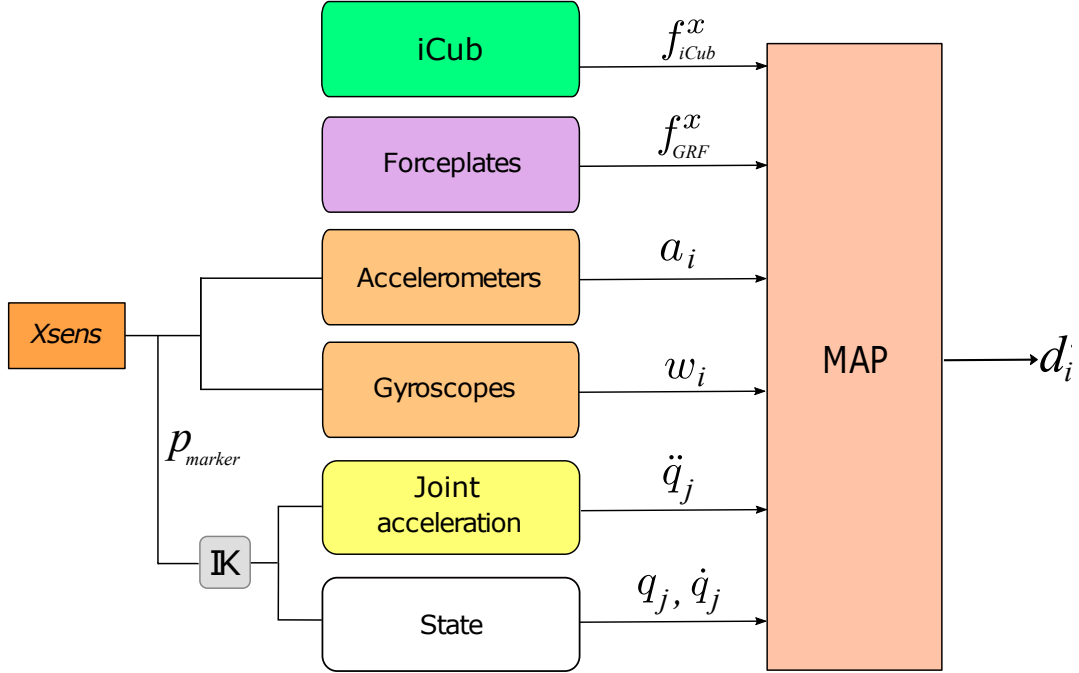

Figure 4.6: Scheme of the inputs and output of the estimation MAP framework. Inputs are: sensor measurements (iCub $\boldsymbol{f}^x_{iCub}$ force plates $\boldsymbol{f}^x_{GRFs}$ and suit $\boldsymbol{a}_i$, $\boldsymbol{\omega}_i$), joint acceleration $\ddot{\boldsymbol{q}}_j$ and state $\dot{\boldsymbol{q}}_j$, $\boldsymbol{q}_j$ (from OpenSim IK tool) and the biomechanical model. The output of MAP is the dynamic variables vector $\boldsymbol{d}_i$

An overview of the framework is summarised in Figure 4.6. Data coming from force plates $\boldsymbol{f}^x_{GRFs}$ and from the robot $\boldsymbol{f}^x_{iCub}$ are considered as net external wrenches. Linear acceleration $\boldsymbol{a}_i$ and angular velocity $\boldsymbol{\omega}_i$ for each i-th link are acquired by Xsens IMUs. Xsens data about trajectories of anatomical landmarks, which are points of interest located on the human subject, are used as input for the

Opensim [34] IK tool. The .osim model, provided in order to employ OpenSim, is endowed with markers in the same position of these anatomical landmarks. By exploiting their trajectories $\boldsymbol{p}_{marker}$, the IK tool computes the joint angles $\boldsymbol{q}_j$ for each joint ($j = 1, \ldots, 22$), which from now on are considered as the human state along with joint velocities. Joint velocities $\dot{\boldsymbol{q}}_j$ and accelerations $\ddot{\boldsymbol{q}}_j$ are computed thanks to a third-order polynomial Savitzky-Golay filtering[3](consisting in a weighed sum of windows of 57 elements). Joint accelerations $\ddot{\boldsymbol{q}}_j$ are considered as acquired from a class of accelerometers located on the joint centres. In general, by considering as inputs data acquired from all above-mentioned sensors and the state $(\boldsymbol{q}_j, \dot{\boldsymbol{q}}_j)$, the MAP estimator provides the estimation of $\boldsymbol{d}_i$ given $\boldsymbol{y}_{meas}$. The vector $\boldsymbol{d}_i$ contains the sequence of dynamic variables listed in Equation (4.3) computed for each temporal frame through the experiment and for all the j-th joints and the i-th links of the human subject.

$$\boldsymbol{d}_i = \left[\begin{array}{cccccc} \boldsymbol{a}_i^T & \boldsymbol{f}_i^{B^T} & \boldsymbol{f}_i^T & \boldsymbol{\tau}_j^T & \boldsymbol{f}_i^{xT} & \ddot{\boldsymbol{q}}_j^T \end{array} \right] \tag{4.3}$$

where $\boldsymbol{a}_i$ is the link spatial accelerations, $\ddot{q}_j$ is the joint j acceleration, $\boldsymbol{\tau}_j$ is the joint j torque, $\boldsymbol{f}_i$ is the spatial force transmitted to body i from its parent link, $\boldsymbol{f}_i^B$ is the net spatial force on body i and $\boldsymbol{f}_i^x$ are external forces acting on body i. Indeed MAP algorithm estimates not only joints torques, as classic ID method, but a number of dynamic variables. Since MAP algorithm could associate a different variance to the sensors according to their reliability, for each type of sensor employed a reasonable variance have to be assigned. We remind that for each sensor a covariance matrix is actually defined; we set all the values of this matrix to zero, except for the values on the diagonal, since they represents the variances. The value of variances used for all our experiments are displayed in Table 4.2. The computation of these variances is explain in detail in Appendix C, thanks to PhD Silvio Traversaro. A variance could be associated even to the model according to its capability of modelling the human being. We use a variance equal to 10^{-4} for all the performed experiments, except for the robustness test of MAP algorithm w.r.t. modelling errors. In this latter analysis, the task BRW is analysed, assigning a different value of variance to the model (equal to 10^{-1}). The estimation of these dynamic variables is expressed through the mean $\boldsymbol{\mu}_{d|y}$ (3.39b) and the standard deviation $\boldsymbol{\Sigma}_{d|y}$ (3.40).

Among all of them, the quantities of major interest in our analysis are the torques $\boldsymbol{\tau}$. We consider the joints mainly involved during the analysed task and we evaluate the torque along the axis in which the most significant angle variation is observed. In particular, for the bowing task we take into account the torque at the hip and at the ankle along the $\boldsymbol{y}$ axis, while for the squat we take into account the torque at the knee and at the hip along the same axis. The $\boldsymbol{y}$ axis, that is enhanced in the RFs of the analysed torques in Figure 4.7, is the axis along with flexion and extension occur (the main movements that are carried out during all the tasks analysed). The torques considered represent

---

[3]The Savitzky-Golay FIR smoothing filters are generalizations of the FIR averager filter. Solving analytically the associated least-square equations, they provide a set of coefficients which can be employed to obtain the estimation of the smoothed signal or its first and second derivative [62].

Table 4.2: Values of variance associated to each sensor and to the model.

Sensor	Variance
IMUs	$1.11 \ 10^{-3}$
Joint accelerations	$6.66 \ 10^{-6}$
Force plates	$[59; \ 59; \ 36; \ 2.25; \ 2.25; \ 0.56] \ 10^{-3}$
iCub	$[59; \ 59; \ 36; \ 2.25; \ 2.25; \ 0.56] \ 10^{-3}$
Model	10^{-4}

the most meaningful internal moments developed during the selected tasks. Since the estimation of the torques provides the same results for the two sides of the human body, it can be exhaustive to show only the torques associated to one side, i.e. the right. In order to compare these torques, several operation have to be performed on the raw data.
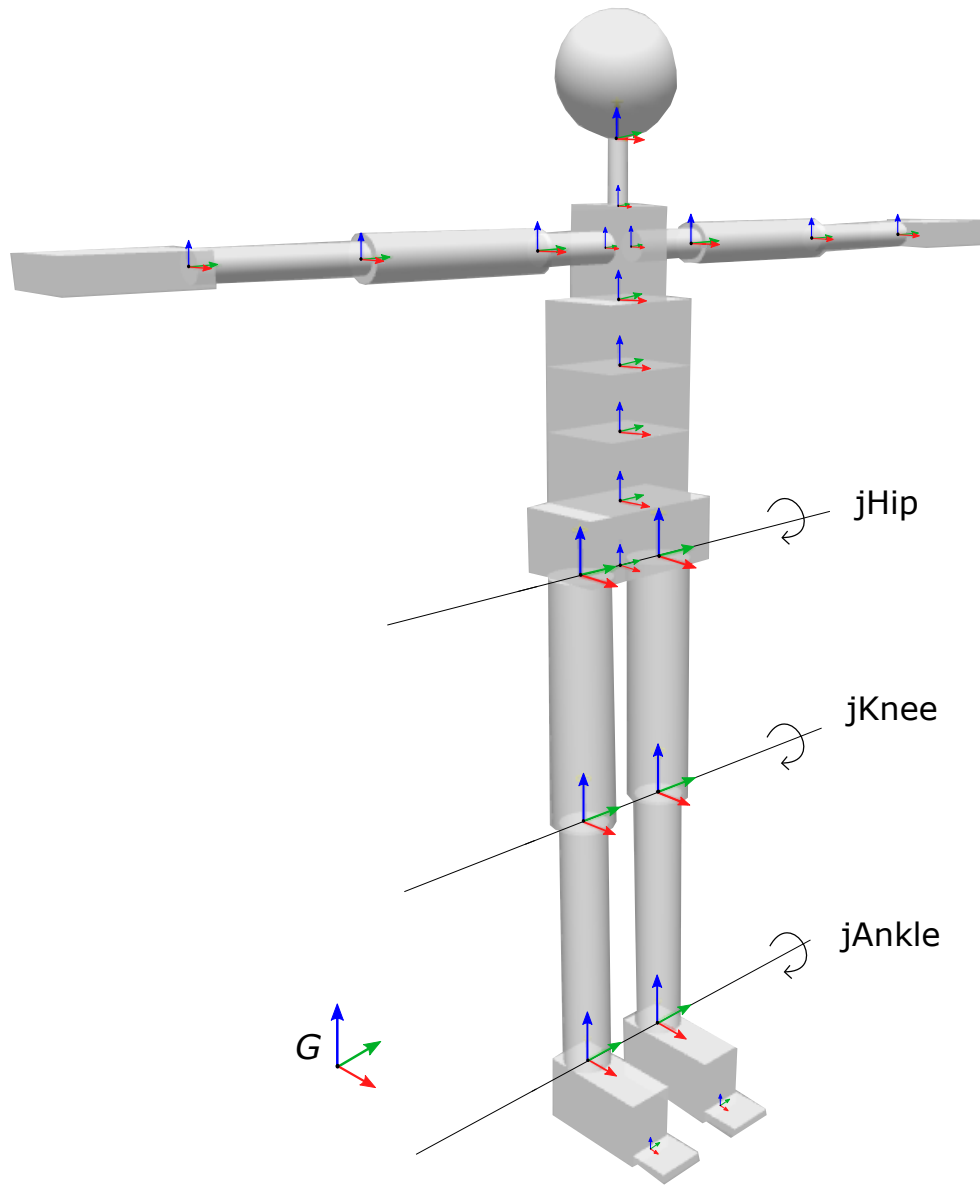
Figure 4.7: The **y** axis is enhanced in the RFs of the analysed joints since the torques along this axis are the most meaningful internal moments developed during the considered tasks.

Firstly, to deal with the different duration of the actual task (among the different trial performed by the same subject and among the same trial performed by different subjects), we have to identify its initial and final instant and consequently cut torque data. Then, in order to overlap all the profiles, data are linearly interpolated on the same predetermined time series.

Secondly, when the torques among different subjects have to be compare, a further operation has to be performed. The absolute value of the torque mostly depends on the kinematics and further on the inertial parameters of the subject and therefore, in order to compare different subjects, it has to

be normalised. The normalisation consists in the following operation:

$$\hat{\boldsymbol{\tau}} = \frac{\boldsymbol{\tau} - \boldsymbol{\tau}_{min}}{\boldsymbol{\tau}_{max} - \boldsymbol{\tau}_{min}} \tag{4.4}$$

where $\boldsymbol{\tau}$ is the vector containing measured torques, $\hat{\boldsymbol{\tau}}$ is the normalised one in the range between 0 and 1, $\boldsymbol{\tau}_{min}$ is the minimum value of the original torque and $\boldsymbol{\tau}_{max}$ is the maximum one.

4.1.3   Analysis conducted

Four different types of analysis are carried out:

A1. Comparison with state-of-the-art ID analysis;

A2. ID estimation analysis;

A3. MAP robustness analysis;

A4. Sensor fusion analysis;

The first analysis (A1) is made in order to assess the additional contribution of our work w.r.t. the previous study [1]. This previous study was conducted with our algorithm but with a different framework: they employed a 3 DoFs model and they compute the vector $\boldsymbol{d}$ with measurements coming from one force plate, one IMU located on the torso of the subject and a traditional motion-capture system marker-based. In this work only one task, not involving the robot, was performed (bowing task BH). By improving this 3 DoFs model, we delineate a 48 DoFs model (described in detail in the previous chapter) and we use additional sensors (i.e. one more force plates, the suit and F/T iCub sensors). Furthermore, we conduct experiments on tasks also involving the robot. For the fact that the model is more complex and the inputs to the algorithm have been augmented, several modifications of MAP algorithm are required. In this analysis our attempt is to: firstly (A1.1), demonstrate that for the very same experiment (BH) we are able to estimate dynamic variables even if the MAP algorithm has been modified; secondly (A1.2), to show how, starting from experiments conducted with human subject alone, the application field can be broaden to pHRI. To this end, we take into account among the dynamic variables estimated only joints torques. The torque considered is the right hip torque $\boldsymbol{\tau}_{hip}$ along the $\boldsymbol{y}$ axis (enhanced in Figure 4.7) which represents the most significant internal momentum produced while performing this specific task. For the first objective (A1.1), a qualitative comparison between right hip torques estimated by MAP algorithm in the previous work $\boldsymbol{\tau}_{hip}3DoFs$ and in our work $\boldsymbol{\tau}_{hip}48DoFs$, during bowing task (BH), is performed. Only one subject is taken into account since in the previous study only one subject was analysed. For the second objective (A1.2), a qualitative comparison between right hip torques estimated during a bowing task without pHRI (BH) $\boldsymbol{\tau}_{hip}Human$ and a bowing task with pHRI (BR) $\boldsymbol{\tau}_{hip}pHRI$ is performed. The idea is that, if the MAP algorithm is able to perform ID computation in task involving only human, it is possible to test MAP outcomes adding more sensors to the analysis and among these sensors we can

include a robot. Only one subject is taken into account since it could be exhaustive for the purpose of this qualitative comparison.

The second analysis (A2) attempts to evaluate the capability of MAP algorithm to compute the estimation of dynamic variables among different subjects, developing our previous work [63] where only one subject is analysed. To this end, employing the protocol described above, for four different tasks (BH, BR, SH, SR), carried out five times by ten different subjects, we perform ID computation and we take into account among the dynamic variables estimated only joints torques. We consider the right hip $\boldsymbol{\tau}_{RightHip}$ and the right ankle $\boldsymbol{\tau}_{RightAnkle}$ torques along the $\boldsymbol{y}$ axis (enhanced in Figure 4.7) for the bowing tasks (with and without iCub, BH and BR) and the right knee $\boldsymbol{\tau}_{RightKnee}$ and the right hip $\boldsymbol{\tau}_{RightHip}$ torques along the $\boldsymbol{y}$ axis for the squats (with and without iCub, SH and SR). These torques represent the most significant internal momentum produced while performing these specific tasks. One trial per task for each subject is considered. We make a qualitative comparison between the profiles of the torques at relevant joints computed for all subjects recruited. The mean and the standard deviation of these torques values between all subjects are computed. Through the mean we can derive a single torque profile which could represents the average trend of the torque and thus the common behaviour of all subjects. The standard deviation instead is used to express the inter-subject variability.

The third analysis (A3) is made in order to verify the MAP robustness w.r.t. modelling errors. An alternative protocol is adopted: the torques at relevant joints during a bowing task with pHRI are computed for the same subject in two conditions, with and without an additional weigh (BR and BRW) roughly positioned in correspondence of the CoM of the torso. In both the two cases, the ID analysis is performed with the biomechanical model characterized by the inertial parameters of the subject without the weigh, so this model is unsuitable in the second case, but a variance equal to 10^{-1} is associated to the model (different from the value of variance equal to 10^{-4} assigned for BR analysis). This higher value of variance assigns to the model itself a lower reliability in the computation. Only one subject, which perform five repetitions of the trial in both these two cases, is analysed. We consider the right hip torques along the $\boldsymbol{y}$ axis (enhanced in Figure 4.7). By exploiting the linearity of the system, in the assumption that the kinematics of the task is the same (since the subject is the same) the expression for the torques is:

$$\boldsymbol{\tau}_{hip}^{sub+6kg} - \boldsymbol{\tau}_{hip}^{sub} = \boldsymbol{\tau}_{hip}^{6kg} \tag{4.5}$$

where we denote with $\boldsymbol{\tau}_{hip}^{sub+6kg}$ the torque developed by the subject with the additional 6 kg mass on the torso, with $\boldsymbol{\tau}_{hip}^{sub}$ the torque developed by the subject without the weigh and $\boldsymbol{\tau}_{hip}^{6kg}$ is the theoretical torque due to the additional mass. $\boldsymbol{\tau}_{hip}^{6kg}$ can be easily computed modeling the torso and the hip with a 1 DoF system (Figure 4.8), in which the position of the additional weigh b_0 and the hip angle $\boldsymbol{\theta}(\boldsymbol{t})_{hip}$ during the movement are known.
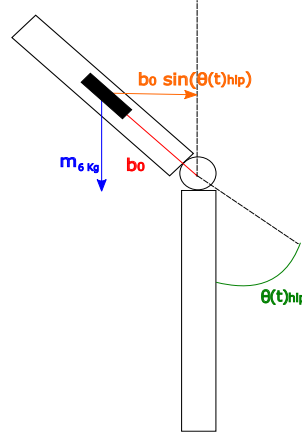
Figure 4.8: 1 DoF model to compute $\boldsymbol{\tau}_{hip}^{6kg}$: m is the additional weigh of 6 kg, b_0 its position on the torso w.r.t. the hip joint, $b_0 sin(\boldsymbol{\theta(t)}_{hip})$ is the force arm and $\boldsymbol{\theta(t)}_{hip}$ the angle developed at the hip during the movement.

The force arm of the additional weigh is a function of time, and so the torque due to the additional weigh $\boldsymbol{\tau}_{hip}^{6kg}$ varies along the movement as:

$$\boldsymbol{\tau}_{hip}^{6kg} = m_{6kg}\boldsymbol{a} \ b_0 \ sin(\boldsymbol{\theta(t)}_{hip}) \tag{4.6}$$

With the Equations (4.5) and (4.6), it is possible to calculate the error $\boldsymbol{\varepsilon}_{\boldsymbol{\tau}_{hip}}$ of the estimation of the hip torque for the subject with the 6 kg weigh, due to the employment of the unsuitable biomechanical model. The computation of the torque estimation error is:

$$\boldsymbol{\varepsilon}_{\boldsymbol{\tau}_{hip}} = |\boldsymbol{\tau}_{hip}^{sub+6kg} - \boldsymbol{\tau}_{hip}^{sub}| - \boldsymbol{\tau}_{hip}^{6kg} \tag{4.7}$$

Mean and standard deviation of the error $\boldsymbol{\varepsilon}_{\boldsymbol{\tau}_{hip}}$, as expressed in Equation (4.7), are computed for this analysis. For testing this error obtained with MAP algorithm, the very same experiments is conducted using OpenSim ID tool. Even for this analysis the unsuitable model for the torque computation in the configuration of subject with additional weigh is used, in order to evaluate OpenSim effectiveness w.r.t. modeling errors. The error $\boldsymbol{\varepsilon}_{\boldsymbol{\tau}_{hip}}$ of the torque estimation is again calculated as in Equation (4.7) and its mean and standard deviation values are computed. It is worth to notice that OpenSim does not offer the possibility of changing the model reliability in the computation.

In the last analysis (A4), we exploit the sensor fusion approach adopted by MAP algorithm. We want to prove that, performing ID computation by adding progressively different sensors' data, the variance associated to the dynamic variables estimated consequently decreases, making the estimation more reliable [1]. We remind that a distinctive feature of the MAP algorithm consists in the possibility of building the measurement Equation (3.26) for different sources of measurement in the measurement vector $\boldsymbol{y}$. We consider the sensor equations (which exploit the transformation matrices expressed in (4.1) and (4.2)) :

$$\boldsymbol{y}_{fp} = {}^{fp}\boldsymbol{X}_{foot} \ \boldsymbol{f}_{foot} \tag{4.8}$$

$$\boldsymbol{y}_{IMU} = {}^{IMU}\boldsymbol{X}_{link}\,\boldsymbol{a}_{link} \qquad (4.9)$$

$$\boldsymbol{y}_{iCubFT} = {}^{iCubFT}\boldsymbol{X}_{hand}\,\boldsymbol{f}_{hand} \qquad (4.10)$$

where with fp we refer at the force plates, with IMU we refer at the accelerometers of the Xsens IMU, with $link$ we refer at the link of the human subject where the considered accelerometer is located and with $iCubFT$ we refer at the F/T sensor mounted on the arms of iCub. The transformation matrix ${}^{IMU}\boldsymbol{X}_{link}$ allows to pass from the link RF to the RF of the IMU placed on that specific link. Starting from these equations, we build the measurement Equation (3.26) for three different cases: 1) $\boldsymbol{y} = [\ddot{\boldsymbol{q}}, \boldsymbol{y}_{fp}]$, 2) $\boldsymbol{y} = [\ddot{\boldsymbol{q}}, \boldsymbol{y}_{fp}, \boldsymbol{y}_{IMUs}]$, 3) $\boldsymbol{y} = [\ddot{\boldsymbol{q}}, \boldsymbol{y}_{fp}, \boldsymbol{y}_{IMUs}, \boldsymbol{y}_{iCubFT}]$. MAP computation is performed for each one of these cases since the addition of a sensor includes each time new information in the analysis. MAP algorithm gives as output the covariance matrix associated to all the dynamic variables included in $\boldsymbol{\mu}_{d|y}$. In order to perform the comparison between the cases defined above, we take into account only the variance (the diagonal of the covariance matrix) associated to the analysed dynamic variables. We take into account among the dynamic variables estimated only joints torques and we consider the right hip and the right ankle torques along the $\boldsymbol{y}$ axis (enhanced in Figure 4.7). The task analysed is the bowing task pHRI (BR) since a task involving iCub was needed in order to include the robot sensor measurements $case\ 3$ in the computation. The torque variance is estimated for all the ten subjects recruited and then the mean μ_{var} and the standard deviation σ_{var} between the variances of the torques of all the subjects are computed, for the three case of sensors involvement described above. We computed the mean and the standard deviation of the variance between all the subjects, in order to prove that the variance decreases for all the subjects, by adding sensors to the ID computation. In order to assess the statistical significance of these results, a t-test is performed on data. A paired-samples t-test is performed firstly between $case\ 1$ and $case\ 2$ (2 sensors: $\ddot{q}$, fp versus 3 sensors: $\ddot{q}$, fp, IMUs) and then between $case\ 2$ and $case\ 3$ (3 sensors: $\ddot{q}$, fp, IMUs versus all sensors: $\ddot{q}$, fp, IMUs, iCub).

4.2 Experimental results

In this section we present the outcomes of the experiments conducted in the modality described above. Since our work is a development of the one in [1], we firstly show a comparison between the torque estimated with the old version of MAP algorithm and our new version, adapted for a more complex model. Additionally, it is possible to enlarge the field of application of the analysis introducing the interaction with a robot within the explored tasks. A comparison between the torque estimated in tasks involving and not involving the robot is provided. Then, in order to test from a qualitative point of view the estimation capability of the algorithm, the results have been assessed on ten different subject, attempting to detect a common trend in the torque profiles among all the subjects. To evaluate, instead, the robustness of the MAP w.r.t. modelling errors, a different experiment has to be performed. The subject repeats a simple task in two different configurations, that is with and without

an additional weigh, but with the same model, that thus become unsuitable in the second case. The capability of the MAP algorithm to compensate for the modelling error is thus evaluated. Finally, since one of the distinctive features of the MAP is the possibility of performing the ID analysis considering or not considering each of the sensors (e.g. force plates, IMUs and iCub) in the computation by adding or removing related data, we assess the variances of the torques in the different cases.

4.2.1 Comparison with state-of-the-art ID analysis

In Figure 4.9 we show a comparison between the right hip torque profiles along the y axis obtained during a bowing task (BH) in [1] and in our analysis. The torques values are normalized (through Equation (4.4)) and both times series are interpolated. The trends of the two curves are comparable from a qualitative point of view.
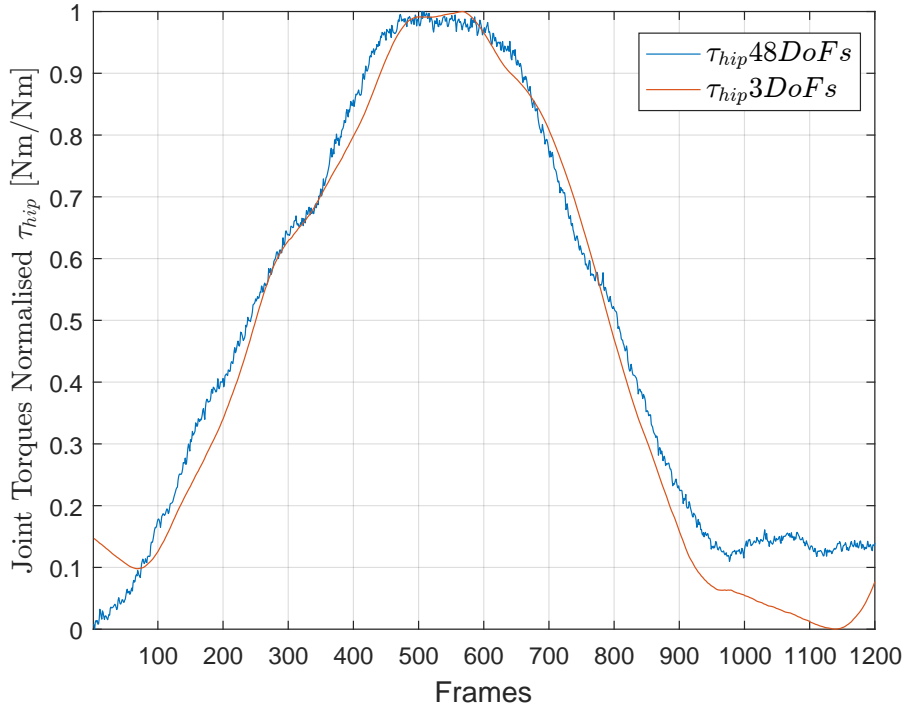

Figure 4.9: Normalised torque at the right hip $\boldsymbol{\tau}_{hip}$ during a bowing task (BH) computed by MAP a for a 3 DoFs model (blue) $\boldsymbol{\tau}_{hip}3DoFs$ and a 48 DoFs model (red) $\boldsymbol{\tau}_{hip}48DoFs$.

We show in Figure 4.10 the torque profiles of the right hip along the y axis obtained during the bowing task without pHRI (BH) $\boldsymbol{\tau}_{hip}Human$ and the bowing task with pHRI (BR) $\boldsymbol{\tau}_{hip}pHRI$ of the same subject. The torques values are normalized (through Equation (4.4)) and both times series are interpolated. The torque profile during the bowing task (BH) is quite regular, whereas the torque developed in pHRI task (BR) exhibits a significant perturbation. In the first phase of the bowing task (BR), namely the one during which the hip angle decreases until his minimum, when the subject gets in touch with the robot a perturbation (Frames from 200 to 400) is clearly visible. In the second

phase of the bowing task (BR), namely the one during which the hip angle returns to its starting value, the same behaviour is exhibited: an oscillation (Frames from 650 to 850) similar to the first one can be observed. A possible explaination of the perturbations that characterise the torque profiles is the following. When the subject gets in touch with iCub, pushing down it, the hip torque decreases because part of the weigh of torso is unloaded on iCub. On the contrary, when the subject interrupts the contact with iCub, the hip torque developed increases due to the lost support of the robot.
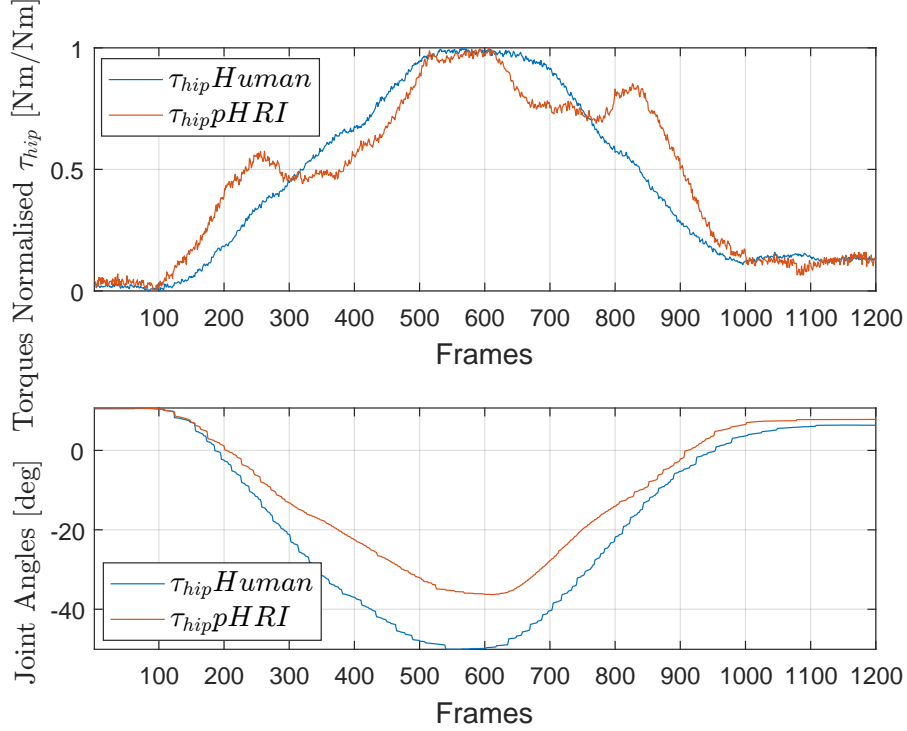

Figure 4.10: Normalised torques $\boldsymbol{\tau}_{hip}$ estimation at the right hip during a bowing task (BH, blue) $\boldsymbol{\tau}_{hip}Human$ and a pHRI bowing task (BR, red) $\boldsymbol{\tau}_{hip}pHRI$ computed by MAP.

4.2.2 ID estimation analysis

In Figure 4.11 the mean torques at the relevant joints along the $\boldsymbol{y}$ axis and the relative standard deviations, computed between all the subjects for bowing task (BH), bowing task pHRI (BR), squat (SH) and squat pHRI (SR), are shown. The mean is represented by the continuous line and the standard deviation is represented by the shadow which surround it. The torques values are normalized (through Equation (4.4)) and all subjects' times series are interpolated. In Table 4.3, for all the above cited tasks, the maximum $max[\sigma]$ and the mean value μ_σ of the standard deviations σ of the torques at the considered joints are presented.
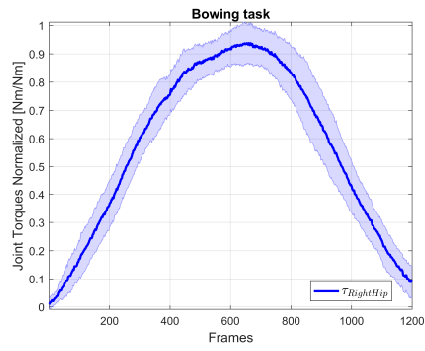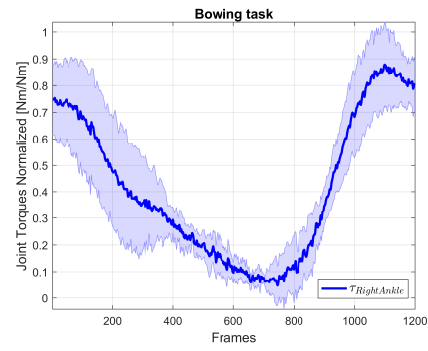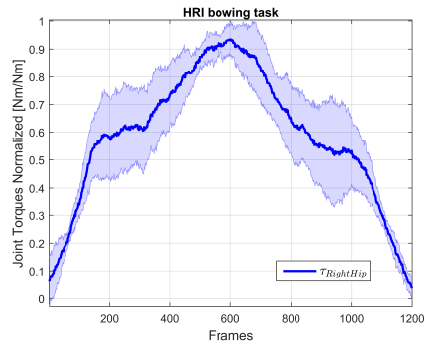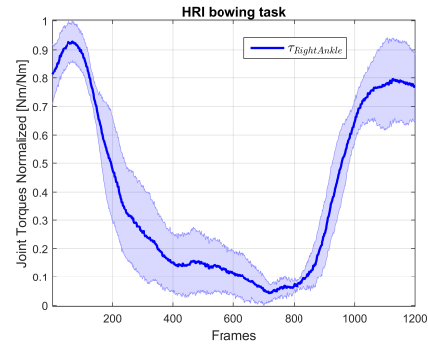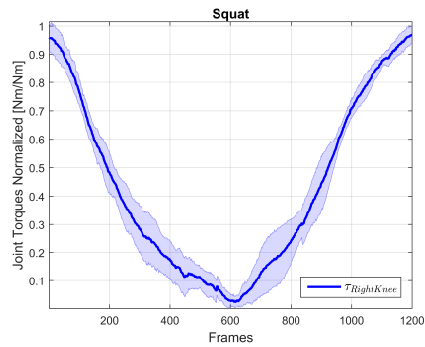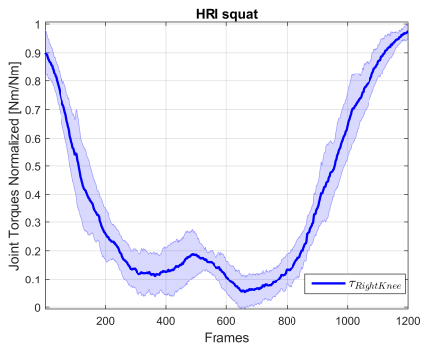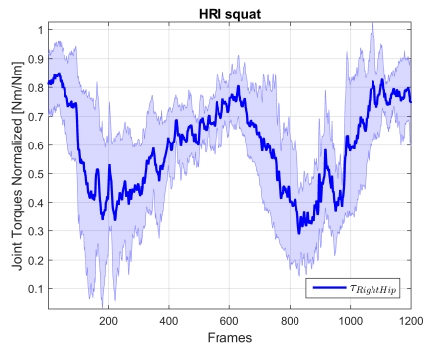
Figure 4.11: Normalised torques are presented for all the different joints and tasks considered: (a) right hip during bowing task (BH), (b) right ankle during bowing task (BH), (c) right hip during pHRI bowing task (BR), (d) right ankle during pHRI bowing task (BR), (e) right knee during squat (SH), (f) right hip during squat (SH), (g) right knee during pHRI squat (SR), (h) right hip during pHRIsquat (SR).

Table 4.3: Mean and maximum value of the standard deviations of the torques computed at the considered joints for all the tasks.

| Task	Joints	μ_σ	$max[\sigma]$
Bowing task (BH)	*Hip*	0.076939	0.129031
	Ankle	0.115863	0.230405
Bowing task pHRI (BR)	*Hip*	0.099753	0.195511
	Ankle	0.098284	0.186924
Squat (SH)	*Knee*	0.056270	0.101316
	Hip	0.101636	0.249047
Squat pHRI (SR)	*Knee*	0.073793	0.163279
	Hip	0.160254	0.359620

For those tasks not involving the iCub (BH and SH), a minor variability between subjects can be observed w.r.t. the pHRI tasks (BR and SR) as proved by the standard deviations values reported in the table (BH and SH values are lower than BR and SR ones). In addition, we can note that the standard deviations computed for the torque at the hip for bowing tasks (BH, BR) and at the knee for squats (SH, SR) are lower than the ones computed for the other joints considered for those same tasks (i.e. ankle for bowing task (BH, BR) and hip for squats (SH, SR)), as demonstrated by values in Table 4.3.

4.2.3 MAP robustness analysis

The hip torques estimated for the two cases of analysis A3 (bowing task with pHRI (BR) τ_{hip}^{sub} and bowing task with pHRI with additional weigh (BRW) $\tau_{hip}^{sub+6kg}$) by the MAP algorithm are shown in Figure 4.12, whereas the ones estimated by OpenSim ID tool (τ_{hip}^{sub} and $\tau_{hip}^{sub+6kg}$) in Figure 4.13. These torques (five repetitions of the task for both two cases BR and BRW) are represented through their mean value and standard deviation computed among all the repetitions of the task (mean represented by the continuous line and standard deviation represented by the shadow that surround the mean).
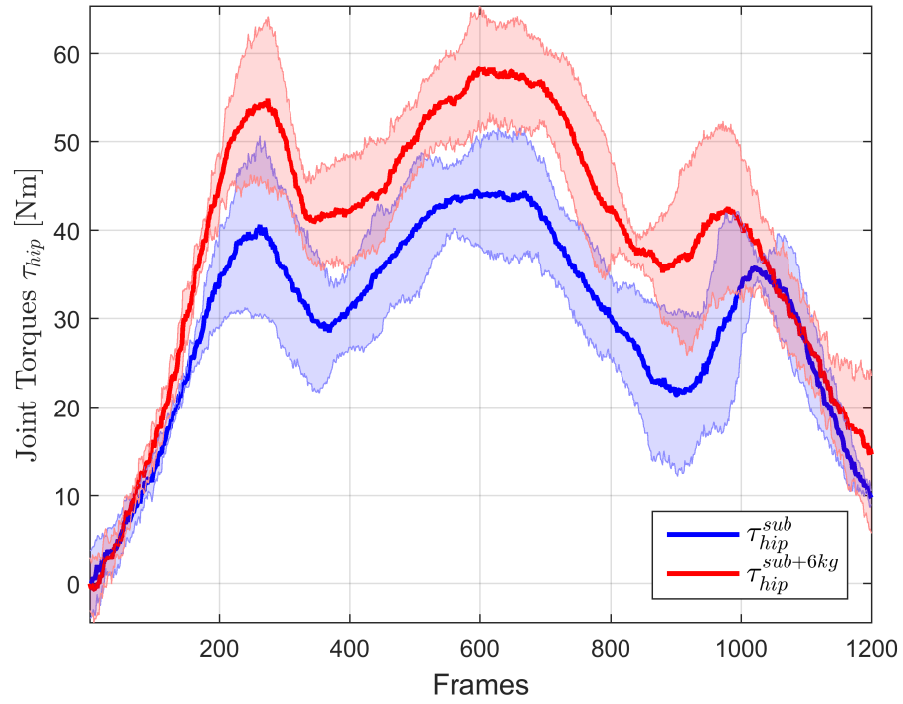
Figure 4.12: Mean torques and relative standard deviations computed by MAP algorithm at the right hip during a pHRI bowing task for one subject (BR, blue) $\boldsymbol{\tau}_{hip}^{sub}$ and the subject with the additional 6 kg mass (BRW, red) $\boldsymbol{\tau}_{hip}^{sub+6kg}$. The average is computed among five repetitions of the two tasks.
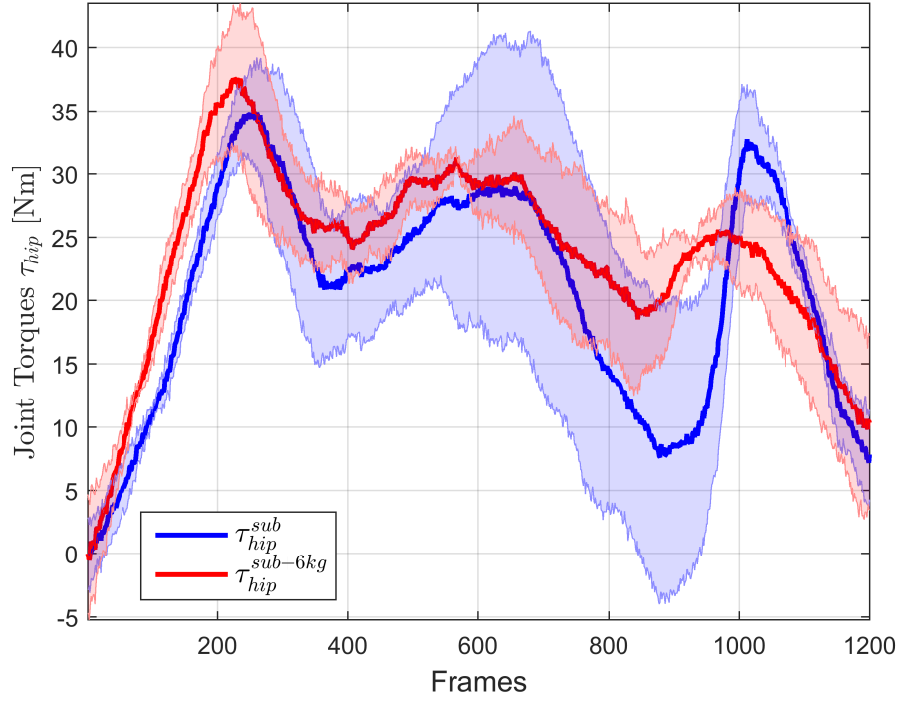
Figure 4.13: Mean torques and relative standard deviations computed by OpenSim ID tool at the right hip during a pHRI bowing task for one subject (BR, blue) $\boldsymbol{\tau}_{hip}^{sub}$ and the subject with the additional 6 kg mass (BRW, red) $\boldsymbol{\tau}_{hip}^{sub+6kg}$. The average is computed among five repetitions of the two tasks.

Mean and standard deviation of the error $\boldsymbol{\varepsilon}_{\boldsymbol{\tau}_{hip}}$, as expressed in Equation (4.7), are computed for this analysis and shown in the box plots of Figure 4.14. The box plot on the right is referred to MAP algorithm estimation error while the box plot on the left is referred to OpenSim ID tool estimation error.
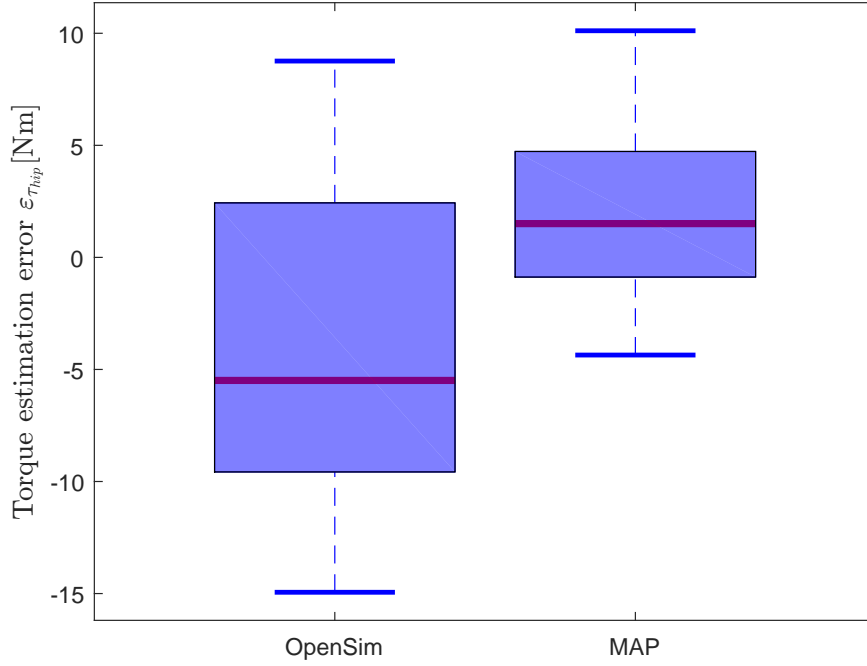
Figure 4.14: Box plots of the torque estimation error $\boldsymbol{\varepsilon}_{\boldsymbol{\tau}_{hip}}$ computed during a bowing task with pHRI performed five times by a subject without (BR) and with an additional weigh (BRW) for OpenSim ID tool and for MAP.

We can observe that the estimation error of MAP algorithm present smaller (closer to zero) value of mean and less significant value of standard deviation than the ones of OpenSim.

4.2.4   Sensor fusion analysis

Passing progressively from *case 1* to *case 3* (as shown in 4.15) the variance associated to the torque included in the estimated vector $\boldsymbol{\mu}_{d|y}$ decreases. In Figure 4.16 we show the decreasing behaviour of the mean variance of the torque at the hip and at the ankle along the $\boldsymbol{y}$ axis for a bowing task with pHRI (BR) computed between ten subjects.
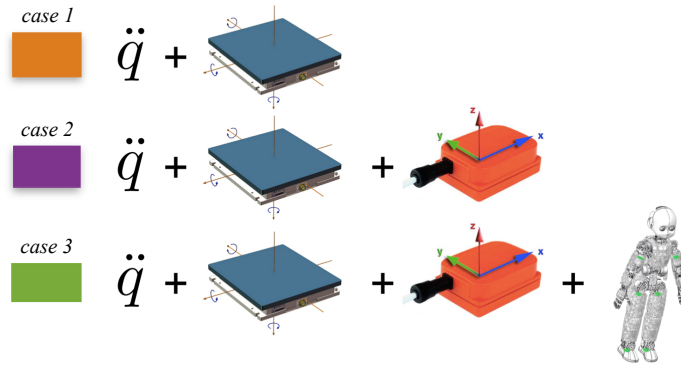
Figure 4.15: Sequence of different types of sensor that are progressively added for the estimation of $\boldsymbol{\tau}$.
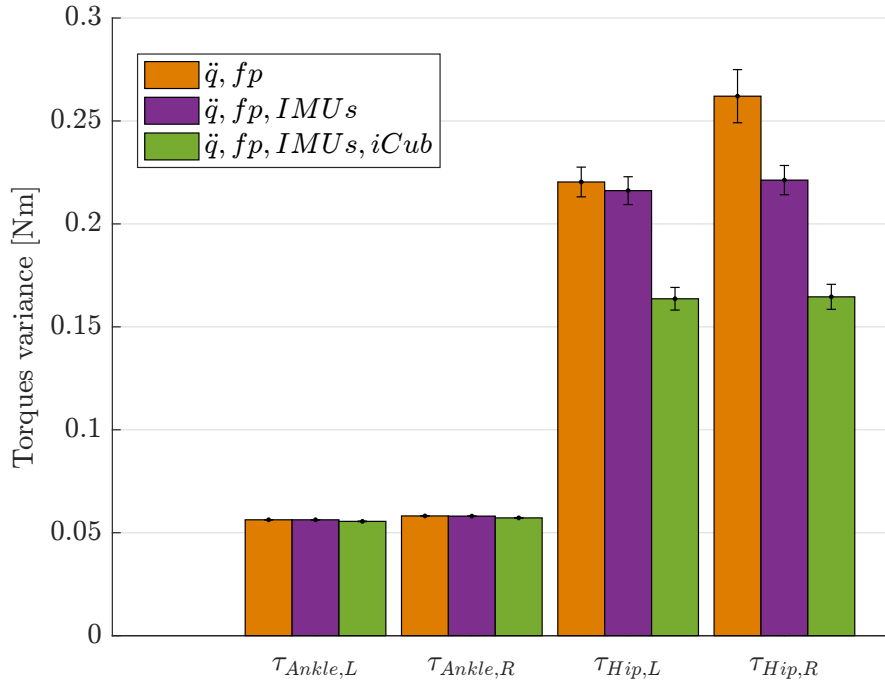
Figure 4.16: Torque variances at the left and right ankle and hip computed by MAP with the three different version of the measurement vector: 1) $\boldsymbol{y} = [\ddot{\boldsymbol{q}}, \boldsymbol{y}_{fp}]$ (orange), 2) $\boldsymbol{y} = [\ddot{\boldsymbol{q}}, \boldsymbol{y}_{fp}, \boldsymbol{y}_{IMUs}]$ (purple), 3) $\boldsymbol{y} = [\ddot{\boldsymbol{q}}, \boldsymbol{y}_{fp}, \boldsymbol{y}_{IMUs}, \boldsymbol{y}_{iCubFT}]$ (green).

By focussing on the ankles, both the right and the left, the variance values do not change significantly among the three cases. These variations are so modest that they are almost not visible in Figure 4.16. The variance for the hip torques, both the right and the left,instead, as can be seen from the results in Figure 4.16, clearly decrease while adding sensors and redoing MAP computation.

In Table 4.2.4 the values of the standard deviations of the variance σ_{var} computed for the torques at the hip and the ankle between the ten subjects are shown. We can notice that, among the different

Table 4.4: Means and standard deviations of the variances of the torques at the hip and at the ankle for a bowing task with pHRI (BR) computed between ten subjects. * is to be multiplied by 10^{-5}

Joint	case 1		case 2		case 3	
	μ_{var}	σ_{var}	μ_{var}	σ_{var}	μ_{var}	σ_{var}
LeftAnkle	0.0563	2.6503*	0.0563	2.6497*	0.0556	17.113*
RightAnkle	0.0582	4.2828*	0.0581	1.8750*	0.0573	17.760*
LeftHip	0.2201	0.0044	0.2159	0.0040	0.1639	0.0045
RightHip	0.2619	0.0092	0.2209	0.0044	0.1650	0.0055

subjects, the torque variance does not change considerably, as can be seen from the small value of the standard deviation.

The resulting p-values of the t-test performed between *case 1* and *case 2* (2 sensors: $\ddot{q}$, fp versus 3 sensors: $\ddot{q}$, fp, IMUs) and then between *case 2* and *case 3* (3 sensors: $\ddot{q}$, fp, IMUs versus all sensors: $\ddot{q}$, fp, IMUs, iCub), are displayed in Table 4.2.4.

The torques variances, adding progressively sensors to the computation, are statistically significantly decreasing as $p - value < 0.05$ for all the considered joints. We can restate that the variations of the hip torque variance is more significant than the ankle one, since hip and ankle p-value differ by two orders of magnitude. Furthermore, we can note that the iCub sensors addition decreases the variance of the torques at both the joints more than the IMUs addition (p-values computed between *case 1* and *case 2* are major than p-values computed between *case 2* and *case 3*).

Table 4.5: p-values computed with a t-test between *case 1* and *case 2* (first column) and between *case 2* and *case 3* (second column).

Joint	pValue	
	case1/case2	case2/case3
LeftAnkle	$1.61\ 10^{-6}$	$3.10\ 10^{-8}$
RightAnkle	$5.68\ 10^{-7}$	$2.07\ 10^{-8}$
LeftHip	$1.67\ 10^{-8}$	$1.39\ 10^{-11}$
RightHip	$4.01\ 10^{-8}$	$6.21\ 10^{-11}$

4.3 Discussions

With the first analysis (A1) we demonstrate that: firstly (A1.1), for the very same experiment (BH) we are able to estimate dynamic variables even if the MAP algorithm has been modified w.r.t. his previous version ([1]) secondly (A1.2), we can expand the application field of MAP algorithm from experiments conducted only with human to pHRI. As regard A1.1, since the profiles of the two torques $\tau_{hip}3DoFs$ and $\tau_{hip}48DoFs$, shown in Figure 4.9, are comparable from a qualitative point of view, we can state that MAP estimation works although the framework employed in [1] is changed. In this way, we demonstrate that MAP algorithm for human estimation can deal with models with a major number of DoFs and more sources of measurements. As regard A1.2, a possible explanation of the torque computed during a bowing task with pHRI $\tau_{hip}pHRI$ on the basis of how interaction has occurred is provided. For this reason, we can state that MAP estimation application field can be broaden to pHRI experiments.

In analysis A2, we found an average trend which represents a common behaviour between all the subjects. The several dissimilarities between torques profiles among different subjects, proved by the standard deviations values shown in Table 4.3, can be explained by different causes. On one hand, althought the explanations given to each subject about how to perform the trials were the same, the execution differs in several aspects: the total duration, the different durations of the ascending

and descending phases within the same task, the joint angles ranges developed during the movement, the force impressed on iCub arms, the duration of the contact with iCub and the kinematics in general. On the other hand, the inertial parameters of subjects are not the same and this leads them to generate forces and moments of different magnitudes. Even if the absolute values of the torques have been normalised and the torque profiles have been interpolated on the same times series to reduce inter-subjects variability, these causes have not been completely eliminated. For those tasks not involving the iCub (BH and SH), the minor variability between subjects can be explained as a consequence of the different kinematics and inertial properties. In the pHRI tasks (BR and SR), in addition to these issue, we have to consider that the forces exchanged with iCub and the duration of the contact with the robot, which differ among the subjects trials, influence the torque results. This is the reason why tasks involving iCub tend to present a major variability than the tasks performed only by humans, as demonstrated by the standard deviation values shown in Table 4.3. The fact that standard deviations computed for the torque at the hip $\tau_{RightHip}$ for bowing tasks (BH and BR) and at the knee $\tau_{RightKnee}$ for squats (SH and SR) are lower than the one (respectively $\tau_{RightAnkle}$ and $\tau_{RightHip}$) computed for the other joints considered for those same task (as can be seen in Table 4.3) can be explained as follows. During both the bowing tasks and the squats there is a joint that is more controlled during the movement (namely the hip for the bowing tasks (BH and BR) and the knee for the squats (SH and SR)) because of the kinematics of the task itself. In summary, considering all the issue discussed so far, we can say that torques computed among different subjects present an acceptable inter-subject variability in terms of standard deviation.

As regard A3 results, since MAP algorithm estimation error, whose box plot (with error mean and standard deviation) is shown on the right of Figure 4.14, is smaller than the OpenSim ID tool estimation error, whose box plot (with error mean and standard deviation) is shown on the left of Figure 4.14 we can state that MAP algorithm is able to represent the model uncertainties better then OpenSim ID tool. This can be explain with the fact that in MAP algorithm it is possible to associate a variance to the model itself, varying its reliability (high values of variance correspond to a low reliability and vice versa) while between OpenSim ID tool features this possibility is not included. Therefore, OpenSim ID tool is more sensitive to modeling errors w.r.t. MAP algorithm.

Observing the results of A4 analysis in Figure 4.16, we can state that the variance value on the ankle does not change significantly between the three different configurations of sensors, because the ankle torque estimation depends mostly on the contribution of the force plates measurements that are included in all the three cases of the computation. The hip torques estimation instead, is affected equally by the three measurement sources. Indeed, as can be seen from the results in Figure 4.16, the variance clearly decreases while adding sensors and redoing MAP computation. The results of the t-test performed strengthen the consideration discussed so far. The different p-values between hip and ankle can be explained as the influence upon the ankle of the IMUs and iCub sensors addition on the computation, is minor than the influence of these sensors upon the hip. In summary, we have

demonstrated the advantages of the sensor fusion approach in MAP computation, because it improve the reliability of the estimation, since the variance of the torques decreases in all the cases considered adding sensors data to the computation.

Chapter 5

Conclusions and future developments

5.1 Conclusions

This thesis presents an estimation framework to compute whole-body human dynamics in the field of pHRI. The analysis is conducted in a probabilistic domain, thus the dynamic variables, provided by means of Maximum-a-posteriori, are defined in terms of mean and covariance, the latter expressing the level of reliability of the estimation. In order to estimate these dynamic variables, we employ the MAP algorithm, which was originally proposed for the purpose of humanoid robot control. The classic boundary conditions in the RNEA are replaced with redundant (and noisy) measurements coming from whole-body distributed sensors. Our framework encompasses three different sources of measurements: a wearable suit provided with IMUs, two force plates and F/T sensors embedded in a humanoid robot.

Since the algorithm works in a probabilistic domain, it is possible to associate a variance to each of these sensors. The value is firstly selected according to their technical specifications (from data-sheet) then, it can be changed on the basis of their actual level of reliability, in order to weigh differently sensors role in the computation. In addition, as a distinctive feature of MAP is the possibility of adding progressively each of the available sensors data to the computation, we perform the analysis for three different cases of sensors involvement.

The first outcome of this thesis is to show the additional contribution of our work w.r.t . [1]. We have proved that MAP algorithm can deal with model characterised by a major number of DoFs and more sensors data involved in the computation. Moreover, the application field can be broaden from simple experiments conducted only on human subject to pHRI experiments.

Developing the achievements reached in [63], we have moved from a single subject analysis to a comparison between the dynamic variables estimated on ten different subjects. The relative results have been explained and some possible causes of inter-subjects variability have been discussed.

Then, the robustness of MAP algorithm w.r.t. modelling error is demonstrated. We compute the estimation employing an unsuitable model and we prove that MAP is able to deal with the model uncertainties. This is an unique feature of MAP algorithm and it represents an improvement w.r.t. ID classic methods, like OpenSim ID tool, that instead is sensitive to modelling errors.

The final contribution of the thesis consists in showing that sensor fusion approach applied to our analysis, allows to significantly improve estimation accuracy, reducing the variance of the results.

One of the main drawbacks of the framework proposed lies in the synchronization procedure among the different sources of measurements, which required a too heavy post-processing of the raw data. As regards the biomechanical model, we have to note that the joints, even if they are defined with 3 DoFs, can only be an approximation to the biological ones. Moreover, even if the model used can deal with a large number of DoFs, only simple movements are analysed for now.

The study is mainly conducted in Matlab and the related code is freely available on Github[1].

5.2   Future developments

One of the main drawbacks of our code is the synchronization between the sources of measurement. It would be advisable to employ the same methodology, whether hardware or software, for all the sensors, in order to lighten data processing. A possible solution would be to allow a seamless communication between the PC that controls the robot and the PC that controls the suit and force plates. For example, the middle-ware software YARP could implement this communication.

Additionally, since the tasks considered in our experiments are extremely simple and they involved a number of DoFs which is low w.r.t. the total of DoFs potentially allowed by our model, a reasonable development of our work would be to analyse more complex movements. Tasks engaging the upper part of the body as well as movements producing significant internal torques for a major number of DoFs, could be investigated. Moreover, as concerns the iCub side, other sensors included in the robot could be exploited for the study of interaction. It is worth to notice that, even if the human model is provided with 3 DoFs joints, they are only a rough approximation of the complexity exhibited by real biological joints. However, MAP algorithm is not limited to this particular choice and it could potentially deal with any kind of joint.

Once investigated in detail operating procedures adopted by OpenSim, it would be significant to compare the dynamic variables obtained by MAP with the ones computed by OpenSim ID tool. In this way, since OpenSim is a commercial software accepted by the scientific community, we could further validate the outcomes of the framework we proposed.

Finally, a direct extension of MAP application, by exploiting its probabilistic approach, would be to estimate dynamic variables that are not directly measured during the experiment (i.e. internal and external forces), making use of the huge opportunities afforded by sensor fusion. For example, it would

---

[1]https://github.com/Claudia-Lat/MAPest.

be possible to remove from the computation a sensor which is not reliable, nevertheless obtaining an estimation of the data that it measures.

5.3 Perspectives

The main aim of the work here presented is the estimation of human dynamic variables in pHRI domain by means of sensor fusion. Once the framework employed will be validated with all improvements proposed above, it will be possible to go beyond fixed-base constraint and investigate free movements in an extended environment. To this end, the traditional GRF sensors (i.e. force plates) will have to be substitute with seamless sensor insoles providing plantar pressure distribution, contact forces and dynamics of the human foot. In this way, our analysis could be broaden outside the controlled area of the laboratory and it could expand its applications in every day life. In this contest, it would be advisable to perform a real-time ID computation.

The main scope of forthcoming publications would be the attempt to provide human dynamics as a feedback to the robot controllers, in order to improve the accuracy of its actions. As a consequence, the control of the robot itself and its ability to predict and control mutual collaboration in physical interactions with human could be significantly enhanced.

Once having gained the full control of robot behaviour within completely safe and dependable conditions, robots future possible applications will be limitless.

Never assign a human to do a machine's job

Agent Smith, *Matrix*

Bibliography

[1] Claudia Latella, Naveen Kuppuswamy, Francesco Romano, Silvio Traversaro, and Francesco Nori. Whole-body human inverse dynamics with distributed micro-accelerometers, gyros and force sensing. *Sensors*, 16(5), 2016.

[2] Yusuke Maeda, Takayuki Hara, and Tamio Arai. Human-robot cooperative manipulation with motion estimation. In *Intelligent Robots and Systems, 2001. Proceedings. 2001 IEEE/RSJ International Conference on*, volume 4, pages 2240–2245. IEEE, 2001.

[3] Sylvain Miossec and Abderrahmane Kheddar. Human motion in cooperative tasks: Moving object case study. In *Robotics and Biomimetics, 2008. ROBIO 2008. IEEE International Conference on*, pages 1509–1514. IEEE, 2009.

[4] Anand Thobbi, Ye Gu, and Weihua Sheng. Using human motion estimation for human-robot cooperative manipulation. In *2011 IEEE/RSJ International Conference on Intelligent Robots and Systems*, pages 2873–2878. IEEE, 2011.

[5] Heni Ben Amor, Gerhard Neumann, Sanket Kamthe, Oliver Kroemer, and Jan Peters. Interaction primitives for human-robot cooperation tasks. In *2014 IEEE International Conference on Robotics and Automation (ICRA)*, pages 2831–2837. IEEE, 2014.

[6] C. L. Vaughan. Are joint torques the holy grail of human gait analysis? *Human Movement Science*, 15(3), 1996.

[7] G. Robertson, G. Caldwell, J. Hamill, G. Kamen, and S. Whittlesey. *Research methods in biomechanics, 2E*. Human Kinetics, 2013.

[8] R. D. Crowninshield and R. A. Brand. A physiologically based criterion of muscle force prediction in locomotion. *Journal of biomechanics*, 14(11), 1981.

[9] C. B. Brooks and A. M. Jacobs. The gamma mass scanning technique for inertial anthropometric measurement. *Medicine and Science in Sports*, 7(4), 1974.

[10] V. Zatsiorsky and V. Seluyanov. The mass and inertia characteristics of the main segments of the human body. *Biomechanics viii-b*, 56(2), 1983.

[11] R. F. Chandler, C. E. Clauser, J. T. McConville, H. M. Reynolds, and J. W. Young. Investigation of inertial properties of the human body. Technical report, DTIC Document, 1975.

[12] C. E. Clauser, J. T. McConville, and J. W. Young. Weight, volume, and center of mass of segments of the human body. Technical report, DTIC Document, 1969.

[13] W. T. Dempster. Space requirements of the seated operator: geometrical, kinematic, and mechanical aspects of the body, with special reference to the limbs. 1955.

[14] C. L. Vaughan, B. L. Davis, C. O. Jeremy, et al. Dynamics of human gait. 1999.

[15] E. P. Hanavan. A mathematical model of human body. Technical report, Air force aerospace medical research lab Wright-Patterson AFB OH, 1964.

[16] H. Hatze. A mathematical model for the computational determination of parameter values of anthropomorphic segments. *Journal of biomechanics*, 13(10), 1980.

[17] M. R. Yeadon. The simulation of aerial movement. *Journal of biomechanics*, 23(1), 1990.

[18] V. Cahouët, M. Luc, and A. David. Static optimal estimation of joint accelerations for inverse dynamics problem solution. *Journal of Biomechanics*, 35(11), 2002.

[19] A. J. Van den Bogert, L. Read, and B.M. Nigg. A method for inverse dynamic analysis using accelerometry. *Biomechanics*, 29(7), 1996.

[20] K. Guelton, S. Delprat, and T. M. Guerra. An alternative to inverse dynamics joint torques estimation in human stance based on a takagi–sugeno unknown-inputs observer in the descriptor form. *Control Engineering Practice*, 16(12), 2008.

[21] A. L. Bell, D. R. Pedersen, and R. A. Brand. A comparison of the accuracy of several hip center location prediction methods. *Journal of biomechanics*, 23(6), 1990.

[22] A. D. Kuo. A least-squares estimation approach to improving the precision of inverse dynamics computations. *Journal of biomechanical engineering*, 120(1), 1998.

[23] M. H. Schwartz and A. Rozumalski. A new method for estimating joint parameters from motion data. *Journal of biomechanics*, 38(1), 2005.

[24] R. Riemer, E. T. Hsiao-Wecksler, and X. Zhang. Uncertainties in inverse dynamics solutions: a comprehensive analysis and an application to gait. *Gait & posture*, 27(4), 2008.

[25] A. Cappozzo. Minimum measured-input models for the assessment of motor ability. *Journal of biomechanics*, 35(4), 2002.

[26] J. Fuller, L-J. Liu, MC. Murphy, and RW. Mann. A comparison of lower-extremity skeletal kinematics measured using skin-and pin-mounted markers. *Human Movement Science*, 16(2), 1997.

[27] J. P. Holden, J. A. Orsini, K. L. Siegel, T. M. Kepple, L. H. Gerber, and S. J. Stanhope. Surface movement errors in shank kinematics and knee kinetics during gait. *Gait & Posture*, 5(3), 1997.

[28] R. Riemer and E. T. Hsiao-Wecksler. Improving joint torque calculations: Optimization-based inverse dynamics to reduce the effect of motion errors. *Journal of biomechanics*, 41(7), 2008.

[29] M. Damsgaard, J. Rasmussen, S. T. Christensen, E. Surma, and M. De Zee. Analysis of musculoskeletal systems in the anybody modeling system. *Simulation Modelling Practice and Theory*, 14(8), 2006.

[30] Sd/fast documentation, 2001. Available online.

[31] E. Todorov, T. Erez, and Y. Tassa. Mujoco: A physics engine for model-based control. In *Intelligent Robots and Systems (IROS), 2012 IEEE/RSJ International Conference on*. IEEE, 2012.

[32] T. Erez, Y. Tassa, and E. Todorov. Simulation tools for model-based robotics: Comparison of bullet, havok, mujoco, ode and physx. In *Robotics and Automation (ICRA), 2015 IEEE International Conference on*. IEEE, 2015.

[33] J. Hicks. Open sim documentation, 2013. Available online.

[34] S. L. Delp, Anderson F. C., A. S. Arnold, P. Loan, A. Habib, C.T. John, E. Guendelman, and D. G. Thelen. Opensim: Open-source software to create and analyze dynamic simulations of movement. *IEEE Transactions on Biomedical Engineering*, 54(11), 2007.

[35] J. Dunne. *User's Guide*. SimTK.org, 2014.

[36] M. Sherman, A. Seth, and S. L. Delp. What is a moment arm? calculating muscle effectiveness in biomechanical models using generalized coordinates. In *ASME 2013 International Design Engineering Technical Conferences and Computers and Information in Engineering Conference*, 2013.

[37] Roy Featherstone. *Rigid body dynamics algorithms*. Springer, 2014.

[38] L. Sciavicco and B. Siciliano. *Modelling and control of robot manipulators*. Springer Science & Business Media, 2012.

[39] Francesco Nori, Naveen Kuppuswamy, and Silvio Traversaro. Simultaneous state and dynamics estimation in articulated structures. In *Intelligent Robots and Systems (IROS), 2015 IEEE/RSJ International Conference on*. IEEE, 2015.

[40] Daniel Roetenberg, Henk Luinge, and Per Slycke. Xsens mvn: full 6dof human motion tracking using miniature inertial sensors. *Xsens Motion Technologies BV, Tech. Rep*, 2009.

[41] Xsens Technologies. *MVN User Manual*. Xsens Technologies, 2015.

[42] G. Metta, G. Sandini, D. Vernon, D. Caldwell, N. Tsagarakis, R. Beira, A. Ijspeert, L. Righetti, G. Cappiello, G. Stellin, et al. The robotcub project - an open framework for research in embodied cognition. In *Humanoids Workshop, Proceedings of the IEEE-RAS International Conference on Humanoid Robots*, number BIOROB-CONF-2006-014, 2006.

[43] M. Fumagalli, S. Ivaldi, M. Randazzo, L. Natale, G. Metta, G. Sandini, and F. Nori. Force feedback exploiting tactile and proximal force/torque sensing. *Autonomous Robots*, 33(4), 2012.

[44] G. Metta, P. Fitzpatrick, and L. Natale. Yarp: yet another robot platform. *International Journal on Advanced Robotics Systems*, 3(1), 2006.

[45] K. Engel, Herpers R., and U. Hartmann. *Theoretical biomechanics*, chapter Chapter 5 Biomechanical Computer Models. InTech, 2011.

[46] K. H. E. Kroemer, S. H. Stover, S. K. Meadows, and S. Deutsch. *Ergonomic Models of Anthropometry, Human Biomechanics and Operator-Equipment Interfaces: Proceedings of a Workshop*, chapter Chapter 3 Biomechanical Models. National Academy Press, 1988.

[47] W. S. P. Robertson. A modern take on the theoretical modelling of inertial properties of a human body for biomechanical simulations. In *MODSIM2013: The 20th International Congress on Modelling and Simulation*, 2013.

[48] P De Leva. Adjustments to zatsiorsky-seluyanov's segment inertia parameters. *Journal of biomechanics*, 29(9), 1996.

[49] D.J. Pearsall, J.G. Reid, and R. Ross. Inertial properties of the human trunk of males determined from magnetic resonance imaging. *Annals of biomedical engineering*, 22(6), 1994.

[50] J. L. Durkin, J. J. Dowling, and D. M. Andrews. The measurement of body segment inertial parameters using dual energy x-ray absorptiometry. *Journal of biomechanics*, 35(12), 2003.

[51] R. K. Jensen. Estimation of the biomechanical properties of three body types using a photogrammetric method. *Journal of biomechanics*, 11(8), 1978.

[52] H. Hatze. A comprehensive model for human motion simulation and its application to the take-off phase of the long jump. *Biomechanics*, 14(3), 1981.

[53] J. Wicke, G. A Dumas, and P. A. Costigan. A comparison between a new model and current models for estimating trunk segment inertial parameters. *Journal of biomechanics*, 42(1), 2009.

[54] R. Drillis, R. Contini, and M. Bluestein. Body segment parameters - a survey of measurments tecniques. Technical report, National Academy of Sciences and National Research Council, 1964.

[55] H. F. J. M. Koopman. *The three-dimensional analysis and prediction of human walking.* 1989.

[56] G. Anastasi, G. Motta, and P. Balboni. *Trattato di anatommia umana.* Edi. Ermes, 2012.

[57] Teachmeanatomy. Available online.

[58] JJ Gerhardt. International standard orthopedic measurements. *Wall Chart. SFTR Recording of Joint Motion and Position in the Neutral-0-Method. Indiana, USA: Orthopedic Equipment Company, Bourbon,* 1964.

[59] V Wright and JMH Moll. Normal range of spinal mobility. *Ann. rheum. Dis,* 30:381, 1971.

[60] Alison Middleditch and Jean Oliver. *Functional anatomy of the spine.* Elsevier Health Sciences, 2005.

[61] JJ Gerhardt. Clinical measurements of joint motion and position in the neutral-zero method and sftr recording: basic principles. *International rehabilitation medicine,* 5(4):161–164, 1983.

[62] S. J. Orfanidis. *Introduction to signal processing,* chapter Chapter 8.

[63] C. Latella, F. Romano, S. Traversaro, M. Lazzaroni, M. Lorenzini, and F. Nori. Human whole-body motion and forces estimation during human-robot interaction, 2016. Humanoids 2016.

[64] W. S. Erdmann. Geometry and inertia of the human body - review of research. *Acta of Bioengineering and Biomechanics,* 1(1), 1999.

[65] I. P. Herman. *Physics of the human body,* chapter Chapter 1 Terminology, the standard human, and scaling. Springer, 2007.

[66] J. Bjornstrup. Estimation of human body segments parameters - historical background. Internal tech-report, 1995.

[67] D. A. Winter. *Biomechanics and motor control of human movement,* chapter Chapter 4 Anthromopetry. Fourth, 2009.

[68] R. Dumas, E. Nicol, and L. Chèze. Influence of the 3d inverse dynamic method on the joint forces and moments during gait. *Journal of Biomechanical Engineering,* 129, 2007.

[69] R. Dumas, E. Nicol, and L. Chèze. Influence of perturbated gait data on four 3d inverse dynamic methods. In *9th Symposium on 3D Analysis of Human Movement, France,* 2006.

Appendix A

Recursive Newton-Euler Algorithm

Among the several ID formulations we are interested in the Newton-Euler one [38], based on a balance of all the forces and moments acting on the generic link. This yields to a set of equations whose structure allows a recursive type of solution: a forward recursion is performed for propagating links velocities and accelerations, followed by a backward recursion for propagating forces. For the system composed by the link i and the joint $i+1$, according to Denavit-Hartenberg convention for joint numbering [38], one can refer to the centre of mass C_i to characterize the following parameters:

⋄ m_i mass of the link,

⋄ $\bar{\boldsymbol{I}}_i$ inertia tensor of the link,

⋄ $\boldsymbol{I}_{m_i}$ moment of inertia of joint,

⋄ $\boldsymbol{r}_{i-1,C_i}$ vector from origin of frame $(i-1)$ to centre of mass C_i,

⋄ $\boldsymbol{r}_{i,C_i}$ vector from origin of frame i to centre of mass C_i,

⋄ $\boldsymbol{r}_{i-1,i}$ vector from origin of frame $(i-1)$ to origin of frame i.

The velocities and accelerations to be considered are:

⋄ $\dot{\boldsymbol{p}}_{C_i}$ linear velocity of centre of mass C_i,

⋄ $\dot{\boldsymbol{p}}_i$ linear velocity of origin of frame i,

⋄ $\boldsymbol{\omega}_i$ angular velocity of link,

⋄ $\boldsymbol{\omega}_{m_i}$ angular velocity of joint,

⋄ $\ddot{\boldsymbol{p}}_{C_i}$ linear acceleration of centre of mass C_i,

⋄ $\ddot{\boldsymbol{p}}_i$ linear acceleration of origin of frame i,

⋄ $\dot{\boldsymbol{\omega}}_i$ angular acceleration of link,

⋄ $\dot{\boldsymbol{\omega}}_{m_i}$ angular acceleration of joint,

$\diamond$ $\boldsymbol{g}_0$ gravity acceleration.

The forces and moments to be considered are:

$\diamond$ $\boldsymbol{f}_i$ force exerted by link $(i-1)$ on link i,

$\diamond$ $-\boldsymbol{f}_{i+1}$ force exerted by link $(i+1)$ on link i,

$\diamond$ $\boldsymbol{\mu}_i$ moment exerted by link $(i-1)$ on link i w.r.t. origin of frame $(i-1)$,

$\diamond$ $-\boldsymbol{\mu}_{i+1}$ moment exerted by link $(i+1)$ on link i w.r.t. origin of frame i.

The Newton equation for the translational motion of the CoM can be written as:

$$\boldsymbol{f}_i - \boldsymbol{f}_{i+1} + m_i \boldsymbol{g}_0 = m_i \ddot{\boldsymbol{p}}_{C_i} \tag{A.1}$$

The Euler equation for the rotational motion of joint (referring moments to the CoM) can be written as:

$$\boldsymbol{\mu}_i + \boldsymbol{f}_i \times \boldsymbol{r}_{i-1,C_i} - \boldsymbol{\mu}_{i+1} - \boldsymbol{f}_{i+1} \times \boldsymbol{r}_{i,C_i} = \frac{d}{\mathrm{d}t}(\bar{\boldsymbol{I}}_i \boldsymbol{\omega}_i + k_{r,i+1}\, \dot{\boldsymbol{q}}_{i+1}\, \boldsymbol{I}_{m_{i+1}}\, \boldsymbol{z}_{m_{i+1}}) \tag{A.2}$$

where $\boldsymbol{z}_{m_{i+1}}$ is the unit vector of axis $\boldsymbol{z}$ of frame $(i+1)$, $\boldsymbol{k}_{r,i+1}$ is the gear reduction ratio and $\boldsymbol{q}$ is the vector of joint variables. Notice that the gravitational force $m_i \boldsymbol{g}_0$ does not generate any moment, since it is expressed at the CoM. In order to express the inertia tensor in the current frame (for having a constant tensor), according to the formula $\bar{\boldsymbol{I}}_i = \boldsymbol{R}_i\, \bar{\boldsymbol{I}}_i\, \boldsymbol{R}_i^T$, where $\boldsymbol{R}_i$ is the rotation matrix for frame i to the base frame, by substituting this relation in the first term on the right-hand side of the Equation (A.2):

$$
\begin{aligned}
\frac{d}{\mathrm{d}t}(\bar{\boldsymbol{I}}_i \boldsymbol{\omega}_i) = \quad & \dot{\boldsymbol{R}}_i\, \bar{\boldsymbol{I}}_i\, \boldsymbol{R}_i^T\, \boldsymbol{\omega}_i + \boldsymbol{R}_i\, \bar{\boldsymbol{I}}_i\, \dot{\boldsymbol{R}}_i^T\, \boldsymbol{\omega}_i + \boldsymbol{R}_i\, \bar{\boldsymbol{I}}_i\, \boldsymbol{R}_i^T\, \dot{\boldsymbol{\omega}}_i \\
= \quad & \boldsymbol{S}(\boldsymbol{\omega}_i)\, \boldsymbol{R}_i\, \bar{\boldsymbol{I}}_i\, \boldsymbol{R}_i^T\, \boldsymbol{\omega}_i + \boldsymbol{R}_i\, \bar{\boldsymbol{I}}_i\, \boldsymbol{R}_i^T\, \boldsymbol{S}^T(\boldsymbol{\omega}_i)\, \boldsymbol{\omega}_i + \boldsymbol{R}_i\, \bar{\boldsymbol{I}}_i\, \boldsymbol{R}_i^T\, \dot{\boldsymbol{\omega}}_i \\
= \quad & \bar{\boldsymbol{I}}_i\, \dot{\boldsymbol{\omega}}_i + \boldsymbol{\omega}_i \times (\bar{\boldsymbol{I}}_i \boldsymbol{\omega}_i)
\end{aligned} \tag{A.3}
$$

where the second term represents the gyroscopic torque induced by the dependence of $\bar{\boldsymbol{I}}_i$ on link orientation. Moreover, by observing that the unity vector $\boldsymbol{z}_{m_{i+1}}$ rotates accordingly to link i, the derivative needed in the second term on the right-hand side of Equation (A.2) is:

$$\frac{d}{\mathrm{d}t}(\dot{\boldsymbol{q}}_{i+1}\, \boldsymbol{I}_{m_{i+1}}\, \boldsymbol{z}_{m_{i+1}}) = \ddot{\boldsymbol{q}}_{i+1}\, \boldsymbol{I}_{m_{i+1}}\, \boldsymbol{z}_{m_{i+1}} + \dot{\boldsymbol{q}}_{i+1}\, \boldsymbol{I}_{m_{i+1}}\, \boldsymbol{\omega}_i \times \boldsymbol{z}_{m_{i+1}} \tag{A.4}$$

By substituting the Equations (A.3) and (A.4) in (A.2) we obtain:

$$
\begin{aligned}
\boldsymbol{\mu}_i + \boldsymbol{f}_i \times \boldsymbol{r}_{i-1,C_i} - \boldsymbol{\mu}_{i+1} - \boldsymbol{f}_{i+1} \times \boldsymbol{r}_{i,C_i} = \quad & \bar{\boldsymbol{I}}_i \dot{\boldsymbol{\omega}}_i + \boldsymbol{\omega}_i \times (\bar{\boldsymbol{I}}_i \boldsymbol{\omega}_i) \\
+ k_{r,i}\, \ddot{\boldsymbol{q}}_{i+1}\, \boldsymbol{I}_{m_{i+1}}\, \boldsymbol{z}_{m_{i+1}} + k_{r,i}\, \dot{\boldsymbol{q}}_{i+1}\, \boldsymbol{I}_{m_{i+1}}\, \boldsymbol{\omega}_i \times \boldsymbol{z}_{m_{i+1}} &
\end{aligned} \tag{A.5}
$$

The generalized force at joint i can be computed by projecting the force $\boldsymbol{f}_i$ for a prismatic joint, or the moment $\boldsymbol{\mu}_i$ for a revolute joint, along the joint axis. In addition, there is the contribution of the joint inertia torque $\boldsymbol{k}_{r,i}\,\boldsymbol{I}_{m_i}\,\dot{\boldsymbol{\omega}}_{m_i^T}\,\boldsymbol{z}_{m_i}$. Hence, the generalized force at joint i is expressed by:

$$\boldsymbol{\tau}_i = \begin{cases} \boldsymbol{f}_i^T \boldsymbol{z}_{i-1} + \boldsymbol{k}_{ri}\,\boldsymbol{I}_{m_i}\,\dot{\boldsymbol{\omega}}_{m_i}^T\,\boldsymbol{z}_{m_i} & \textit{for a prismatic joint} \\ \boldsymbol{\mu}_i^T \boldsymbol{z}_{i-1} + \boldsymbol{k}_{ri}\,\boldsymbol{I}_{m_i}\,\dot{\boldsymbol{\omega}}_{m_i}^T\,\boldsymbol{z}_{m_i} & \textit{for a revolute joint} \end{cases} \tag{A.6}$$

Since for the ID analysis the angular and linear accelerations of link i and joint i are required, this computation can be carried out starting from:

$$\boldsymbol{\omega}_i = \begin{cases} \boldsymbol{\omega}_{i-1} & \textit{prismatic} \\ \boldsymbol{\omega}_{i-1} + \dot{\boldsymbol{\theta}}_i \boldsymbol{z}_{i-1} & \textit{revolute} \end{cases} \tag{A.7}$$

$$\dot{\boldsymbol{p}}_i = \begin{cases} \dot{\boldsymbol{p}}_{i-1} + \dot{\boldsymbol{d}}_i \boldsymbol{z}_{i-1} + \boldsymbol{\omega}_i \times \boldsymbol{r}_{i-1,i} & \textit{prismatic} \\ \dot{\boldsymbol{p}}_{i-1} + \boldsymbol{\omega}_i \times \boldsymbol{r}_{i-1,i} & \textit{revolute} \end{cases} \tag{A.8}$$

For the angular and linear accelerations of the link, $\boldsymbol{\omega}_i$ and $\dot{\boldsymbol{p}}_i$ differentiation yields to:

$$\dot{\boldsymbol{\omega}}_i = \begin{cases} \dot{\boldsymbol{\omega}}_{i-1} & \textit{prismatic} \\ \dot{\boldsymbol{\omega}}_{i-1} + \ddot{\boldsymbol{\theta}}_i \boldsymbol{z}_{i-1} + \dot{\boldsymbol{\theta}}_i \boldsymbol{\omega}_{i-1} \times \boldsymbol{z}_{i-1} & \textit{revolute} \end{cases} \tag{A.9}$$

$$\ddot{\boldsymbol{p}}_i = \begin{cases} \ddot{\boldsymbol{p}}_{i-1} + \ddot{\boldsymbol{d}}_i\,\boldsymbol{z}_{i-1} + 2\dot{\boldsymbol{d}}_i\,\boldsymbol{\omega}_i \times \boldsymbol{z}_{i-1} + \dot{\boldsymbol{\omega}}_i \times \boldsymbol{r}_{i-1,i} + \boldsymbol{\omega}_i \times (\boldsymbol{\omega}_i \times \boldsymbol{r}_{i-1,i}) & \textit{prismatic} \\ \ddot{\boldsymbol{p}}_{i-1} + \dot{\boldsymbol{\omega}}_i \times \boldsymbol{r}_{i-1,i} + \boldsymbol{\omega}_i \times (\boldsymbol{\omega}_i \times \boldsymbol{r}_{i-1,i}) & \textit{revolute} \end{cases} \tag{A.10}$$

By remembering that in the case where $\boldsymbol{p}_{i+1}$ is fixed in frame $i+1$, since $\dot{\boldsymbol{p}}^{i+1} = 0$, the linear velocity can be expressed as:

$$\dot{\boldsymbol{p}}^i = \dot{\boldsymbol{o}}_{i+1}^i + \boldsymbol{\omega}_{i+1}^i \times \boldsymbol{r}_{i+1}^i \tag{A.11}$$

We can derive, by differentiating w.r.t. the time this equation, the acceleration of the centre of mass C_i of link i, required by the Newton equation, considering that $\dot{\boldsymbol{r}}_{i,C_i}^i = 0$:

$$\ddot{\boldsymbol{p}}_{C_i} = \ddot{\boldsymbol{p}}_i + \dot{\boldsymbol{\omega}}_i \times \boldsymbol{r}_{i,C_i} + \boldsymbol{\omega}_i \times (\boldsymbol{\omega}_i \times \boldsymbol{r}_{i,C_i}) \tag{A.12}$$

This acceleration can be expressed as a function of the velocity and acceleration of the origin of frame i. Finally, by remembering that the total angular velocity of the joint is:

$$\boldsymbol{\omega}_{m_i} = \boldsymbol{\omega}_{i-1} + \boldsymbol{k}_{ri}\,\dot{\boldsymbol{q}}_i\,\boldsymbol{z}_{m_i} \tag{A.13}$$

the angular acceleration of the joint can be obtained by time differentiation of the Equation (A.13):

$$\dot{\boldsymbol{\omega}}_{m_i} = \dot{\boldsymbol{\omega}}_{i-1} + \boldsymbol{k}_{ri} \, \ddot{q}_i \, \boldsymbol{z}_{m_i} + \boldsymbol{k}_{ri} \, \dot{q}_i \, \boldsymbol{\omega}_{i-1} \times \boldsymbol{z}_{m_i} \tag{A.14}$$

The resulting Newton-Euler equations of motion are not in closed form, since the motion of a single link is coupled to the motion of the other links through the kinematic relationship for velocities and accelerations. A computationally recursive algorithm can be constructed: a forward recursion relative to the propagation of velocities and accelerations and a backward recursion for the propagation of forces and moments along the structure. Having computed the velocities and accelerations from the base link to the end-effector, once $\boldsymbol{h} = [\boldsymbol{f}_{n+1}^T \ \boldsymbol{\mu}_{n+1}^T]^T$ is given (eventually $\boldsymbol{h} = 0$), a backward recursion can be carried out, rewriting the Newton equation as:

$$\boldsymbol{f}_i = \boldsymbol{f}_{i+1} + m_i \ddot{\boldsymbol{p}}_{C_i} \tag{A.15}$$

since the contribution of gravity acceleration has already been included in $\ddot{\boldsymbol{p}}_{C_i}$. Further, the Euler equation gives:

$$\boldsymbol{\mu}_i = -\boldsymbol{f}_i \times (\boldsymbol{r}_{i-1,i} + \boldsymbol{r}_{i,C_i}) + \boldsymbol{\mu}_{i+1} + \boldsymbol{f}_{i+1} \times \boldsymbol{r}_{i,C_i} + \bar{\boldsymbol{I}}_i \dot{\boldsymbol{\omega}}_i + \boldsymbol{\omega}_i \times (\bar{\boldsymbol{I}}_i \boldsymbol{\omega}_i)$$
$$+ \boldsymbol{k}_{r,i+1} \, \ddot{q}_{i+1} \, \boldsymbol{I}_{m_{i+1}} \, \boldsymbol{z}_{m_{i+1}} + \boldsymbol{k}_{r,i+1} \, \dot{q}_{i+1} \, \boldsymbol{I}_{m_{i+1}} \, \boldsymbol{\omega}_i \times \boldsymbol{z}_{m_{i+1}} \tag{A.16}$$

where $\boldsymbol{r}_{i-1,C_i}$ has been expressed as the sum of the two vectors appearing already in the forward recursion. Finally, the generalized forces resulting at the joints can be computed as:

$$\boldsymbol{\tau}_i = \begin{cases} \boldsymbol{f}_i^T \, \boldsymbol{z}_{i-1} + \boldsymbol{k}_{ri} \, \boldsymbol{I}_{m_i} \, \dot{\boldsymbol{\omega}}_{m_i}^T \, \boldsymbol{z}_{m_i} + \boldsymbol{f}_{vi} \, \dot{d}_i + \boldsymbol{f}_{si} \, sgn(\dot{d}_i) & prismatic \\ \boldsymbol{\mu}_i^T \, \boldsymbol{z}_{i-1} + \boldsymbol{k}_{ri} \, \boldsymbol{I}_{m_i} \, \dot{\boldsymbol{\omega}}_{m_i}^T \, \boldsymbol{z}_{m_i} + \boldsymbol{f}_{vi} \, \dot{\theta}_i + \boldsymbol{f}_{si} \, sgn(\dot{\theta}_i) & revolute \end{cases} \tag{A.17}$$

where joint viscous and Coulomb friction torques have been included. In the above derivation, it has been assumed that all vectors are referred to the base frame. However, the recursion is computationally more efficient if all vectors are referred to the current frame on link i, thus they need to be transformed (by means of a proper rotation matrix $\boldsymbol{R}$).

There are two methods for derivation of the equations of motion in the joint space: besides the Newton-Euler formulation, the other approach is based on the Lagrange formulation. Both of them allow computing the relationship between the joints torques and the motion of the structure but a comparison reveals different features. The Lagrange formulation has the following advantages:

⋄ it is systematic and of immediate comprehension;

⋄ it provides the equations of motion in a compact analytical form containing the inertia matrix, the matrix in the centrifugal and Coriolis forces and the vector of gravitational forces. Such a form is advantageous for control design;

⋄ it is effective if it is wished to include more complex mechanical effects such as flexible link deformation.

The Newton-Euler formulation has the following fundamental advantage:

⋄ it is an inherently recursive method that is computationally efficient;

⋄ it provide real-time computation of dynamic variables.

Four different methods to compute ID using the Newton-Euler equations of motion, applied recursively to each segment of the body, have been proposed in the literature [68]. These methods are based on: vectors and Euler angles, wrenches and quaternions, homogeneous matrices and generalized coordinates and forces.

In the method based on vectors and Euler angles, the linear acceleration $\boldsymbol{a}$, the angular velocity $\boldsymbol{\omega}$ and the angular acceleration $\boldsymbol{\alpha}$ are computed starting from the Euler angles (φ, θ, ψ) and their derivatives and then forces and moments are computed in two separate times. In the method based on quaternions and wrenches, quaternion algebra is used to compute $\boldsymbol{a}$, $\boldsymbol{\omega}$ and $\boldsymbol{\alpha}$ and then the wrench ($\boldsymbol{F}$, $\boldsymbol{M}$) is computed at once. The method based on homogeneous matrices consists in building an acceleration matrix $\boldsymbol{A}$ where all the linear and angular kinematic variables are included and then an homogeneous matrix $\boldsymbol{\phi}$ including the computed forces and moments. In the method based on generalized coordinates and forces, the kinematics, computed as direct derivatives, and forces and moments are computed simultaneously.

Comparing the four methods, when only considering the kinematics, the difference remains rather limited, when considering the dynamics significant differences are observed. In the method based on vectors and Euler angles the joint forces and the joint moments are computed in two different systems and thus the successive coordinate transformation may have an influence on the result. In the other three methods, the forces and moments are computed simultaneously in the same system, but in the method based on homogeneous matrices this process is done in a redundant manner and in the method based on generalized coordinates and forces rigid body constraints are additionally taken into account through Lagrange multipliers. The first method facilitates a clinical interpretation of kinematic patterns but presents some discontinuity and singularity problems in dynamic computation. For that, the second and the third methods are more used, while the fourth method is more specific and may be used in particular cases. A complementary study [69] has demonstrated different sensitivities to noise, with higher perturbations observed for the first and the fourth method.

Appendix B

Anthropometry

Human motor activity is determined by the response of the subject to constantly changing external and internal stimuli. The motor response has a definite pattern and the kinematic analysis of movement is the process of measuring the kinematic quantities used to describe this pattern. The most important characteristics are: the paths of motion, linear and angular displacements curves, amplitudes and ranges of motion, the instantaneous and average velocities and their direction and finally the linear and angular accelerations of the body segments under investigation. All these quantities are concerned with the influence of different forces and moments acting on the body during the performance of a given activity. To determine these forces and moments, accurate data on the mass, the location of CoM, the momentum of inertia and the dimensions of the subject body segments need to be defined [54]. For the purpose of a single-subject investigation all these values can be easily collected. From the 17th century to the present time, several methods have been outlined: mechanical and electromechanical, optical (for geometry), geometric (for inertia), penetrating, calculation, modelling [64]. Several studies have been conducted also in order to find standard human dimensions and inertial characteristics [65] but they are a too much huge approximation. These properties must be subject-specific, as body shape and weigh distribution vary significantly between members of the human population. Therefore in order to conduct large-scale studies, considering that it is not feasible to make manual measurements on each subject, a method for body parameters estimation is required [66]. Thanks to the findings of anthropometry, the science that deals with the measurement of size, weigh and proportions of the human body, statistical data about the distribution of body dimension in the global population have been collected. By using these sets of anthropometric data it is possible to obtain subject-specific body parameters in an automatic way [65].

Starting from the estimated parameters it is possible to design biomechanical model for simulation and prediction of realistic movements. The anthropometric measurements are used as inputs into a geometric humanoid model, in which each body segment is consisted of a certain number of regular volumetric shapes depending on the complexity of the shape and on the complexity of the model. The complexity of a body segment model is governed by the number of measurements taken [47].

Table B.1: A description of the 'standard man' sizes and parameters[65].

age	30 yr
height	1.72 m
mass	70 kg
weigh	690 N
surface area	1.85 m^2
body core temperature	37.0 $^{\circ}C$
body skin temperature	34.0 $^{\circ}C$
heat capacity	0.83 $kcal/kg - {}^{\circ}C$ (3.5 $kJ/kg - {}^{\circ}C$)
basal metabolic rate	70 $kcal/h$ (1.680 $kcal/day$, 38 $kcal/m^2 - h$, 44 W/m^2)
body fat	15%
subcutaneous fat layer	5 mm
body fluids volume	51 L
body fluids composition	53% intracellular 40% interstitial, lymph 7% plasma
heart rate	65 $beats/min$
blood volume	5.2 L
blood hematocrit	0.43
cardiac output (at rest)	5.0 L/min
cardiac output (in general)	3.0 + 8 * O2 consumption L/min
systolic blood pressure	120 $mmHg$
diastolic blood pressure	80 $mmHg$
breathing rate	15$/min$
O2 consumption	0.26 L/min
CO2 production	0.21 L/min
total lung capacity	6.0 L
vital capacity	4.8 L
tidal volume	0.5 L
lung dead space	0.15 L
lung mass transfer area	90 m^2
mechanical work efficiency	0-25%

B.1 Anthropometric measurements

Several studies for modeling humans assume numerical values for mass, height and volume of a 'standard human', a 70 kg man with parameters similar to those ones present in Table B.1.

In [10] authors proposed an alternative method for obtaining the relative body segment masses, CoM positions and radii of gyration for samples of college-aged Caucasian males and females by means of a Gamma-ray scanning technique.

Another possibility consists in using anthropometric data, in order to create flexible human models adaptable to different subjects. These quantities (Table B.2 and Figure B.1), provide the lengths of different anatomical segments of the 'average' body as a fraction of the body height h_{tot}.

Table B.3 gives the mass (or weigh) of different anatomical parts of the body as a fraction of total body mass m_{tot} (or equivalently, total body weigh) [65]. The mass and volume of body segments are determined on cadaver body segments, respectively by weighing them and by measuring the volume of water displaced for segments immersed in water (by using Archimedes' Principle). The average density of different body segments can then be determined, as in Table B.3. The volumes of body

Table B.2: Body segment lengths (data from [67]).

Segment	Segment length[1] Body height h_{tot}
head height	0.130
neck height	0.052
shoulder width	0.259
upper arm	0.186
lower arm	0.146
hand	0.108
shoulder width	0.259
chest width	0.174
hip width/leg separation	0.191
upper leg (thigh)	0.245
lower leg (calf)	0.246
ankle to bottom of foot	0.039
foot breadth	0.055
foot length	0.152

segments of living humans can be measured by water displacement and then their masses can be estimated quite well by using these cadaver densities. Whole body densities of living humans can be measured using underwater weighing.

An important aspect in human modelling is the range of motion of the biological joints, that could be very different from the idealized one. The average ranges of mobility in people are given in Table B.4 for the motions depicted in Figure B.2, along with the standard deviations about these values (for normal or Gaussian distributions with an average, μ, and standard deviation, σ, about 68% of all values are between $\mu - \sigma$ and $\mu + \sigma$).
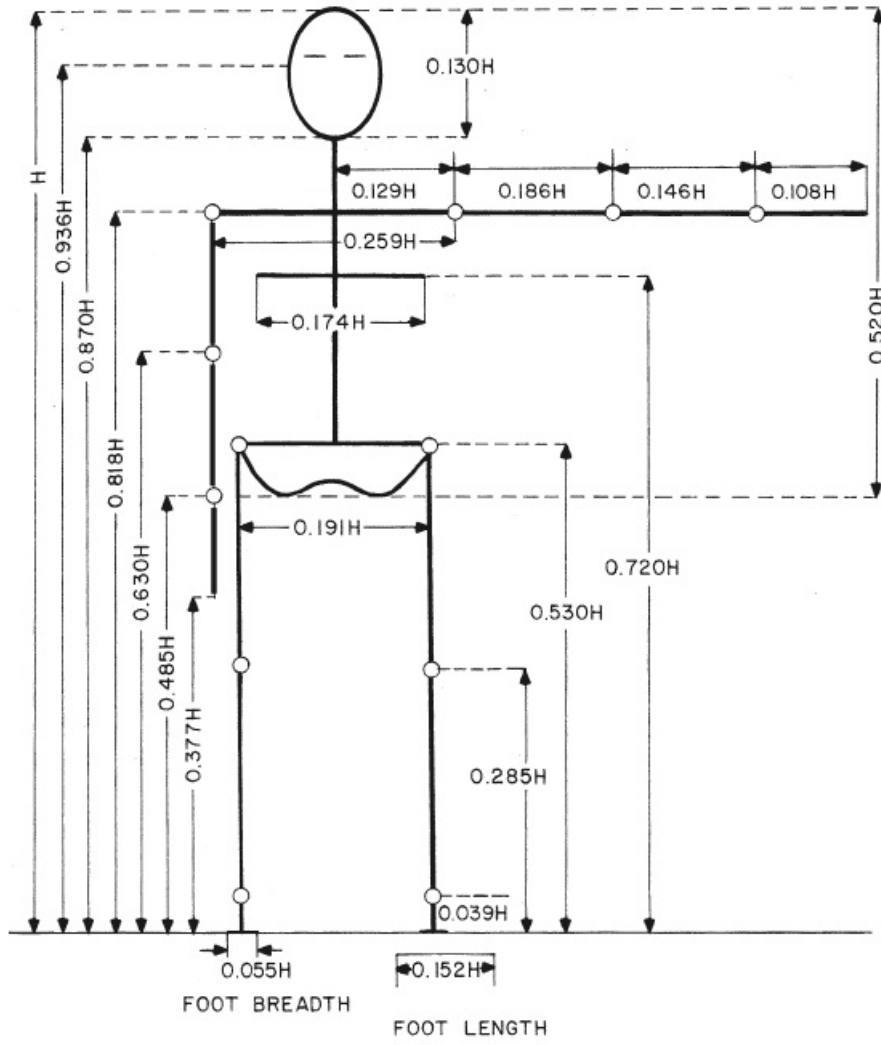
---

[1]Unless otherwise specified

Figure B.1: Body segments length, relative to the body height h_{tot}.

Table B.3: Mass and density of body segments (data from [67]).

Segment	Segment mass/ total body mass m_{tot}	Mass density (g/cm^3)
hand	0.006	1.16
forearm	0.016	1.13
upper arm	0.028	1.07
forearm and hand	0.022	1.14
total arm	0.050	1.11
foot	0.0145	1.10
lower leg (calf)	0.0465	1.09
upper leg (thigh)	0.100	1.05
foot and lower leg	0.061	1.09
total leg	0.161	1.06
head and neck	0.081	1.11
trunk	0.497	1.03

Table B.4: Range of joint mobility expressed in [deg] for opposing movements, with mean μ and standard deviation σ.

Opposing movements	μ	σ
shoulder flexion/extension	188/61	12/14
shoulder abduction/adduction	134/48	17/9
shoulder medial/lateral rotation	97/34	22/13
elbow flexion	142	10
forearm supination/pronation	113/77	22/24
wrist flexion/extension	90/99	12/13
wrist abduction/adduction	27/47	9/7
hip flexion	113	13
hip abduction/adduction	53/31	12/12
hip medial/lateral rotation (prone)	39/34	10/10
hip medial/lateral rotation (sitting)	31/30	9/9
knee flexion (prone) voluntary, arm assist	125,144	10,9
knee flexion voluntary (standing), forced (kneeling)	113,159	13,9
knee medial/lateral rotation (sitting)	35/43	12/12
ankle flexion/extension	35/38	7/12
foot inversion/eversion	24/23	9/7

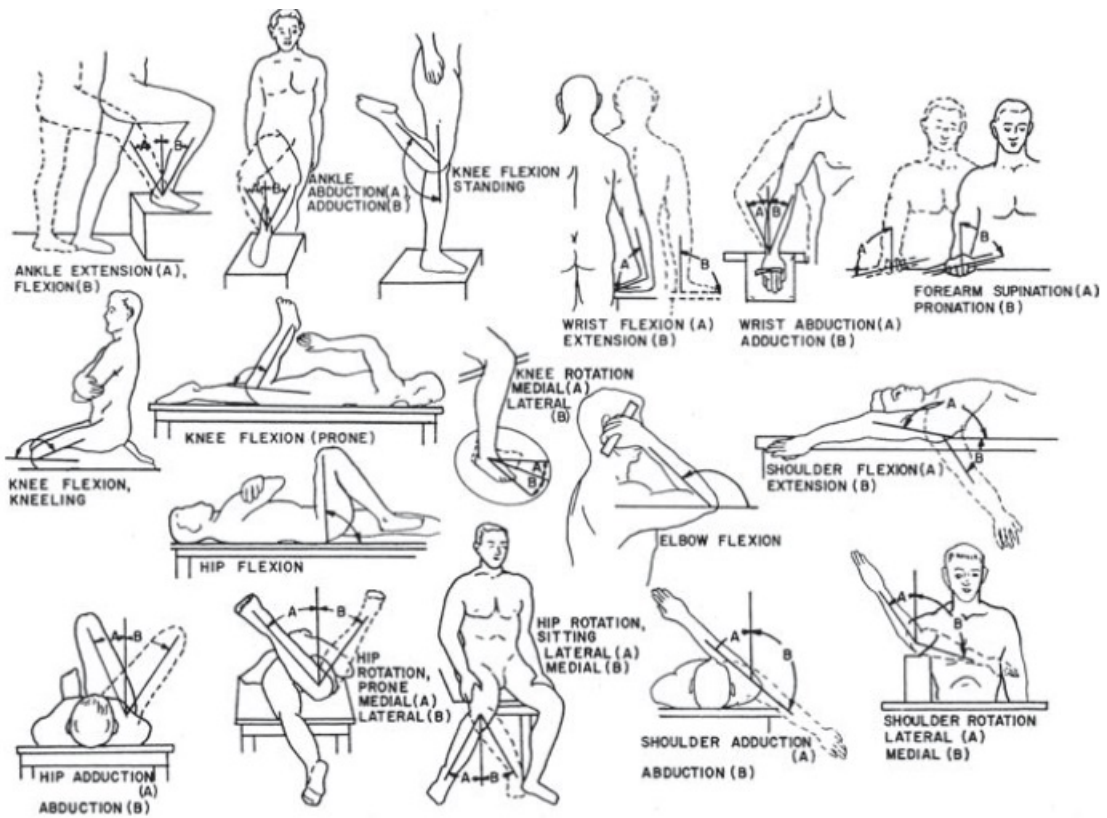The subjects were college-age males. Also see Figure B.2

Figure B.2: Postures used for Table B.4, for range of opposing motions.

Three DOFs are given for the shoulder and hip, two for the wrist and the foot (listed separately as foot and ankle), and one each for the elbow and forearm. The knee has 2 DOFs: the flexion in a 1D hinge and the rotation of the upper and lower leg about the knee [65].

Appendix C

Human Estimation Worst Case Variances

C.1   Introduction

In this report we will discuss how to obtain a worst-case estimate for the pre-processing step of the sensors used for human motion dynamics estimation in the Dynamic Interaction Control lab.

C.2   Review on variance propagation

In the following $X \sim \mathcal{N}(\mu_X, \Sigma_X^2)$ and $Y \sim \mathcal{N}(\mu_Y, \Sigma_Y^2)$ will indicate arbitrary multivariate continuous random variable whose distribution is Gaussian.

C.2.1   Sum of multivariate gaussians

Assuming that X and Y are independent, their sum is distributed as a gaussian with mean the sum of the means and variances the sum of variances.

$$Z = X + Y \tag{C.1}$$

$$Z \sim \mathcal{N}(\mu_X + \mu_Y, \Sigma_X^2 + \Sigma_Y^2) \tag{C.2}$$

C.2.2   Affine function of a gaussian

If A is a matrix and b is a vector of appropriate size, we have

$$Z = AX + b \tag{C.3}$$

$$Z \sim \mathcal{N}(A\mu_X + b, A\Sigma_X A^T) \tag{C.4}$$

This formulas are typically used also in the general (non-linear) case, for example in the Extended Kalman filter. If Z is a nonlinear function of X, an approximation of the distribution of Z as gaussian distribution is given by:

$$Z = f(X) \tag{C.5}$$

$$A = \left(\frac{\partial f}{\partial X} \Big|_{X=\mu_X} \right) \tag{C.6}$$

$$\tilde{Z} \sim \mathcal{N}(f(\mu_X), A\Sigma_X A^T) \tag{C.7}$$

Assuming that Σ_X is a diagonal matrix, then the maximum variance of $\tilde{Z}$ are maximised by $s_A^2 \max(\Sigma_X)$, where s_A is the maximum singular value of A. We will use this formula to propagate the worst-case variances.

C.3   Used sensors and data sheet variance

We list a series of sensors used in the human dynamics experiments. Notice that for some of this sensor the assumption that their error is distributed as a guassian variable is not verified in reality. The quantity that is published by the manufacturer of the sensors is tipically an "accuracy", whose definition is not standardized among manufactures. For this reason we try to just extract from the datasheets a "maximum error" (that we call $\epsilon_{\text{measure}}$) in the measure, that then we convert to variance of a single output channel with the following formula:

$$\sigma^2_{\text{measure}} = (\epsilon_{\text{measure}}/3)^2$$

The rationale behind this is a that 99.7 % of the samples extracted from a random variable distributed with a gaussian distribution are found in the interval $[\mu - 3\sigma, \mu + 3\sigma]$ (see the 68-95-99.7 or three sigma rule).

The single channel variances extracted in this way from the datasheet can then be converted to a covariance matrix assuming that the channels are mutually independent (that is again a quite strong assumption) obtaining a diagonal covariance matrix.

C.3.1   Force Plate

Data sheet : www.amti.biz/OR6-6.aspx

Most of the errors in a Force Plate come from the nonlinear effects and the hysteresis .

From the datasheet, assuming the reported full scale is:

$$\text{FS}_f = \begin{bmatrix} 2224N \\ 2224N \\ 4448N \end{bmatrix} \tag{C.8}$$

for forces

$$\text{FS}_\tau = \begin{bmatrix} 1129 Nm \\ 1129 Nm \\ 565 Nm \end{bmatrix} \tag{C.9}$$

for torques.

The biggest source of noise is sum of the hysteresis and non-linearity, that accounts for an error of 0.4% on the full scale. Another relevant error is the crosstalk in F_x and F_y due to the load on F_z. The typical weigh of a subject is $700N$, so we have to account this in the figure of epsilon for F_x and F_y.

Assuming then the ϵ_f and ϵ_τ are given by:

$$\text{FS}_f = \begin{bmatrix} 0.004 * FS + 0.02 * 700 = 23N \\ 0.004 * FS + 0.02 * 700 = 23N \\ 0.004 * FS = 18N \end{bmatrix} \tag{C.10}$$

and

$$\text{FS}_\tau = \begin{bmatrix} 0.004 * FS = 4.5 Nm \\ 0.004 * FS = 4.5 Nm \\ 0.004 * FS = 2.25 Nm \end{bmatrix} \tag{C.11}$$

the relative worst case variances are given by:

$$\text{diag}\left(\Sigma_f\right) = \begin{bmatrix} 59 N^2 \\ 59 N^2 \\ 36 N^2 \end{bmatrix} \tag{C.12}$$

and

$$\text{diag}\left(\Sigma_\tau\right) = \begin{bmatrix} 2.25 (Nm)^2 \\ 2.25 (Nm)^2 \\ 0.56 (Nm)^2 \end{bmatrix} \tag{C.13}$$

C.3.2 XSens MTx IMU

Data sheet : https://www.xsens.com/wp-content/uploads/2013/11/mtx-leaflet.pdf

$$\epsilon_{\text{acc}} = 0.002 \times 50 \frac{m}{s^2} = 0.1 \frac{m}{s^2}$$

$$\epsilon_\omega = 0.001 \times 21 \frac{[rad]}{s} = 0.021 \frac{[rad]}{s}$$

$$\sigma_{\text{acc}}^2 = 0.0011111 \frac{m^2}{s^4}$$

$$\sigma_\omega^2 = 5 \times 10^{-5} \frac{[rad]^2}{s^2}$$

$$\sigma_{\dot\omega}^2 = \text{SSSGVEL} * \sigma_\omega = 2 \times 10^{-4} \frac{[rad]^2}{s^4}$$

Notice that SSSGVEL is defined in the next section.

C.4 Variance propagation

C.4.1 Joint angles

For joint estimation, the location of three imaginary points in the body are computed by averaging the location of two markers. For each channel (x,y,z) averaging means summing the two variances and then dividing them by 4 (2^2). Each one of this point has then variance:

$$\sigma^2_{\mathrm{point}} = 5.555 \times 10^{-8} m^2 \tag{C.14}$$

Two components of this imaginary point are then subtracted (their variance are summed, $\sigma^2_{\mathrm{diff}} = 1.1111 \times 10^{-7} m^2$) and the angle between the the difference vector and the vertical is computed as the arctangent of the ratio of two components. In formulas :

$$Q = \arctan\left(\frac{X}{Y}\right) \tag{C.15}$$

with

$$\frac{\partial Q}{\partial \begin{bmatrix} X \\ Y \end{bmatrix}} = \begin{bmatrix} \frac{X}{X^2+Y^2} & -\frac{1}{X^2+Y^2} \end{bmatrix} \tag{C.16}$$

Assuming that a typical value for the difference vector is $X = Y \approx 0.5m$, so the Jacobian is similar to $\begin{bmatrix} 1 & -0.5 \end{bmatrix}$, so the variance in the joint encoders is more and less the sum of variances, $\sigma^2_{\mathrm{q}} \approx 2.22 \times 10^{-7} [rad]^2$.

C.4.2 Joint velocities and accelerations

Joint velocity and acceleration estimates are obtained as a weighed sum of a windows of elements, using the Savitzky Golay filters. Assuming that the errors in the samples of the angles are indipendent between time samples the variance of the joint velocity and acceleration estimate is simply given by the variance of joint angles multiplied by the sum of the square of the coefficient of the filters. In the human motion dataset we are using a Savitzky Golay filter of order 3 and windows size of 57. We have then that SSSGVEL $= 4\frac{1}{s^2}$ and SSSGACC $= 30\frac{1}{s^4}$. We have then:

$$\sigma^2_{\dot{q}} = \mathrm{SSSGVEL} \times \sigma^2_{\mathrm{q}} \approx 4 \times 2.22 \times 10^{-7} = 8.88 \times 10^{-7} \frac{[rad]^2}{s^2} \tag{C.17}$$

$$\sigma^2_{\ddot{q}} = \mathrm{SSSGACC} \times \sigma^2_{\mathrm{q}} \approx 30 \times 2.22 \times 10^{-7} = 6.66 \times 10^{-6} \frac{[rad]^2}{s^4} \tag{C.18}$$